

AD-A107 899 ROYAL AIRCRAFT ESTABLISHMENT FARNBOROUGH (ENGLAND) F/6 20/4
MEASUREMENTS IN THE NEAR-WAKE OF A TRANSPORT MODEL, TO DETERMIN--ETC(U)
FEB 81 A J PRIEST, D G DOBNEY, R P HILL
UNCLASSIFIED RAE-TR-81012 DRIC-BR-79571 NL

ROYAL AIRCRAFT ESTABLISHMENT FARNBOROUGH (ENGLAND) F/6 20/4
MEASUREMENTS IN THE NEAR-WAKE OF A TRANSPORT MODEL, TO DETERMINE--ETC(U)
FEB 81 A J PRIEST, D G DOBNEY, R P HILL
RAE-TR-81012 DRIC-BR-79571 NL

DRIC-BR-79571

NL

JOE J
40
NOTES

END
DATE
FILMED
82
DTIC

TR 81012

TR 81012

BR79571

LEVEL II

①



ROYAL AIRCRAFT ESTABLISHMENT

*

Technical Report 81012

February 1981

DTIC

NOV 30 1981

E

**MEASUREMENTS IN THE NEAR-WAKE
OF A TRANSPORT MODEL,
TO DETERMINE THE LIFT, DRAG AND
DRAG COMPONENTS USING
MASKELL'S ANALYSIS**

by

A. J. Priest

D. G. Dobney

R. P. Hill

*

Procurement Executive, Ministry of Defence
Farnborough, Hants

DTIC FILE COPY

81 11 12 024

ROYAL AIRCRAFT ESTABLISHMENT

Technical Report 81012

Received for printing 3 February 1981

MEASUREMENTS IN THE NEAR-WAKE OF A TRANSPORT MODEL, TO DETERMINE THE LIFT,
DRAG AND DRAG COMPONENTS USING MASKELL'S ANALYSIS

by

A. J. Priest

D. G. Dobney

R. P. Hill

SUMMARY

Extensive measurements have been made on a plane normal to the wake of a swept-wing/fuselage model of airbus type, at $C_L = 0.49$ in incompressible flow, using a computer-controlled wake-traverse system incorporating a null-reading five-hole yawmeter probe. The results define the detailed distributions of total pressure defect, flow velocity, flow angles and streamwise vorticity in the viscous wake at that plane.

The results have been analysed within the basic theoretical framework set out by Maskell (1973), allowing the calculation of lift and drag from traverse data, and the resolution of the drag into provisionally-defined components $C_{D I}$ and $C_{D II}$, respectively relating to the profile drag and vortex drag.

at sub sub

Departmental Reference: Aero 3497

Copyright

©

Controller HMSO London
1981

LIST OF CONTENTS

	<u>Page</u>
1 INTRODUCTION	3
2 DETAILS OF THE MODEL AND ITS SUPPORT RIG	4
3 GENERAL BACKGROUND TO THE WAKE-TRAVERSE ANALYSIS	5
3.1 Theoretical principles	5
3.2 Practical application of the drag analysis procedure	6
3.3 Practical application of the lift analysis procedure	7
3.4 Measurement of the strut circulation effect	8
4 EXPERIMENTAL DETAILS	9
4.1 General comments	9
4.2 Experimental programme	9
4.3 Reduction of forces data	9
4.4 Wake-traversing - experimental technique	10
4.5 Wake-traversing - experiment control, data logging, data reduction	13
4.6 Wake-traversing - analysis of processed data	14
5 EXPERIMENTAL RESULTS - GENERAL COMMENTS	15
5.1 Forces and moments data	15
5.2 General characteristics of the flowfield	15
6 EXPERIMENTAL RESULTS - WAKE-TRAVERSE DRAG	19
6.1 General comments	19
6.2 Comparison with mechanical balance data	20
6.3 Extraction of support rig effects	22
6.4 Tunnel corrections	23
6.5 Induced drag	24
6.6 Evaluation of results	24
7 EXPERIMENTAL RESULTS - WAKE-TRAVERSE LIFT	26
7.1 General comments	26
7.2 Evaluation of results	27
8 CONCLUDING REMARKS	27
8.1 Experimental results	27
8.2 Experimental technique	29
Table 1 Summary of wake-traverse tests in the No.2 11½ ft tunnel (Three-strut support rig)	31
Table 2 Lift and drag of model and its support rig (uncorrected) - summary of cases analysed in depth	32
Table 3 Lift and drag of the model, net of support and constraint corrections - summary of cases analysed in depth	33
Table 4 Drag increments measured in the traverse plane	34
Table 5 Analysis of drag contribution of support rig	36
Table 6 Geometric details of the model	37
List of symbols	38
References	41
Illustrations	
Report documentation page	

Accession For	
NTIS GRA&I	<input checked="" type="checkbox"/>
DTIC TAB	<input type="checkbox"/>
Unannounced	<input type="checkbox"/>
Justification	
By	
Date	
Avail Codes	
For	
Dist	
A	

Figures 1-37
inside back cover

1 INTRODUCTION

The work described in this Report forms part of a long-term study of the wakes of lifting wings and wing-body combinations in incompressible flow. It is based on measurements made with a computer-controlled five-axis wake-traverse system, employing a five-hole yawmeter probe in a self-aligning or null-reading mode^{1,3-6}. The measuring accuracy of such a probe used in the conventional, fixed orientation mode⁷ was considered insufficient in the present context.

The primary objective of the current work is the trial application of the Maskell drag analysis scheme to a comprehensive set of total pressure defect, flow angle and flow velocity measurements on a plane cutting the wake of a model representing a swept-wing airbus-type transport. Maskell¹ reports encouraging results from preliminary measurements in the wake of a constant chord, uncambered wing ($A = 6$) on a simple wire support rig. The additional complexities of camber, sweep and taper, fuselage representation, and the use of a three-strut model support rig are now introduced.

Maskell's analysis¹ is a development of that due to Betz², and allows the calculation of the lift and drag of a wind-tunnel model from measurements confined to the viscous wake portion of a wake-traverse plane, normal to the tunnel axis, downstream of the model. The total traverse-derived drag coefficient (C_{D_t}) may, subject to the validity of certain assumptions detailed in Ref 1, be resolved into two components. The first (C_{D_I}) is broadly consistent with the conventional concept of 'profile drag', the second ($C_{D_{II}}$) with that of 'vortex drag'. Maskell¹ stresses that the current definitions of C_{D_I} and $C_{D_{II}}$ are provisional ones only. Their physical validity and their uniqueness - i.e. their invariance with the chosen location of the traverse plane - remain to be fully substantiated by experiments on a wide range of model and support rig configurations.

Ref 1 argues the potential utility of this drag analysis procedure, once its soundness and its generality of application have been experimentally established. Once one has a means of accurately separating the profile drag and vortex drag constituents of lift-dependent drag, one can then more confidently extrapolate model-scale test results to flight-scale, particularly for high-lift configurations. It will then be possible to re-examine the validity of the planar wake assumptions implicit in the classical vortex drag prediction theories, and to study three-dimensional profile drag effects. Again high-lift configurations will be of primary interest.

A secondary objective of the present work is the assessment of the usefulness of wake-traverse measurements for diagnostic purposes; the assumption being that measurements would only be made in a limited portion of the viscous wake, and made in less detail than that required for drag analysis. It is reasonable to expect that such measurements could assist in the identification of localised sources of drag that might be considered excessive, such as, for example: wing-fuselage junctions; nacelles and external stores; flap and slat deployment mechanisms; wing fences, etc. A major interest in the present work is the unfilleted wing-fuselage junction of the model, and to what extent the junction vortices (if present) contribute to the profile drag and vortex drag terms.

Another secondary objective of the present work is the assessment of the extent of mutual interference between the model and its three-strut support rig. The wake-traverse procedure clearly cannot yield such precise quantitative data as the conventional mechanical balance tare and interference procedures. It can, however, be expected to produce a great deal of useful qualitative information as to the mechanisms determining the viscous component of the mutual interaction between the model and its support rig.

The lift condition ($C_{Lc} = 0.49$) in the present investigation is comparable to that considered in Maskell's pilot study of the wake at several stations downstream of a pitching^{1,15}, though the current Reynolds number is some 4.5 times higher ($Re_c = 950000$). The current wake-traverse system⁶ is in some respects more advanced than Maskell's, particularly with regard to its extensive computerised experiment-control and data-handling facilities. Its greater versatility of application has been obtained at the cost of potential increases in measurement rate, though future software development may recover the situation somewhat.

This Report also discusses some aspects of the results of some preliminary studies with the present wake-traverse system, made by way of post-commissioning trials. Measurements were made at three lift conditions (one corresponding to that currently considered) at fixed distance aft of the swept-wing currently considered. The only configuration difference was the absence of a fuselage, the flaps and slats being retracted in all four cases.

Table 1 lists the configurations studied subsequent to Maskell's small-scale pilot study; all but one involved cambered swept-wings. Tables 2 and 3 give the key lift and drag results for the three wing-body cases analysed in detail, while Tables 4 and 5 give a detailed drag breakdown for the present wing-body case.

Figs 1, 2 and 6a show the present experimental configuration, while Figs 3 to 5 show the basic corrected balance-derived force and moment characteristics of the model.

It is appropriate to note that, since the wake-traverse drag analysis technique is still very much in the development stage and low-speed tunnel manpower very limited, the resources have not been available to effect a number of fairly straightforward computer software and computerised data analysis developments. The current working processes are therefore relatively inefficient, and are certainly unrepresentative of a fully-developed wake-traverse system being applied to a long-term drag analysis program. At this early stage it has been felt necessary to analyse the flowfield data in very considerable detail, rather than merely submit it to a series of essentially unmonitored computerised integration processes with the sole objective of deriving the values of the C_{DI} and C_{DII} contributions to C_{Dt} . This too has extended the timescale of each wake-traverse, beyond that representative of routine application.

2 DETAILS OF THE MODEL AND ITS SUPPORT RIG

The model comprises a straight-tapered 28° (quarter chord) swept-wing of aspect ratio 8.35. The wing has no dihedral or twist and is mounted at mid/low position on a fuselage, as shown in Fig 1. The maximum wing thickness is 10.7% (at 37.5% chord), and

the maximum camber is 1.1% (at 75% chord). The aerofoil section is a development of an NPL type, having considerable rear loading. Table 6 gives the basic planform dimensions and Ref 8 gives the detailed section profile co-ordinates.

The fuselage is representative of a wide-bodied transport type, and the wing reference plane is at 1.1° incidence relative to the fuselage axis. The wing-fuselage junctions are unfilleted, and the diameter of the circular section fuselage remains constant through the wing root region.

The model has been tested in cruise configuration, with the slats and flaps retracted, and with boundary layer transition fixed on the forward fuselage and on the upper and lower wing surfaces. No flap hinge or flap jack fairings have been represented on the wing, and all joints and excrescences were carefully smoothed flush with the surfaces.

The model was mounted on a conventional three-strut support rig (Fig 2). The strut cleat assemblies on the undersurfaces of the wings and of the rear fuselage were not recessed into these surfaces.

3 GENERAL BACKGROUND TO THE WAKE-TRAVERSE ANALYSIS

3.1 Theoretical principles

The wake-traverse drag analysis scheme is based on the equation for the conservation of streamwise (x) momentum. This is applied to a control volume enclosing the model, and otherwise bounded by the wake-traverse plane, the displacement surfaces of the tunnel wall boundary layers, and a plane upstream of the model where undisturbed, basically one-dimensional flow conditions (H_0 , p_0) are assumed to exist. A further assumption is that no streamwise pressure gradient exists in the empty tunnel working section. The derivation of the model lift, using the same control volume and the equation for the conservation of vertical (z) momentum follows essentially similar lines. The drag and lift equations thus derived are set out in Fig 6b&c respectively.

The lift and drag forces deduced from the wake-traverse measurements relate to the constrained flow conditions within the tunnel working section. That is, these forces are in principle identical to those sensed by the tunnel mechanical balance (where one is considering the model and the wetted surfaces of the 'live' support rig as an entity); they would therefore be subjected to the same tunnel corrections.

The basic concept of a scale-dependent viscous shear layer effect ('profile drag') and an independent inviscid secondary flow effect ('vortex drag') is a useful theoretical tool, but difficulties arise in defining these effects in such a way that they can be isolated in terms of experimentally measurable quantities. The main difficulty is that one cannot discriminate between that portion of the total head decrement measured on the traverse plane that is attributable to 'profile drag' (C_{D_I}) effects, and that portion attributable to the viscous dissipation of streamwise shed vorticity between the wing and the traverse plane, i.e. 'vortex drag' ($C_{D_{II}}$) effects. For example, streamwise vorticity is shed within the wake flow inboard of the tip vortex. In this region it is reasonable to assume that the viscous dissipation of streamwise vorticity will be negligible, the velocity gradients typically being relatively low. This is not the case for

the tip vortices, however, where extremely high radial velocity gradients exist and surface shear layer fluid from the wingtip regions is entrained into the vortices. For the purposes of the analysis of the results of the present investigation it has been assumed that the total head defects in the vortex cores (measured as a 'profile drag' contribution $\Delta C_{D_{I_{vc}}}$) are dominantly produced by the dissipation of $C_{D_{II}}$ related rotational energy generated in an idealised inviscid secondary flow. Thus the increment $\Delta C_{D_{I_{vc}}}$ has been accounted to the $C_{D_{II}}$ term.

If the rate of viscous dissipation in the vortex core is significant, and the above $\Delta C_{D_{I_{vc}}}$ transfer is not made, then one would expect an interchange between the measured C_{D_I} and $C_{D_{II}}$ components of a constant C_{D_t} - as the traverse plane is moved progressively further aft of a wing at given lift. The C_{D_I} term would increase with progressive dissipation of vorticity. Maskell¹⁵ found just such an effect in the analysis of the first two of the three traverses behind a pitchwing (Ref 1 reports the first traverse and the basic theory), but was unable to account for it fully with the above $\Delta C_{D_{I_{vc}}}$ adjustment.

Throughout the remainder of this Report the terms 'profile drag' and 'vortex drag' are frequently used with reference to the measured C_{D_I} and $C_{D_{II}}$ components. The single wake-traverse dataset considered cannot be taken either to confirm or to disprove the reservations expressed in section 1, as to the validity of the C_{D_I} and $C_{D_{II}}$ definitions.

3.2 Practical application of the drag analysis procedure

Fig 6a shows the regions of the wake-traverse plane within which measurements have been made. The arbitrarily defined analysis regions 1-10 indicate the limits of measurements on rectangular meshes of points. Each analysis region extends a little way beyond the extremities of the viscous wake, and has only a limited variation of mesh size within it.

Fig 6b summarises the key expressions occurring in the drag analysis¹ and shows the quantities (subscript '2') that must be measured at each mesh point on the traverse plane. The tunnel reference parameters U_0 , H_0 , q_0 are defined at the centre of the upstream reference plane, and the theory assumes these to represent the whole upstream plane. This assumption is not entirely valid (Fig 14) but appropriate corrections can readily be made to the C_{D_I} or 'profile drag' term (section 4.6).

The auxiliary terms $\Delta C_{D_{IIa}}$ and $\Delta C_{D_{IIb}}$ (Fig 6b; equations (6),(7)) represent induced upwash contributions. One can only measure the quantity $\int_w \psi' \xi ds$ on the traverse plane, not the quantity $\int_w \psi \xi ds$ employed in the basic¹ flow model. ψ is the stream function of the transverse flow that would exist far downstream in wind-tunnel if the distribution of streamwise vorticity ($\xi(y,z)$) measured in the wake-traverse plane were to persist unchanged to infinity downstream. ψ' is the actual stream function measured in the traverse plane for the approximately two-dimensional flow in the near field of the wing; $\Delta C_{D_{IIa}}$ and $\Delta C_{D_{IIb}}$ relate ψ' to ψ . $\Delta C_{D_{IIa}}$ defines a direct effect dependent on the spanwise loading on the wing, and $\Delta C_{D_{IIb}}$ defines a wall constraint or image effect. In evaluating these auxiliary terms x has been measured relative to the mean quarter chord station on the wing.

The first auxiliary term requires a circulation distribution $\Gamma(y)$ in its evaluation; this is equivalent to the surface integral of streamwise vorticity in the viscous wake on the traverse plane, outboard of each of a series of stations at various y values. $\Gamma(y)$ only emerges from the lift calculations discussed below, and so the evaluation of the auxiliary term cannot be incorporated readily into the computer data reduction scheme. Both terms have been calculated manually and appear in Table 4.

A correction term ΔC_{D_I} is applied to the C_{D_I} term (Fig 6b, equation (8)), correcting the C_{D_I} overstatement otherwise produced by the blockage velocity effect ($\Delta U_0 = U_e - U_0 = u_0$) of the presence of the model.

3.3 Practical application of the lift analysis procedure

Fig 6c shows the key expressions involved in the lift analysis, together with a schematic representation of the starboard half of the symmetrical 'liftloop' employed in the calculations. This contour lies entirely in the free-stream, other than for unavoidable crossings of support rig wakes (segment 'L-K' for example); for convenience it largely follows the edges of the arbitrarily chosen analysis regions.

The dominant contribution to the local lift coefficient C_{L_y} (Fig 7) at a spanwise station 'y' is $\rho U_e \Gamma_y / (q_0 b \bar{c})$ (Fig 6c, equation (2)), where Γ_y is the circulation round the contour formed by the line cutting the wake at 'y' (segment 'A-P' for example) and that portion of the liftloop lying to its right-hand-side. Γ_y is calculated thus, progressing from the starboard tip to the port, sequentially treating each 'y' station for which measured data are available. The liftloop or contour integration approach is, for the present purposes, more convenient than evaluating the surface integrals (for the streamwise vorticity) for the areas enclosed within the set of contours corresponding to the various 'y' values.

It has been found that the use of U_0 rather than U_e makes a negligible difference to the C_{L_y} values derived from this procedure, so U_0 has been used with a considerable resulting simplification of the data reduction scheme.

The contribution from the second term, the integral $\rho \int_w (U_2^* - U_2) W_2 dz$ along the cut through the wake, has consistently been found to be negligibly small.

The third term in the equation, namely $\rho U_e \Delta \Gamma_{LK} / (q_0 b \bar{c})$ corrects for the circulation jump encountered in crossing the main strut wakes (segment 'L-K' for example), when calculating C_{L_y} in the region $-y' \leq y \leq +y'$ between the struts. These struts are in fact lifting surfaces, given the sidewash field generated by the wing. This factor did not require consideration in Maskell's application of the theory to a wing on a wire support rig¹. The circulation Γ_y is evaluated taking the anticlockwise direction as positive, and the circulation increments produced by the streamwise vorticity shed from the wing on the segment 'PONMLKJH' (Fig 6c) of the contour in the strut region are in fact positive, taking the starboard strut as example. The circulation jump produced by the strut wake will be negative in terms of the above convention, so the correction $\Delta \Gamma_{LK}$ requires to be positive. The same argument holds for the port strut wake, all signs being reversed.

The strut circulation correction $\Delta\Gamma_{LK}$ ($= +\gamma_z$, Fig 8b) has been evaluated on a rectangular contour close to the starboard main strut at station 'A' ($z = -334$ mm), about half way along the wetted strut length. The streamlines crossing the rear segment of the contour at 'A' reach the main wake traverse plane at a height $z = -341.5$ mm, at which point the wake crossing segment L-K (Fig 6c) of the liftloop has been located, after having made the necessary supplementary measurements. (The streamlines were traced aft of 'A' to the traverse plane, by searching for the local high total head defect region generated by an excrescence temporarily attached to the strut trailing edge in plane 'A'.)

It has been assumed that the port strut wake has an identical γ_z to the starboard wake, at the same z , a reasonable assumption given the approximate constancy of the absolute circulation ($C_{LS\bar{c}}$) noted on the starboard strut in the region of 'A'. Accordingly the lift correction increment $C_{LS\bar{c}} = \rho U_0 \Delta\Gamma_{LK} / (q_0 b \bar{c})$ has been added to all C_{LY} values computed for $-y' \leq y \leq +y'$, as shown in Fig 7. A smooth curve has been faired through the strut regions on the C_{LY} plot, and the overall traverse-derived C_L obtained by spanwise integration.

It should be noted that C_{LY} represents the spanwise distribution of the defect of vertical momentum component in the traverse plane. As a consequence of the sidewash effects generated by the wing in its wake, and also of flow convergence over the rear fuselage, C_{LY} cannot be regarded as representing the spanwise lift distribution actually existing on the wing (even though it has been taken as such for the estimation of some small $C_{D_{II}}$ auxiliary terms). These crossflow effects will be particularly strong in the centre section, so the C_{LY} diagram (Fig 7) gives no directly useful information on the wing-body interaction effect on spanwise loading.

3.4 Measurement of the strut circulation effect

Measurements have been made close to the starboard main strut, on contours enclosing the strut section, for each of a number of constant z planes, using the wake-traverse gear. Although it was not possible to make flow measurements immediately upstream of the strut nose, it was found that one could make extrapolations with sufficient confidence to close the circulation loop and thus compute γ_z . Fig 8b shows the variation of crossflow induced circulation along the strut thus derived. When γ_z is expressed in C_{LSZ} form (i.e. nondimensionalised with respect to local strut chord $C(Z)$) the sectional circulation is constant over a considerable portion of the exposed strut length. The rapid drops in sectional γ_z near the lower and upper ends of the strut can respectively be attributed to strut guard leakage plume effects and to model wake effects.

In addition to establishing γ_z for the wing plus body case, the exercise included the measurement of γ_z at station 'A' for three model lift conditions for the wing-alone configuration¹³. This data (Fig 8a) shows that the strut circulation γ_z , one of the interference effects of the model on the support rig, is strongly dependent on the lift developed by the model. At $C_{LC} \approx 0.49$ the strut circulation for the station 'A' is some 50% greater for the wing and fuselage case than for the wing alone case, a disparity which is far greater than proportionate to the probable changes in C_L distribution on the wing, in proximity to the strut, produced by introduction of a fuselage.

EXPERIMENTAL DETAILS

4.1 General comments

The tests were made in the No.2 11½ ft × 8½ ft (3.5 m × 2.6 m) low-speed tunnel at Farnborough, at a windspeed of 60 m/s corresponding to a mean chord Reynolds number $Re_c = 0.95 \times 10^6$. The model was tested without a tailplane, fin or engine nacelles.

Boundary layer transition was fixed at the 5% chord line over the full span of the upper wing surface, similarly at the 35% chordline on the lower surface, and at the 50% maximum fuselage diameter station on the model nose - using wires in each case. Some preliminary flow visualisation tests were made - employing an acenaphthelene/petroleum - ether surface deposit - to confirm the effectiveness of the transition fixing, particularly at the chosen wake-traverse incidence ($\alpha_T = 5.10$). It was considered essential to preclude the possibility of transition 'creep' over the considerable duration of traverse measurements.

4.2 Experimental programme

This required some 125 tunnel running hours over a one month period. It comprised

- (i) an initial set of mechanical balance measurements, to establish the basic characteristics of the model and the effect of transition fixing (Figs 3 to 5),
- (ii) a detailed traverse of the viscous wake in a plane 7.4 tip chordlengths aft of the tip trailing-edges (Figs 1 and 6a), measurements being made at 5100 points, and,
- (iii) several partial traverses close to the fuselage side, seeking evidence of discrete vortices or excessive total head losses - generated in the wing/fuselage junction region.

The force measurements were made over a range of uncorrected incidence $-5^\circ < \alpha_T < 12^\circ$, the lower limit being fixed by separation on the wing under-surface (causing model buffeting), and the upper limit by stalling. The wake traverse measurements were carried out at a mean corrected lift coefficient $C_{Lc} = 0.49$, corresponding to a corrected incidence $\alpha_c = 5.25^\circ$ ($\alpha_T = 5.1^\circ$). During traversing the test condition was monitored by periodic mechanical balance measurements. No consistent trends of change in lift or drag were discernible, within the $\pm 0.8\%$ scatter band of lift data or the $\pm 1.2\%$ band of drag data (relative to mean values). Concurrent checks on the nominal dynamic pressure produced values lying well within $\pm 0.2\%$ of that desired ($q_0 = 2190.7 \text{ N/m}^2$).

4.3 Reduction of forces data

The balance measurements have been reduced to conventional coefficient form, using a standard computer program⁹. For the purposes of Figs 3 to 5 these coefficients have been corrected - for stream pitch, wall constraint, streamwise pressure gradient, solid-blockage and strut deflection (model CG offset) effects. No corrections have been applied in respect of separated flow wake-blockage effects (assumed negligible), or of the mutual interference between the model and its support struts¹⁰.

4.4 Wake-traversing - experimental technique

The measurements were made using a five-tube yawmeter with a central total pressure tube. It was of conventional design¹¹, constructed of 0.5 mm diameter (0.27 mm bore) hypodermic tubing, and having a nose apex angle of 60° . It was employed in a null-reading mode, being aligned with the local velocity vector before taking each set of reading - namely five pressures $[H, p_1, p_2, p_3, p_4]$ and the probe orientation angles $[\theta, \phi]$ relative to the tunnel centreline - at a given probe tip location $[x, y, z]$ relative to the intersection of the line joining the trailing-edge tips and the plane of model symmetry ($y = 0$). Probe alignment was effected by rotation of the probe support quadrant about a roll axis ($-200^\circ < \phi < +200^\circ$) parallel to the tunnel centreline, and by circumferential movements of the circular arc quadrant in a range $-30^\circ \leq \theta \leq +30^\circ$ (or alternatively $0^\circ \leq \theta \leq 60^\circ$) - where $\theta = 0^\circ$ corresponds to the aerodynamic axis of the probe being parallel to the tunnel axis. The θ, ϕ (quadrant and roll) motions have a virtual centre at the probe tip.

Lovell⁶ gives a detailed description of the mechanical operation of the traverse gear and the system providing probe nulling; he also gives details of the alternative manual, computer-assisted manual, and fully-computer-controlled modes of operation of the wake-traverse system. The system allows flow measurements to be made at sequences of points forming prescribed lines or grids of points in any chosen portion of the tunnel working section, entirely under computer control where appropriate.

The probe nulling motions of the present wake-traverse system differ from those described by Maskell¹; the latter corresponded to direct movements in the pitch and yaw senses, rather than in quadrant and roll senses. The current system inherently has a somewhat slower rate of probe nulling - and therefore a slower rate of measurement - for a given standard of control system. It does however have the advantage of reduced aerodynamic interference on the flow under study - due to the elimination of significant probe support asymmetries.

The complexities of the mechanism and the control system required to effect nulling of the probe can be eliminated if it is used in fixed orientation. One then has to establish calibrations for the flow angles between the probe axis and the local velocity vector, and the total head coefficient and static pressure coefficient, as functions of the five measured pressures; Ref 7 describes such an approach. However, such calibration schemes have been claimed¹¹ to give typical accuracies of dynamic pressure measurement of only 3-5%, for flow angles less than 25° . Such an accuracy would be unacceptably low in the present drag analysis context.

Fig 1 shows the location of the main wake-traverse plane relative to the model, and also those of the supplementary planes 'A' and 'B' relative to the fuselage sides. Fig 6a shows the division of the traverse plane into rectangular analysis regions, each extending a short distance beyond the wake extremities. Each analysis region is composed of regular rectangular grids of measurement points, chosen according as to the local gradients of flow angle and total head encountered, as follows.

<u>Region No.</u>	<u>Region</u>	<u>Δy (mm)</u>	<u>Δz (mm)</u>
1, 5	vortex cores	4	4
	vortex periphery	8	8
2, 4	inner wing	40	8
	strut top/mid wing	8	8
	outer wing	40	8
3	centresection	20	8
6, 7, 8	struts	8	40

Experience has shown that it is often important to avoid changes of grid pitch within a reference area; small economies in tunnel running time can be offset by the introduction of difficulties in interpreting the local vorticity data at the intersections of meshes of differing pitch. Constant values of grid $\Delta y, \Delta z$ are particularly useful in the centresection reference area - where the wingroot vortices may have migrated further towards the centreline than expected - and also in the tip vortex reference area, where one wishes to examine the manner in which the viscous wake is rolled round the vortex core. In the present tests the relaxation of the mesh size on the vortex periphery - on ground of economy of measurement points in the light of the relatively lower gradients of H, θ, ϕ observed - has proved to be a mistake. It led to a loss of detail in the measured vorticity distribution between the vortex core and the viscous wake rolled round it. The consequent loss in the accuracy of C_{DII} measurement is negligible, but one has lost some useful data on the wake roll-up process.

During the wake-traverse test, the tunnel mechanical balance readings (C_L, C_D) and the tunnel speed were routinely checked, the model incidence ($\alpha_T = 5.1^\circ$) being held constant throughout. Additionally, measurements were made at a check point before and after each measurement run - to highlight any changes in test condition or probe calibration characteristics, or system failure during the run. The check point disparities fell entirely in the third category, and the relevant data has been discarded where necessary.

The check point was located in the free-stream outboard of the starboard tip vortex (where the local yaw angle was small), and it was also used to set the zero for quadrant angle (θ) measurements - by 'balancing' or nulling the probe with the local velocity vector at two roll angles approximately 180° apart. The deviation ($\Delta\phi_B - 180^\circ$) is a function of the inevitable small probe asymmetries and also of the local quadrant angle (θ_B), where

$$\theta_B = \frac{1}{2}(\theta_{BS} - \theta_{BUS}) \quad (1)$$

Because of the existence of the roll asymmetry the 'unstable' balance point (θ_{BUS}, ϕ_{BUS}) can only be located by reversal of the usual convention that positive roll error signals (Δp_R) require negative increments of roll angle ϕ to null them. The roll asymmetry is, for the purposes of probe calibration, characterised by the roll tube angular position error

$$\epsilon_p = \tan^{-1} \left[\sin \theta_B \tan \left(\frac{\Delta \phi_B - 180}{2} \right) \right] \quad (2)$$

where θ_B is the measured quadrant angle (noting that one sets a zero with $\theta_B = \theta_{BS} = -\theta_{BUS}$) and $\Delta \phi_B$ the roll angle increment between the normal (or 'stable') and the 'unstable' balance points. Following the recommendation of Ref 6, ϵ_p has in fact been computed as the mean of values derived for a number of θ_B values corresponding to a range of points in the flowfield.

The roll angle zero is set absolutely, using an inclinometer, for $\phi = +90^\circ$ with the quadrant arm horizontal.

Lovell⁶ gives a detailed description of the calibration scheme used for the probe, including the relationships used for transforming the θ, ϕ measurements to corrected flow angles in pitch (w^0) and yaw (v^0) - and also gives an assessment of the angular resolution of the probe and the precision of measurements. In essence the probe calibration requires the following quantities as functions of the local dynamic pressure q_m measured by the probe:

- (i) q_1/q_m , where q_1 is the true dynamic pressure (Fig 9).
- (ii) The error $(H_m - H_1)/q_1$ where H_m is the total head measured by the probe's central tube and H_1 the true value (Fig 10).

The calibrations are based on the empty tunnel conditions (ie $q_1 = q_0$, $H_1 = H_0$, in this case), the 'true' values being established by measurements with a pitot-static tube. The q_m data shown has been normalised using q_{m60} , the q_m value at the 60 m/s test speed. The quantities q_m and H_m have been measured with the probe nulled. q_m is defined by

$$q_m = H_m - \frac{1}{4}(p_1 + p_2 + p_3 + p_4)$$

where $p_1 \dots p_4$ are the readings of the probes' four side tubes. Since pressure transducers of adequate quality were available for only four of the five tubes, the calibration in the present investigation has been based on

$$q_m = H_m - \frac{1}{4}(p_1 + p_2 + 2p_3) \quad (3)$$

where each of the four pressures is measured relative to the tunnel plenum wall static pressure p_m . The probe error signals, Δp_Q and Δp_R , are employed in the probe nulling procedure; the angles θ and ϕ are adjusted such that at a 'balance' condition

$$\Delta p_Q = p_1 - p_2 = 0 \quad (4)$$

$$\Delta p_R = p_3 - p_4 = 0 \quad (5)$$

A phase-advance system is employed to increase the effective frequency response of the system, by compensating for the viscous damping in the long lines between the probe and the transducers, which are located in thermally insulated packages outside the tunnel.

The pressures Δp_Q and Δp_R are measured independently of H_m, p_1, p_2, p_3 , using transducers functioning as part of the probe nulling control system. (In the former case transducers with minimal zero drift are required, the voltage sensitivity $\delta E/\delta p$ being less important; in the latter case $\delta E/\delta p$ constancy is of vital importance and zero drift effects can be accommodated by keeping measurement runs fairly short.)

The calibration scheme also requires:

- (i) ϵ_p as defined in equation (2) above
- (ii) the pitch of the traverse gear roll axis (α_{RA}^0)
- (iii) the yaw of the traverse gear yaw axis (ψ_{RA}^0).

Both the latter are referred to the horizontal centreline of the tunnel working section. They are obtained by comparison of five-hole probe measurements with Conrad tube measurements at points in the model flowfield where substantially pure pitch and pure yaw conditions exist.

In the central portion of each vortex core the normal quadrant angle range ($-30^\circ \leq \theta \leq +30^\circ$) (probe located at the quadrant arm centre) has been found insufficient to achieve probe nulling owing to extreme values of the flow angles ($V_{\max}^0 \approx W_{\max}^0 \approx 30.5^\circ$). Therefore the probe was remounted at one extremity of the 60° circular arc quadrant arm, and the range of quadrant angle $0^\circ \leq \theta \leq 60^\circ$ then readily accommodated the outstanding measurements. Some earlier measurements (including some at the check datum point) were repeated, to allow the re-evaluation of ϵ_p by a process of comparison.

4.5 Wake traversing - experiment control, data logging, data reduction

Ref 6 may be consulted for details of the very extensive computer software available for various modes of control of wake traverse experiments, for logging of data, and for the off-line reduction of the stored data (in disk file form) on completion of measurement runs.

It is however appropriate to note the following points here:

(i) Having achieved a null condition the analogue voltages representing the measured pressures, the current orientation (θ, ϕ) of the probe and its tip position (x, y, z) are logged by the computer via its ADC unit. The unprocessed data is written to a disk file and concurrently output as a single line of line-printer data. At the end of each prescribed sequence of measurements the corresponding series of $\theta, \phi, p_m - H$ datapoints can (if required) be displayed as a function of the spatial co-ordinate being varied (y or z in our case) on an analogue graph-plotter.

(ii) Control modes exist whereby the traverse gear will make measurements at a series of points defining lines and grids on the traverse plane - either under full computer control or under interactive control where the operator guides the nulling process.

(iii) The quality of the raw data has been assessed by monitoring the variation of the voltages corresponding to $\theta, \phi, p_m - H$ during each run, and by checking the consistency of measurements at the check datum point before and after each run.

(iv) The θ, ϕ nulling operation is controlled by an open-loop control system. The current θ and ϕ values at any instant are recorded as the cumulative sums of the starting values and all control signals ($\Delta\theta, \Delta\phi$) subsequently sent to the quadrant and roll drive motors. These cumulative sums, of signal pulses performing the dual function of control and power supply, also control the analogue ramp voltage generator which is monitored by the computer. Thus if a fault occurs in the θ or ϕ counter or ramp generator systems, or if the drive motors fail to respond to the signal pulses: the probe nulls correctly; the probe pressures are measured correctly; and the θ and/or ϕ values logged at the null condition are in error. A recurrent source of faults is the system of transmission of the θ and ϕ nulling drive/control signals through a low voltage brush system. The open-loop nature of the control system is a major weakness of the current wake-traverse system; the addition of a system to measure θ and ϕ directly would obviate the need to repeat many measurements. Errors in θ and ϕ are frequently relatively small, but in the drag measurement context it is necessary to repeat even marginally suspect measurements. In the present test some 10-15% of excess data had to be recorded, to produce the 5100 useful points free of θ and ϕ errors.

4.6 Wake-traversing - analysis of processed data

The measurements on the traverse plane have been used to calculate the spatial distributions of the integrands in equations (2) and (3) in Fig 6b - i.e the distributions of the local drag coefficient contributions per mm^2 (C_{D_I}'' and $C_{D_{II}}''$) - on that plane. In the case of the wing wake (Fig 6a, analysis regions 1-5) the overall C_{D_I} and $C_{D_{II}}$ contributions are each calculated in two stages, the first being a process of vertical stripwise integration yielding the spanwise variation of $C_{D_I}'(y)$ and $C_{D_{II}}'(y)$, (Figs 11 and 12) the second being a process of spanwise integration. In the case of the strut wakes it is convenient to define $C_{D_I}'(z)$ (Fig 13) and $C_{D_{II}}'(z)$, and the order of integration is reversed.

All these integration procedures are incorporated in the computer software available, trapezium rule techniques being employed. However, as with the spanwise integration

of lift (section 3.3), the definitive value
$$\int_{-1}^{+1} C_{D_I}'(y) d(2y/b) = \overline{C_{D_I}'}(y)b = C_{D_I} = 0.02287$$

for the wing wake has been derived by graphical integration of large scale plots. The 1.7% disparity from the computer integration is largely attributable to the omission of a small number of anomalous C_{D_I}' datapoints from the analysis. The spanwise mean value of drag coefficient contribution per unit run for the wing wake $\left(\overline{C_{D_I}'}\right)$ has been used to normalise the profile drag data presented in Figs 11 and 13.

The spanwise integration of the vortex drag data has been performed using a computer procedure. Fig 12 shows the spanwise variation of $C_{D_{II}}'(y)$; again the data have been normalised using a spanwise mean value $\left(\overline{C_{D_{II}}'}(y)b = 0.00937\right)$ appropriate to the wing wake (Fig 6a, analysis regions 1-5).

Maskell's theory, in the form presented in Ref 1, assumes that on the upstream reference plane the centreline reference total head H_0 is valid over the whole plane.

Examination of the present data shows that slightly negative total head defects ($\Delta H/q_0 = (H_0 - H)/q_0$) have been recorded outside the viscous wake, particularly towards the wing tips. Small adjustments have been made in the $\Delta H/q_0$ data (before calculation of the flow velocity components from the V^0, W^0 , and static pressure data) to compensate for this. A representative mean correction has been applied in each of eleven spanwise wing wake segments and in the strut wake regions, the correction being at most $\Delta H/q_0 = 0.0037$. These adjustments correct for the small spanwise variation of free-stream total head from the centreline reference value H_0 - and in fact correspond to the spanwise variation of H recorded in the empty tunnel (Fig 14, $z = 0$). These $\Delta H/q_0$ corrections amount to 2% of the final C_{D_I} value. No similar correction is appropriate to the $C_{D_{II}}$ and vorticity calculations.

5 EXPERIMENTAL RESULTS - GENERAL COMMENTS

5.1 Forces and moments data

Figs 3, 4a and 5 show the basic lift, drag and pitching moment characteristics for both transition-fixed and transition-free conditions. The mean C_{L_c} and C_{D_c} values recorded during wake-traversing (transition fixed) are in good agreement with the appropriate curves. All this data derives from mechanical balance measurements, and it has been corrected⁹ using conventional techniques. The support rig correction is restricted to the deduction of the model-off tare measurements (section 4.3). Correction for tunnel constraint effects on the drag polar has been made using the Glauert expression

$$\Delta C_{D_i} = \delta_0 \frac{b\pi}{C} C_L^2 \quad (6)$$

which is considered adequate for the present moderate lift application.

Fig 4b shows the low lift segment of the drag polar, which has a minimum drag point ($\check{C}_{L_c}, \check{C}_{D_c}$) at $C_L = +0.06$, $C_D = 0.0203$. In a restricted range of lift values ($0.3 < C_{L_c} < 0.6$) encompassing the traverse condition ($C_{L_c} = 0.491$), a lift-dependent drag factor value $k = 1.42$ holds for the above \check{C}_D , where k is defined by assumption of a parabolic lift-dependence of the total drag¹⁴.

5.2 General characteristics of the flowfield

The principal features of the wake are shown by the contours of constant total head defect ($\Delta H/q_0$) measured in the traverse plane, Figs 15a and 16 respectively showing the wake behind the fuselage and behind the port wing. Fig 17 shows the locus of maximum $\Delta H/q_0$ in the viscous wake from the port wing and the spanwise variation of maximum total head defect $\Delta H/q_0$. At all points on the locus $\Delta H/q_0$ is very much less than the values observed at the centres of the tip vortex cores ($\Delta H/q_0 \approx 1.4$) and considerably less than the maximum value observed in the fuselage wake ($\Delta H/q_0 \approx 0.7$).

The points A, A' and B, B' marked on Fig 15a represent the estimated locations of the vorticity maxima (Fig 15b) produced by the two pairs of vortices assumed to originate in the wing-fuselage junctions, and these four points lie in a region of moderately high $\Delta H/q_0$. The contours of highest $\Delta H/q_0$ are closely consistent with the marked locations (y,z) of the fuselage tailcone tip ('T', Fig 1) and the pitch strut pivot. The large

area of significant $\Delta H/q_0$ below the fuselage wake is largely attributable to an unfavourable interaction between the pitch strut and the fuselage. Fig 15a also shows the projections of the fuselage cross-sections at station $x = 0$ (the plane of the trailing-edge tip-tip line) and $x = -763$ mm (the plane of the wing planform apex) onto the traverse plane.

Figs 15a, 16 and 17 also show that the wing wake is significantly thinner in the vicinity of the wing root and tip than in the mid semispan region, and that this thinning is accompanied by a reduction in maximum $\Delta H/q_0$. The maximum $\Delta H/q_0$ falls towards zero as one follows the residual viscous wake round the circumference of the tip vortex core.

Figs 15b and 18 show the corresponding contours of constant local streamwise vorticity ξ (in nondimensional form) in the traverse plane aft of the fuselage and the port wing. Fig 19 shows the z value at which maximum (negative) vorticity was recorded at each spanwise station considered, together with the spanwise variation of this maximum. Disregarding the wing root region, where the ξ values were so small as to make it difficult to determine maxima, the z positions of the ξ maxima only deviate significantly from the locus of maximum $\Delta H/q_0$ (Fig 17) in the strut/wing intersection region ($2y/b \approx 0.45$). The maximum ξ value increases spanwise from root to tip, until the viscous wake becomes indistinguishable from the vortex core in ξ terms. A localised reduction in ξ occurs in the strut top region just above the point where vorticity is generated that is of opposite sign to that in the adjacent tip vortex.

Four pairs of vortices are discernible in the centre section wake (Fig 15b), all regions of significant vorticity being enveloped by the $\Delta H/q_0 = 0.025$ total head defect contour. Regions A and A', and B and B', are clearly associated with vortices respectively generated in the upper and lower wing roots; regions C and C' appear to be associated with a vortex pair springing from the forward fuselage roof, though their precise origin is unclear; finally, regions D and D' are associated with a vortex pair generated by the sharp inclined upper edges of the top of the pitch strut. The contours of non-dimensional vorticity of magnitude $|\xi \bar{c}/U_0| = 0.05$ represent the limit of vorticity resolution with the wake traverse system in this particular flowfield.

Fig 18 shows the contours of vorticity for the port wing wake and their relationship to the contour $\Delta H/q_0 = 0$ which defines the estimated 'edge' of the viscous wake. The strut/wing intersection secondary flow, containing vorticity of opposite sense to that in the tip vortex, is a prominent feature. All essential features shown in the figure are mirrored in the starboard wing wake.

The circulation γ has been evaluated on rectangular contours in the traverse plane enclosing the centres of the eight fuselage-region vortices, the strut secondary flow vortices and the tip vortices - and the results have been expressed in a form analogous to that of lift coefficient increments, as shown in the following table. Although the fuselage vortices are individually quite strong relative to the tip vortices, their net contribution to the vortex drag of the configuration (Fig 6b, equation (3)) is negligible, a result accentuated by the weighting effect of the small $\psi'(y,z)$ values in the centre section.

Nondimensional circulation ($2\gamma/U_0\bar{c}$) of vortices		
Vortex	Port	Starboard
Tip vortex	-0.280	+0.273
Strut/wing intersection vortex	+0.014	-0.016
Fuselage vortices	A', A	+0.065
	B', B	-0.011
	C', C	-0.007
	D', D	-0.026
		+0.013

Figs 20 and 21 respectively show plots of the contours of constant sidewash angle and constant downwash angle defined by the wake-traverse measurements. In both cases a pronounced increase in the magnitude of local flow angles occurs in the vicinity of the strut/wing intersection. A noteworthy feature of the latter figure is the strong upwash region that occurs on the centreline ($y = 0$) behind the fuselage. This is consistent with the existence of the strong upper wing-root junction vortices A and A' inferred from the vorticity contours (Fig 15b), such that fluid tends to flow from the upper wing surfaces up the fuselage sides, thereby thinning the wing boundary layer and the consequent wake in proximity to the fuselage.

Figs 22 and 23 show the downwash angle and total head defect ($\Delta H/q_0$) data produced by limited measurements close to the fuselage side, at stations 'A' and 'B' respectively (Fig 1). These measurements were made in an attempt to trace the path of the upper wing-root junction vortex A (Fig 15b) along the fuselage side - in the expectation that its presence would produce a significant distortion of the fuselage boundary layer and locally increased values of $\Delta H/q_0$. The figures show this expectation to have been unjustified, the measurements extending a good way into the fuselage boundary layer with a fine mesh ($\Delta y = \Delta z = 4$ mm). The downwash data in Fig 22 gives some ambiguous indication of a fuselage side vortex at station 'A' - at station 'B' (Fig 23) it appears that the vortex has migrated so far downwards that it is below the z range in which downwash measurements were made. In such close proximity to the fuselage it was not possible to null the probe fully (i.e. to roll the quadrant arm from the vertical, $\phi = 0^\circ$, position) and to determine the sidewash field. Therefore the w^0 and $\Delta H/q_0$ calculations depend on the assumption of small sidewash angles, and it has not been possible to determine the vorticity field close to the fuselage. On the basis of this limited evidence it can tentatively be inferred that the wing-root junction vortices A and A' remain highly concentrated along the parallel part of the fuselage and migrate downwards in the downwash field generated by the wing. Over the converging rear fuselage, where some degree of adverse pressure gradient exists, it is probable that the vortices A and A' diffuse rapidly and migrate rapidly upwards to their observed positions in the principal wake-traverse plane (Fig 15a&b).

Great care was taken to set the model up symmetrically with respect to the tunnel and traverse gear centreline plane ($y = 0$). In the mean the net crossflow generated by the model was small; an analysis of 720 pairs of points symmetrically disposed to port and starboard in the wake (for $\Delta H/q_0 \geq 0.05$) yielded a mean yaw of only 0.06° . It has also been found that the effective aerodynamic centreline plane of the model closely agrees with the geometric centreline plane. Examination of the locations of peak local flow angles, peak local vortex drag contribution ($C_{D_{II}}''$) and peak local profile drag contribution (C_{D_I}'') consistently locate the port and starboard vortex core centres at spanwise positions $2y/b = -0.953, +0.959$ respectively. A similar procedure fixes the heights of the vortex core centres as $z = 20, 24$ mm for the port and starboard vortices, respectively. This 4 mm height discrepancy (0.2% of the span) may well be attributable to small asymmetries in model dimensions in the tip regions.

Figs 24 to 27 allow further assessment of the extent of port-to-starboard symmetry in the wake, for two z heights; the $z = 0$ line approximates to the upper edge of the wake and the $z = -80$ mm line runs some little way below it. Figs 24 and 25 show the spanwise variation of downwash angle at the two heights in the traverse plane, while Figs 26 and 27 show the corresponding sidewash angle data. A high degree of port-starboard symmetry exists over the bulk of the span, the apparent asymmetry in the tip regions being attributed to the above mentioned small asymmetries in vortex core location relative to the traverse gear axes.

Figs 28a-c show the variation of the three velocity components (U, v, w) along vertical and horizontal lines through the port tip vortex core in the traverse plane. For the horizontal cuts only a partial set of experimental data is available for the precise vortex centre height ($z = +20$ mm) and a set of data for $z = +24$ mm is additionally shown. Fig 28d shows the corresponding variations of total pressure and static pressure defect vertically through the vortex centre. Fig 28e shows the corresponding vertical variation of local streamwise vorticity (ξ); in this case some data from the starboard vortex has been shown for comparison. For both the port and starboard cuts the $\xi(z)$ data for the vortex core has been evaluated using mesh sizes of both 4×4 mm and 8×8 mm. The coarse mesh data generally defines satisfactory local ξ values, but the definition of the $\xi(z)$ curve is insufficient to define the maximum at the vortex centre adequately. (An analogous exercise on the spanwise variation of the local vortex drag contribution per unit run ($C_{D_{II}}'(y)$) showed that values calculated from coarse mesh (8 mm) data were accurate enough in themselves, but that 4 mm data were required to establish the $C_{D_{II}}'$ maximum satisfactorily.)

Fig 29 shows the variation of downwash angle along lines of constant y in the traverse plane, through the port and starboard vortex centres, and Fig 30 shows the corresponding variation of sidewash angle. The port-starboard disparities in the flow angles at stations $2y/b = -0.953, +0.959$ may result from these cuts not passing *exactly* through the vortex core centres. Downwash data have been plotted on Fig 29 for y cuts 0.6% semispan outboard of and 0.4% inboard of the cut most nearly passing through the port vortex core centre, to demonstrate the large spanwise variation of downwash profile in the core region.

Fig 3l shows the contours of constant total head defect ($\Delta h/q_0$) established in a survey of the port strut guard leakage plume in the principal traverse plane; a similar picture was obtained on the starboard side. At its minimum z position (-800 mm relative to the current tip-tip line) the traverse gear indicated the upper edge of a rather smaller plume from the pitch strut guard. These plumes are produced by the spillage of low energy fluid over the top of the strut guards; this fluid originates outside the tunnel and is drawn up the gaps between the struts and their windshields (or guards) by the sub-atmospheric pressure level in the working section. Clearly no significant portion of the momentum defect in these plumes is attributable to drag on the exposed portions of the struts.

6 EXPERIMENTAL RESULTS - WAKE-TRAVERSE DRAG

6.1 General comments

Fig 11a&b show the spanwise variation of local C_{D_I} contribution from the wing and fuselage wakes, while Fig 12a-c show the corresponding $C_{D_{II}}$ data. Fig 13a&b show the variation of C_{D_I} contribution along the main struts and the pitch strut respectively, there being no perceptible $C_{D_{II}}$ contribution from the strut wakes. All this data is normalised with respect to the spanwise mean values of local C_{D_I} or $C_{D_{II}}$ contribution, these means being calculated on the basis of exclusion of strut drag contributions and of inclusion of the estimated strut-on-model interference effects.

The wake of the model and its support rig have been divided into arbitrary analysis regions (Fig 6a, Table 4). Inevitably the drag increments measured in the fuselage and wing wake regions will include contributions from short lengths of the three struts, and from the viscous interference effects of the struts on the model. The strut wake analysis regions have been specified so as to exclude all fuselage and wing wake drag contributions, together with those from the main strut/wing junction secondary flows. They include the bulk of the model-on-strut interference effects and all contributions from the readily identifiable portions of the upper strut wakes. The small drag contributions from the three unrecessed cleat fittings have been assumed negligible - the effects of the pitch-strut cleat being included in the fuselage drag, those from the main strut cleats being included in the strut-on-model interference terms.

Figs 11 and 12 show that a high degree of port-to-starboard symmetry exists in the measured spanwise distributions of local C_{D_I} and $C_{D_{II}}$ contributions. This symmetry is reflected in the integrated drag contributions for the various wake analysis regions shown in Table 4a&b. Section 6.3 details the means by which the model-alone, interference of support rig on model, and support rig (net of interference of model) drag increments have been isolated. Sections 6.4 and 6.5 detail the procedures used to apply tunnel constraint corrections and to establish the induced drag from the corrected $C_{D_{II}}$ data.

Examination of Figs 11b and 12b shows that just outboard of the main strut locations a large perturbation from the general trend occurs in both the C_{D_I} and $C_{D_{II}}$ data. The double-peak feature on the C_{D_I} distribution has been attributed partly to a contribution from the short length of main strut unavoidably included in the wing wake analysis

region (inboard peak), and partly to the secondary flow generated at the strut/wing intersection (outboard peak) (see also Fig 18).

The spatial distributions of profile drag ($C_{D_I}''(y,z)$) and vortex drag ($C_{D_{II}}''(y,z)$) contribution on the traverse plane may be inferred from the contour plots of total head defect (Fig 16) and streamwise vorticity (Fig 18) - together with Figs 11 and 12 - and it has not been considered necessary to include contour plots of C_{D_I}'' and $C_{D_{II}}''$ in this Report.

Comparison of Fig 12a - showing the spanwise variation of $C_{D_{II}}'$ in the fuselage and wing-root region - with Fig 15b - which shows a contour plot of streamwise vorticity (closely similar to $C_{D_{II}}''(y,z)$) in the same region - illustrates the relatively limited utility of the former presentation of data for flowfield diagnostic purposes. A net $C_{D_{II}}'$ of virtually zero at prescribed y can in fact be the resultant effect of a series of vorticity concentrations centred at various z positions at that y .

6.2 Comparison with mechanical balance data

The most obvious criterion of the accuracy of the wake-traverse technique is that used by Maskell¹ - namely a comparison with mechanical balance measurements. Clearly such a comparison should be made on the basis of the respective uncorrected lift and drag figures for the model together with that portion of its support rig exposed to the tunnel stream. This obviates the two subjective judgments, possibly inconsistent ones, required to extract the respective support rig and interference effects. The essential remaining assumption is that both the traverse system and the balance system are sensing the same effect. The validity of this is by no means so clear for the present configuration as for Maskell's wire support rig.

The traverse-derived drag coefficient is $C_{D_T} = 0.03875$, which includes the three auxiliary terms (ΔC_{D_I} , $\Delta C_{D_{IIa}}$, $\Delta C_{D_{IIb}}$; section 3.2). In those regions of the strut wakes where strut effects are indistinguishable from those of the low momentum strut guard leakage plumes (Fig 31), the strut drag contributions have been estimated by extrapolation of the mean $C_{D_I}'(z)$ levels in the central portions of the struts to the planes of the strut guard tops. This assumes that the leakage plumes have no material effect on the $C_{D_I}'(z)$ distributions that would be discernible in their absence. On this basis of comparison the traverse-derived drag coefficient exceeds the apparently equivalent balance-derived value (0.03866) by 0.2%.

As a further check on the general accuracy of the traverse technique it was decided to compare traverse-derived and balance-derived drag data for the two main struts in a model-off condition. (It was considered justifiable to double the traverse-derived measurement of the drag of a single strut (the starboard one, in fact) and to compare this with the balance-derived figure for an identical pair of struts.) The traverse measurements were made quite close to the strut ($x = -96 \text{ mm}$), securing advantages of measurement accuracy in a compact wake and leakage plume, and the results are shown in Fig 13a(i)&(ii) (together with model-on data, to illustrate the strong negative model-on-struts interference). The traverse-derived strut drag was calculated by graphical integration as $\Delta C_{D_I} = 0.00217$, again using the $C_{D_I}'(z)$ extrapolation procedure in the region

of the leakage plume. The corresponding mechanical balance figure was $\Delta C_{D_I} = 0.00284$. (In an empty tunnel the struts are non-lifting bodies and no appreciable $C_{D_{II}}$ effects are generated.)

The results of this comparison - giving a $\Delta C_{D_I} = 0.00067$ discrepancy for the single main strut - are shown in Table 5a; the traverse-derived drag increments relate to the same (y,z) analysis region bounds as used in model-on traverse measurements. This result makes it apparent that the two systems are not in fact sensing the same effects. It has been concluded that the balance registered a $\Delta C_D = 0.00067$ contribution attributable to buoyancy effects on the shielded portion of the strut within the strut guard. This effect is analogous to a well-established buoyancy effect on lift tares measurements¹⁰ - both effects being thought to be produced by the leakage flow into the working section through the clearance passages between struts and guards. Obviously a momentum defect relating to the buoyancy drag increment will appear in the wake-traverse plane but, like the momentum defect attributable to the lower unshielded portions of the struts, will be indistinguishable from the main leakage plume effects (Fig 31). It is not considered possible that any significant portion of the $\Delta C_D = 0.00067$ disparity is attributable to deficiencies in the $C_{D_I}(z)$ extrapolation assumptions.

It should be noted that the tares measurements (balance), model-off traverse measurements and model-on traverse measurements were made at different times, that the relative positions of the struts and their guards were likely to have varied (in ignorance of the significance of this factor) and that the $\Delta C_D = 0.00067$ buoyancy effect estimate is therefore subject to a measure of uncertainty. It was not practical to undertake a similar exercise for the pitch strut, but a reasonable estimate for the buoyancy drag increment for this would be half the above figure.

In the light of the above results it is clear that an acceptable basis of comparison between the traverse-derived drag of the model and its support rig (which involves an extrapolation to eliminate all leakage flow related effects) and the balance-derived drag, requires the latter to be net of a $\Delta C_{D_I} = -0.00167$ correction for the leakage buoyancy effects for the three struts. On this basis the wake-traverse-derived drag ($C_D = 0.03875$) exceeds the corresponding balance-derived figure ($C_D = 0.03699$) by 4.8%.

Table 2 shows a comparison between balance and traverse derived lift and drag figures for the current investigation, and for two others^{3,4} on a model (BAe 146) with 74% of the current planform reference area. The above process of deduction of leakage flow effects has been consistently applied, and in each case the data refers to the model in combination with its support rig. The balance-traverse drag disparities are worse in percentage terms than for the present model - but they are more closely comparable when expressed in absolute terms and scaled on a common reference area (that of the current model), as follows:

Model	C_{Lc}	ΔC_{Dabs} (trav-bal)	$\Delta C_D\%$ (trav-bal)	
			(a)	(b)
Current	0.49	+0.00176	+0.2	+4.8
BAe 146	0.30	+0.00232	+2.5	+9.4
BAe 146	0.61	+0.00208	+3.0	+6.5

The above tabulated data suggest that one has, within the uncertainty of the measurements, a virtually constant absolute disparity between the balance-derived and traverse-derived results. This would be consistent with an error in the traverse technique originating in a support rig effect. It is important to note that the same support rig has been employed in all three cases (though possibly with some variation of strut-guard clearance passage characteristics) - and that the one set of model-off strut traverse measurements has been used, together with each of the three model-off strut tares balance measurements, to estimate the leakage buoyancy effect in each case. Any deficiency in model-off strut traverse data would therefore be reflected as a consistent absolute balance/traverse disparity in each of the three sets of data. Columns (a) and (b) of the above table correspond to the percentage drag disparities between balance and traverse data, according as to whether the leakage buoyancy effect as quantified is respectively neglected or allowed for. A careful check of the model-off strut traverse data suggests that the latter is the correct approach, and that there is some consistent source of error in the technique as currently applied.

6.3 Extraction of support rig effects

Table 4 shows the breakdown of total traverse-derived drag coefficient (C_{Dt}) into C_{DI} and C_{DII} contributions relating to the wing and fuselage wake (analysis regions 1-5) and to the support rig (analysis regions 6-8). No attempt has been made to distribute similarly the small net contribution from the three auxiliary terms ($\Delta C_D = -0.00053$). The wing and fuselage increments include the estimated strut-on-model interference effects of the two main struts within the $C_D = 0.03224$ total. In the present simple experiment it has not been possible to quantify the strut-on-model interference contribution of the pitchstrut, which is likely to be very small, and this has been assumed to be zero. (The drag attributable to the pitchstrut cleat has been accounted to the fuselage, and that of the main strut cleats to the strut-on-model interference terms.) The support rig drag increment ($C_D = 0.00704$) comprises the model-off strut drag (less an allowance for the effects of the exposed strut tops) and the model-on-strut interference effects. It is not possible directly to identify the drag increments attributable to the short lengths of the three struts projecting into the model wake analysis regions. These increments have been estimated by extrapolation to the strut tops (Fig 13a(i)&b(i)).

The $C_{D_{I_{int}}}$ profile drag interference terms in Table 4a have been estimated by fairing-out the strut region perturbations in the port and starboard $C_{D_I}'(y)$ distributions (Fig 11a), so establishing the sum of the upper strut contributions and interference contributions. Having estimated the former by extrapolation the latter may be deduced, and in the present case the two effects are of broadly similar magnitude. The interference term quantifies the disturbance to the wing pressure field and undersurface boundary layer produced by the strut (and its cleat fitting) and the secondary flow generated by the wing/strut junction (Fig 18), so increasing C_{D_I} .

The $C_{D_{II_{int}}}$ vortex drag interference terms in Table 4(a) have been estimated by a similar curve-fairing exercise on the $C_{D_{II}}'(y)$ distributions (Fig 12b). Here a much more subjective judgment is required, to assess the mean spanwise trend of $C_{D_{II}}'$ in the absence of a strut. As with the analysis of $C_{D_I}'(y)$ one is obliged to assume that observable local perturbations represent the entire net interference effect. In fact the localised modification of shed vorticity will affect the whole spanwise load distribution, and there will be second-order interference effects on the $C_{D_{II}}'$ distribution in addition to the first-order effects one is able to identify and correct.

Table 5(a) shows the process of estimation of the leakage flow buoyancy drag increment for the main struts, discussed in section 6.2. Table 5(b) shows the build-up of the support rig drag contributions ($C_D = 0.00704$ in total) entered in Table 4(b). It is possible to estimate the model-on-strut interference drags in Table 5(b) by comparison of the model-on drag contributions (traverse data) with the model-off tare data (mechanical balance) - having allowed for the effects of the leakage flow (the pitch strut value being taken as half that for the main struts) and the exposed strut tops. In the case of the main struts this interference is negative, as is qualitatively apparent from Fig 13a(i).

In the case of the pitch strut one estimates a positive interference drag increment $C_D = 0.00098$. The $C_D = 0.00325$ total pitchstrut drag includes two contributions, denoted 'A' (0.00050, the drag extrapolation for the strut top) and 'B' (0.00088) on Fig 13b(i) - the latter being readily identifiable as an adverse interaction between the model and the pitch strut (Fig 15a), rather than a fuselage flowfield effect. In fact a pair of vortices (Fig 15b; denoted D - D') originates in this region, probably generated by separations from the sharp edges of the oblique, square-cut, aft-sloping top end of the aerofoil section pitchstrut (whose oblique end plane runs into the trailing-edge line at $z \approx -70$ mm). The extent of consistency between the inferred interference increment ($C_D = 0.00098$) and the drag increment 'B' ($C_D = 0.00088$) suggests firstly that the above separation effects are insignificant in the model-off case, and secondly that the C_D increments assumed for the exposed strut top effect (0.00012) and the leakage effect (0.00033) were not seriously unrealistic.

6.4 Tunnel corrections

Table 3 shows a comparison between the total corrected mechanical balance drag ($C_{D_{c_{bal}}}$) and the equivalent traverse figure ($C_{D_{c_{trav}}}$). The corrections for tunnel constraint and stream pitch ('E'), solid blockage ('F'), empty tunnel streamwise buoyancy

('G'), and the omission of a correction for support rig-on-model effects are common to both sets of data. A disparity of treatment of data inevitably arises for the model-on-rig effects, and for this reason the comparison is not as meaningful or satisfactory as that in Table 2 (see section 6.2). The deficiencies of the Table 3 comparison show that a satisfactory evaluation of traverse-derived *net* model drag data in terms of balance-derived data is possible only if the latter includes comprehensive mechanical balance fares and interference measurements.

6.5 Induced drag

This has been calculated from the traverse data as shown in the right-hand half of Table 3. The measured $C_{D_{II}}$ term, taken literally as 'vortex drag' for the present investigation, is 0.00937 in coefficient form, or 0.00889 net of the two auxiliary terms (Table 4(c)). It has been argued (section 3.1) that the C_{D_I} contribution measured in the vortex cores ($\Delta C_{D_{I_{vc}}} = 0.00044$) is correctly accountable to the $C_{D_{II}}$ term, and this transfer has been made. A correction has also been applied for stream pitch (-0.00043), and the Glauert correction (+0.00179) (section 5.1) has been applied in respect of tunnel constraint effects, giving the $C_D = 0.01069$ total entered in Table 3. A further correction, for strut interference on the $C_{D_{II}}$ term, is also appropriate - giving an induced drag coefficient $C_{D_i} = 0.01079$. (Table 3 also gives the corresponding data for the configurations investigated subsequently and reported in Refs 3 and 4.)

6.6 Evaluation of results

The induced drag calculations discussed above have been repeated for the three wing-alone cases investigated at 75 m/s (Table 1)¹³, and the results are plotted in Figs 32 and 33. Since these data were insufficiently detailed in the strut/wing junction regions no strut interference $C_{D_{II}}$ term could be estimated, and the value for the wing plus body case has been used ($C_{D_{IIint}} = -0.0001$ at $C_{L_c} = 0.491$) in these three cases. The $C_{D_{I_{vc}}}$ estimates are approximately proportional to $C_{L_c}^2$, and the induced drag values are consistent with

$$C_{D_i} = \frac{k_v}{\pi A} \left(C_{L_c} - \check{C}_{L_{cv}} \right)^2, \quad (7)$$

where the minimum (i.e. zero) induced drag occurs at $\check{C}_{L_{cv}} = -0.010$ and the vortex drag factor $k_v = 1.115$.

On both the above figures the wing plus body datapoint is closely consistent with the lines defined by the three wing alone datapoints. Assuming the induced drag to have a parabolic lift dependence¹⁴, it is not possible to deduce both k_v and $\check{C}_{L_{cv}}$ on the basis of a single traverse-derived C_{D_i} value (C_{L_c} being defined by a mechanical balance measurement), for the wing plus body case. It would however be reasonable to assume that the $\check{C}_{L_{cv}}$ value is not materially altered by the introduction of a body, and accordingly estimate $k_v = 1.128$ for the wing plus body case. This result is consistent with the expectation, from standard inviscid theory, that the introduction of a body modifies the spanwise lift distribution such that k_v increases. It can be assumed that the 25%

Reynolds number disparity between the wing-alone and the wing plus body cases has no effect on the vortex drag characteristics of the wing.

Given the assumption that the minimum-vortex-drag lift for the wing plus body case is $\check{C}_{L_{CV}} = -0.010$, and the additional assumption that the strut-on-model interference on the total drag (not included in the mechanical balance data shown in Fig 4b) is insignificantly lift-dependent in the range $0 \leq C_{L_c} \leq 0.65$, then one can estimate the lift dependence of the C_{D_I} or profile drag term. The use of Fig 4b and the relations

$$C_{D_I} = \frac{1.128}{\pi A} (C_{L_c} + 0.01)^2 \quad (8)$$

$$C_{D_I} - C_{D_{I_{ref}}} = \left(C_{D_c} - \check{C}_{D_c} \right)_{bal} - \left(C_{D_i} - C_{D_{i_{ref}}} \right) \quad (9)$$

produces the profile drag variation shown in Fig 34, where $C_{D_{i_{ref}}}$ is the fully corrected vortex drag at the balance-derived minimum total drag point ($\check{C}_{L_c} = 0.06$, $\check{C}_{D_c} = 0.0203$), and $C_{D_{I_{ref}}}$ the corresponding profile drag. It is unlikely that the assumptions with regard to the negligible lift dependence of the interference effects are sufficiently invalid for the basic form of Fig 34 to be affected. The basic conclusion from the Figure is that the minimum profile drag for the wing-body case occurs at significantly higher lift ($\check{C}_{L_{CP}} = 0.35$) than either the minimum total drag condition ($\check{C}_{L_c} = 0.06$) or the minimum vortex drag condition ($\check{C}_{L_{CV}} = -0.01$). Over a limited lift range the profile drag variation can be very approximately represented by:

$$C_{D_P} = 0.0194 + \frac{k_p}{\pi A} (C_{L_c} - \check{C}_{L_{CP}})^2 \quad (10)$$

where $k_p \approx 0.4$. As for the parabolic approximation to total drag variation, a wide range of k values might be chosen according as to the closeness of approximation required within any given *restricted* C_{L_c} range.

Fig 35 shows a comparison of the spanwise distribution of local profile drag contribution ($C'_{D_I}(y)$) measured for the present wing-body case ($U_0 = 60$ m/s, $C_{L_c} = 0.49$) with that for a broadly comparable¹³ wing-alone case ($U_0 = 75$ m/s, $C_{L_c} = 0.48$), and with that for a near zero-lift¹³ case ($U_0 = 75$ m/s, $C_{L_c} = 0.08$). In all cases the data have been scaled on local wing chord (C_y), neglecting the small spanwise shift between the point of C'_{D_I} measurement on the traverse plane and the real corresponding C_y - i.e neglecting sidewash effects. In the outboard region 'B' the wing-body and wing-alone results at $C_{L_c} \approx 0.5$ agree well; the rapid fall in C'_{D_I} close to the tip (more than proportionate to the planform taper effect on C_y) is common to both sets of results and indicates substantial entrainment of wing boundary layer and wake shear layer fluid into the tip vortices. In region 'A', for the two $C_{L_c} \approx 0.5$ cases, the wing-body profile drag contributions tend to be lower than those for the wing-alone case - the disparity increasing with approach to the spanwise location of the wing-root. This effect can be associated with the strong inwash flows generated on the wing-body configuration, by wing-root vortex effects and flow convergence over the rear fuselage. The disparities

in C_{D_I}' distribution between the two $C_{L_C} \approx 0.5$ cases in the mid-semispan region are dominantly attributable to entirely arbitrary differences in the location of the wake analysis regions relative to the main features of the wake in the two cases.

In the near zero-lift case the outboard of the two C_{D_I}' maxima, discernible in the other two cases is absent. This indicates that the secondary flow normally generated at the strut/wing junction (Fig 18) is also absent - i.e that the effect is lift dependent. The low levels of C_{D_I}' shown by these data indicate a considerable net increase in profile drag for the wing-alone configuration between $C_{L_C} = 0.08$ and $C_{L_C} = 0.48$.

The following two figures extend the comparison between the Ref 13 wing-alone results and those from the current wing-body tests. Fig 36 shows that there is a consistent trend of peak C_{D_I}' with lift, the peak value being consistently smaller in the port vortex core. The inverse effect is apparent in the $C_{D_{II}}'$ results (Fig 12c) for the wing-body case, and it may be recalled from the table in section 5.2 that in this case the port vortex circulation was of marginally greater magnitude than the starboard. Fig 37 shows that the vortex core span for the wing-body case is somewhat less than for the wing-alone configuration at the same lift, though clearly part of the difference relates to the traverse plane being 1.6 tip chordlengths further downstream in the former case.

7 EXPERIMENTAL RESULTS - WAKE-TRAVERSE LIFT

7.1 General comments

The basic procedure for calculating the model lift has been summarised in section 3.3, section 3.4 describing the evaluation of the adjustment for the strut circulation effects not considered in the original analysis¹. This adjustment contributes 4.6% of the final traverse-derived lift ($C_{L_t} = 0.485$, uncorrected for tunnel constraint effects), which falls 1.2% short of the corresponding balance-derived figure (Table 2). It should be noted that this adjustment does not imply an attempted correction for strut interference effects, either on the total lift or its spanwise distribution.

Fig 7 shows the spanwise distribution of local vertical component momentum defect measured in the traverse plane. In global terms this is equivalent to the configuration lift but, because of crossflow effects, the C_{L_y} distribution shown does not necessarily reflect the actual spanwise lift distribution on the wing itself - particularly in the centresection region. The total lift contribution from the port wing wake analysis regions is 1.7% greater than the equivalent starboard contribution, and the tip vortex circulation data tabulated in section 5.2 shows a 2.6% discrepancy of consistent sense in vortex strength.

Fig 8 shows how the local strut circulation, induced by the model, varies as a function of distance from the model and of model lift. It is clear that the distribution of circulation on the strut is strongly influenced both by the strut guard leakage plume and by the strut/wing junction vortex. It is also clear that the presence or absence of a fuselage has a strong effect on strut circulation distribution.

7.2 Evaluation of results

A comparison of balance-derived and traverse-derived lift data (Table 2) gives agreement to 1.2% in the present case, after extraction of the buoyancy induced lift tares effect. (As with the buoyancy induced drag tares effect, it is implicit that the effect is not modified by introduction of a model.) A similar order of agreement has been obtained for the Refs 3 and 4 results. Given the uncertainties involved in the strut circulation adjustment and the imprecision inherent in graphical integration techniques the order of agreement achieved is considered extremely satisfactory. On the basis of these three cases the wake-traverse technique seems entirely valid in lift derivation terms.

8 CONCLUDING REMARKS

8.1 Experimental results

Detailed traverse measurements have been made in the wake of a swept-wing model of wide-bodied transport type, at a corrected C_L of 0.491, and the results analysed in the context of the Maskell analysis - giving the drag data summarised below.

$C_D \times 10^4$	Net measured C_D	Auxiliary terms	Vortex core adjustment	Total tunnel corrections	Correction for support rig interference	Fully corrected C_D
C_{DI}	228.7	-0.5	-4.4	-12.8	-4.4	206.6
C_{DII}	93.7	-4.8	+4.4	+13.6	+1.0	107.9

The wake-traverse data has been compared with tunnel mechanical balance data, and found to be 1.2% lower on lift and 4.8% higher on drag. The comparison was made on the basis of data applicable to the model and its support rig combined, before application of any of the conventional tunnel corrections. To achieve a proper basis of comparison it is necessary to remove strut guard leakage plume effects from the traverse data, and to deduct the leakage flow buoyancy effects on lift (measured as $\Delta C_L = 0.006$) and drag (estimated as $\Delta C_D = 0.00167$) from the balance data. It is also necessary to correct the traverse data for the effects of support strut circulation not allowed for in Ref 1.

It is by no means certain that the effects of the strut guard leakage flows have been adequately quantified in respect of drag, and that the 4.8% discrepancy mentioned above is a true representation of the accuracy achievable with the wake-traverse technique. The significance of the leakage flows was not appreciated during the main tests, the relative positioning of the guards relative to the struts may not have been satisfactorily reproduced in the supplementary tests, and there is some evidence that the buoyancy drag increments are sensitive to this positioning.

Consideration of the C_{DI} and C_{DII} results yielded by the traverse gives no indication that they should not be literally interpreted as 'profile drag' and 'vortex

drag' respectively. However, a definitive judgment can only be made on the basis of an extensive series of traverses at given C_L , with variation of Reynolds number and traverse plane location. This should certainly be done on a 'useful' configuration - a swept-wing - without the complexities of high lift devices or their deployment mechanism fairings. Comparison of the present data with the three wing-alone cases¹³ suggests that a wing-body configuration is no more difficult to analyse than a wing-alone configuration on the same support rig (involving, in the latter case, complex centre section flows generated by the necessary sting). Clearly, the resolution of the current uncertainty with regard to the strut guard leakage flows will be a pre-requisite for the above series of traverses.

The wing plus body C_{DII} data is consistent with a vortex drag factor $k_v = 1.128$ (section 6.6), assuming a similar form of vortex drag variation to that defined by the three wing-alone cases. That is with a parabolic lift dependence¹⁴ - and a near zero-lift minimum vortex drag point, at $\check{C}_{Lcv} = -0.01$ in fact. The above k_v value is in the expected qualitative relationship to that defined by the wing-alone cases ($k_v = 1.115$) where the spanwise loading will be more nearly elliptic. However, both k_v values are well above the range of k_v variation predicted by inviscid linear theory (with allowance for wing thickness effects), which gives $k_v = 1.014$ for the wing plus body case - and at most $k_v = 1.030$ for a high-lift configuration (full-span slats and 40° flaps). The disparity is clearly partly attributable to the neglect of viscosity in the predictions, but it must also be partly attributable to the assumption of a planar wake in such predictions. (Even at the traverse plane the vortex cores already lie some $0.25 \bar{c}$ above the centre of the viscous wake in the mid semi-span region.) The precise value of k_v inferred from C_{DII} data is heavily dependent on the constraint correction applied. The simple Glauert expression has been considered adequate in the present case, and its use contributes some 17% to the final fully corrected vortex drag value.

The above k_v values are derived assuming that the 'profile drag' measured in the vortex core (ΔC_{DIvc}) is dominantly a consequence of the dissipation of streamwise vorticity, and that it can accordingly be transferred to the C_{DII} term. If this had not been done the k_v values for the wing plus body and wing-alone cases would respectively have been 1.095 and 1.082, rather nearer the theoretical levels. Clearly the validity of the ΔC_{DIvc} transfer, together with the precise constraint correction applied, has an important bearing on the interpretation of C_{DII} measurements and will require detailed study before any large scale wake-traverse studies are undertaken.

An estimate has been made of the C_{DI} or profile drag variation with lift in the vicinity of the minimum total drag point ($\check{C}_{Lc} = 0.06$), on the basis of $k_v = 1.128$ and a minimum vortex drag point at $\check{C}_{Lcv} = -0.01$. This shows a minimum profile drag lift of $\check{C}_{Lcp} = 0.35$, though it is unclear as to the extent that this is fixed by section camber effects and the extent that it is fixed by wing-body junction shear flow interaction effects.

The results for the wing plus body case show that significant mutual interference effects exist between the model and the main struts. Although the separation of the

struts-on-model and model-on-struts components of the net interference is a fairly subjective process with wake-traverse data, the mechanism of the interference on the profile drag is clear. A secondary flow is generated at each outboard strut/wing intersection, presumably because the strut sectional chordline is inclined to the local surface velocity vector. It is only possible to identify and to correct for the first-order interference effects on the vortex drag term - in terms of the modification of the spanwise distribution of shed vorticity produced by the above secondary flow.

The present experiment is insufficiently elaborate to determine the pitch strut interference on the model, though it is clear that the model has a strong adverse interference on the pitch strut drag. The design of the pitch strut top and the strut/fuselage pivot/cleat has in fact been shown to be rather poor.

The wake-traverse measurements reveal two pairs of wing/fuselage junction vortices, the upper surface wing-root vortices being the stronger. The circulation of these vortices has been calculated, together with those of the vortex pair apparently springing from the forward fuselage roof, the vortex pair generated at the pitch strut top, and the two strut/wing secondary flow vortices. The three pairs of fuselage vortices are individually quite strong (up to 23% of the tip vortex circulation) but make small individual contributions (and a negligibly small net overall contribution) to the C_{DII} or 'vortex drag' term. Some doubt exists as to the precise path of the two pairs of wing-root vortices along the fuselage sides.

8.2 Experimental technique

It can be concluded that the wake-traverse drag analysis technique has considerable promise, despite the 4.8% disparity between the traverse-derived and balance-derived total drag figures. The evidence is that this disparity originates in the C_{DI} or 'profile drag' term, and may in large measure be attributable to uncertainties in establishing the strut leakage flow contribution to the measured mechanical balance drag.

Given the reasonable expectation that the origin of the above drag disparity can eventually be firmly identified, one then must consider the practicality of the technique in terms of the resources required for a typical drag analysis traverse. It is unlikely that the requirement for measurements at 5000-6000 points can be reduced significantly (although experience indicates that they can be distributed on the traverse plane to better effect) for realistic aircraft configurations. It is however almost certain that large reductions could be effected in the 100+ hours tunnel running time currently required for a traverse - by improvements in the traverse control software, and small but significant relaxations of the yawmeter nulling criteria which need not lead to appreciable loss in the accuracy of pitch and yaw measurement. Very large reductions in the data analysis workload - currently some 1000 man-hours per traverse - can be obtained by the development of quite simple computer software for the automatic plotting of processed data, particularly in contour map form.

In short the wake-traverse technique for drag analysis purposes is barely practical as implemented. However, some relatively modest further system development - principally

in the computer software and electronic control areas - the technique can be made vastly more cost-effective. It is however difficult to envisage the technique ever becoming a practical proposition for *routine*, project-related drag analysis.

In assessing the usefulness of the system in its current state of development, one must not ignore its enormous potential for general flowfield investigations and configuration diagnostic purposes. These areas are certainly the most cost-effective application of the system, and this has been demonstrated by recent vorticity and total-head-defect mapping exercises in the wakes of combat aircraft configurations fitted with leading-edge strakes.

Table 1
SUMMARY OF WAKE-TRAVERSE TESTS IN THE No. 2 11½ ft TUNNEL
(THREE-STRUT SUPPORT RIG)

Model	Body on?	A	$\Lambda_c^o/4$	U_0 (m/s)	$\Delta X/C_T$	$C_{L_{bal}}$	Number of datapoints	Test date	Remarks
Pitch wing	No	6.00	0	75	2.75	0.53	3900	2-4/75	
M 468 ^x	No	8.35	28	75	5.8	0.08	1300	6-10/75	Slat and flaps retracted
M 468 ^x	No	8.35	28	75	5.8	0.48	1800		
M 468 ^x	No	8.35	28	75	5.8	0.64	3600		
M 468	No	8.35	28	60	3.0	2.50	6600	4- 8/76	Full span slat, 80% span flap, $\delta s = \delta F = 25^\circ$.
M 468 ^{x†}	Yes	8.35	28	60	7.4	0.49	5100	5/77	Slat and flaps retracted
BAe 146 ^{x*}	Yes	9.00	15	60	8.2	0.29	4800	10-11/77	Slat and flaps retracted
BAe 146 ^{x*}	Yes	9.00	15	60	8.2	0.60	4900	4- 5/78	

* See Tables 2 and 3 for summary of lift and drag results

† See Tables 4 and 5 for detailed traverse drag results

x Transition fixed on upper and lower surfaces

Table 2

LIFT AND DRAG OF MODEL AND ITS SUPPORT RIG (UNCORRECTED) -
SUMMARY OF CASES ANALYSED IN DEPTH

Model	α_T^0	Lift data (uncorrected)				Drag data (uncorrected)				
		$C_{L_{bal}}^+$	$C_{L_{bal}} - C_{L_{tares}}$ ^(A)	$C_{L_{trav}}$ ^(B)	$\left(\frac{B-A}{B}\right)\%$	$C_{D_{bal}}^{+x}$ ^(C)	$C_{D_{I_{trav}}}$	$C_{D_{II_{trav}}}$	$C_{D_{trav}}^{(D)}$	$\left(\frac{D-C}{C}\right)\%$
BAe 146 ³ (wing and body)	1.92	0.304	0.294	0.296	+0.7	0.03340	0.03252	0.00403	0.03655	+9.4
BAe 146 ⁴ (wing and body)	5.48	0.606	0.600	0.609	+1.5	0.04326	0.03294	0.01313	0.04607	+6.5
M 468 (wing and body)	5.10	0.497	0.491	0.485	-1.2	0.03699	0.02986 [*]	0.00889 [*]	0.03875	+4.8
	Uncorrected	Uncorrected	Subtracting lift tares	Corrected for strut circulation effect	% error in wake-traverse lift	Uncorrected	Net of ΔC_{D_I} auxiliary term	Net of the two $\Delta C_{D_{II}}$ auxiliary terms	Total wake-traverse derived drag	% error in wake-traverse drag

+ Mean of values recorded on mechanical balance during traverse

x Excluding strut guard leakage flow effect

* See Table 4(c), totals of C_{D_I} and $C_{D_{II}}$ contributions

Table 3

LIFT AND DRAG OF THE MODEL, NET OF SUPPORT AND CONSTRAINT CORRECTIONS -
SUMMARY OF CASES ANALYSED IN DEPTH

Model (C_{Lc})	Mechanical balance data						Wake-traverse data						$\Delta C_D \%$ $\left(\frac{K - H}{H} \right) \%$
	$C_{D_{bal}}$	$\Delta C_{D_{con}}$ ^(E)	$\Delta C_{D_{block}}$ ^(F)	$\Delta C_{D_{buoy}}$ ^(G)	$\Delta C_{D_{tares}}$ * ^(H)	$C_{D_{C_{bal}}}$ ^(H)	$C_{D_I} - \Delta C_{D_I}$ ^(I)	$C_{D_{II}} + \Delta C_{D_I}$	C_{D_i} ^(J)	$C_{D_{rig}}$	$C_{D_{C_{trav}}}$ ^(K)		
HS 146 (0.292)	0.03567	0.00021	-0.00023	-0.00066	-0.01222	0.02277	$\begin{Bmatrix} 0.02218 \\ -0.00028 \end{Bmatrix}$	$\begin{Bmatrix} 0.00399 \\ 0.00028 \end{Bmatrix}$	0.00448	0.01038	0.02549	+11.9	
HS 146 (0.596)	0.04471	0.00142	-0.00046	-0.00066	-0.01160	0.03341	$\begin{Bmatrix} 0.02382 \\ -0.00046 \end{Bmatrix}$	$\begin{Bmatrix} 0.01315 \\ 0.00046 \end{Bmatrix}$	0.01503	0.00910	0.03727	+11.6	
M 468 (0.491)	0.03866	0.00136	-0.00052	-0.00076	-0.00840	0.03034	$\begin{Bmatrix} 0.02282 \\ -0.00044 \end{Bmatrix}$	$\begin{Bmatrix} 0.00889 \\ 0.00044 \end{Bmatrix}$	0.01069	0.00704	0.03179	+ 4.8	
(C_L constraint corrected)	Entirely uncorrected	Constraint correction (inc. tunnel stream pitch)	Solid blockage correction	Empty tunnel buoyancy correction	Model-off tares (assume $C_{D_{int}} = 0$)	Corrected balance drag	Profile drag (net of strut effects)	Uncorrected vortex drag	Corrected vortex drag	Support rig drag	Corrected wake-traverse drag	Drag disparity traverse relative to balance	

(* including strut guard leakage flow effect)

Correction of balance data: $C_{D_{C_{bal}}} = C_{D_{bal}} + \Delta C_{D_{tares}} + E + F + G$

Correction of traverse data: $C_{D_i} = C_{D_{II}} + \Delta C_{D_I}$ (vortex cores) + E

$C_{D_{C_{trav}}} = C_{D_i} + I + F + G$

Table 4

DRAG INCREMENTS MEASURED IN THE TRAVERSE PLANE

(a) Uncorrected data - wake of wing and fuselage

Region number	Analysis region	$C_{D_I} \times 10^4$	$C_{D_{I_{int}}} \times 10^4$	$C_{D_{I_{net}}} \times 10^4$	$CD_{II_{int}} \times 10^4$	$C_{D_{trav}} \times 10^4$
1	Port tip vortex	6.0	0	30.7	0*	36.7
2	Port wing	50.6	2.4	17.0	-0.6	69.4
3	Centre section	111.3	0*	0.2	0*	111.5
4	Starboard wing	50.5	2.0	17.4	-0.4	69.5
5	Starboard tip vortex	5.9	0	29.4	0*	35.3
	Totals	224.3	4.4	94.7	-1.0	322.4

(* assumed value)

(b) Uncorrected data - wakes from support rig

Region Number	Analysis region	$C_{D_I} \times 10^4$	$C_{D_{II}} \times 10^4$	$C_{D_{trav}} \times 10^4$
6	Port main strut	19.3*	0	19.3
7	Pitch strut	32.5*	0	32.5
8	Starboard main strut	18.6*	0	18.6
		70.4	0	70.4

(* including interference from model)

Table 4 (concluded)
(c) Application of auxiliary terms - comparison with balance data

Drag increment	$C_{D_I} \times 10^4$	$C_{D_{II}} \times 10^4$	$C_{D_{trav}} \times 10^4$
Totals from 'a', 'b' { wing and fuselage support rig	228.7 70.4	93.7 0	322.4 70.4
Auxiliary terms { ΔC_{D_I} $\Delta C_{D_{IIa}}$ $\Delta C_{D_{IIb}}$	-0.5 - -	- -5.5 +0.7	-0.5 -5.5 +0.7
Total wake-traverse drag measured Strut guard leakage effect, added C_D unaccounted for, subtracted			387.5 +16.7 -17.6
Uncorrected total mechanical balance drag			386.6

Table 5

ANALYSIS OF DRAG CONTRIBUTION OF SUPPORT RIG

(a) Traverse measurements in starboard strut wake (model-off)

Source of C_{D_I} contribution	$C_{D_I} \times 10^4$
Strut wake region (8)*	15.3
Wing wake region (4)	
(i) normally exposed strut length	5.2
(ii) strut top effect	1.2
Inferred leakage flow effect	6.7 [†]
Mechanical balance $C_{D_{tares}}$ [†]	28.4 [†]

(b) Traverse measurements behind complete support rig (model-on)[†]

Source of drag contribution	$C_D \times 10^4$			
	port strut	pitch strut	starboard strut	total
Strut wake regions (6,7,8)*	16.5	18.7	15.9	51.1
Wing wake regions (2,4)**	2.8	-	2.7	5.5
Fuselage wake region (3)**	-	5.0 ^(A)	-	13.8
		8.8 ^(B)		
Total C_{D_I} included in $C_{D_{trav}}$	19.3	32.5	18.6	70.4
Adding {strut top effect	1.2	1.2 ^{***}	1.2	3.6
leakage flow effect	6.7	3.3 ^{***}	6.7	16.7
Subtracting $C_{D_{I_{int}}}$ (model-on-struts)	$-(-1.2)^{\dagger}$	-9.8^{\dagger}	$-(-1.9)^{\dagger}$	-6.7
Mechanical balance $C_{D_{tares}}$	28.4	27.2	28.4	84.0

Notes:

* assuming leakage flow gives C_D increment only for guarded portion of strut+ port and starboard struts assumed to give identical $C_{D_{tares}}$ ** strut drag increments derived by extrapolation of C_{D_I}' curves to the strut extremities

*** assumed values

† deduced as the residual of the other terms

(A), (B) see Fig 13b(i)

Table 6
GEOMETRIC DETAILS OF THE MODEL

<u>Wing</u>	
Gross area	0.5523 m ²
Gross span	2.148 m
Mean chord	0.2572 m
Centreline chord	0.3810 m
Aspect ratio	8.351
Taper ratio	0.35
Dihedral	0.0°
Leading-edge sweep	30.51°
Quarter-chord sweep	28.00°
Trailing-edge sweep	19.74°
Position of the mean quarter-chord aft of the wing apex	0.3349 m
Inclination of wing reference plane to body axis	1.10°
<u>Fuselage</u>	
Diameter	0.3048 m
Overall length	2.239 m
Distance of the wing apex aft of the nose	0.7161 m
Distance of the wing apex below the body centreline	0.0368 m

LIST OF SYMBOLS

A	wing aspect ratio
b	wing span
b^l	effective span of horseshoe vortex representing wing: $b^l = L/(\rho U_e \Gamma')$
C	cross-sectional area of tunnel working section
\bar{c}	wing mean chord
c_T	wing tip chord
$c(z)$	local chord of main strut
C_D, C_L, C_M	balance-derived force coefficients, uncorrected
$C_{D_c}, C_{L_c}, C_{M_c}$	balance-derived force coefficients, corrected for all but strut interference effects
$\check{C}_{L_c}, \check{C}_{L_{cp}}, \check{C}_{L_{cv}}$	corrected lift coefficients corresponding to minimum total, profile and vortex drags
$\check{C}_{D_c}, \check{C}_{D_{cp}}, \check{C}_{D_{cv}}$	corrected drag coefficients corresponding to above
C_{D_t}, C_{L_t}	total drag and lift coefficients from traverse data (uncorrected)
C_{D_i}	corrected induced drag coefficient derived from traverse data
$C_{D_I}, C'_{D_I}, C^*_{D_I}, C''_{D_I}$	profile drag coefficient, local contribution per unit spanwise run (mm^{-1}), local contribution/spanwise mean contribution, local contribution per unit area (mm^{-2}) - wake-traverse derived
$C_{D_{II}}, C'_{D_{II}}, C^*_{D_{II}}, C''_{D_{II}}$	vortex drag coefficient, local contribution per unit spanwise run (mm^{-1}), local contribution/spanwise mean contribution, local contribution per unit area (mm^{-2}) - wake-traverse derived
ΔC_{D_I}	profile drag correction for blockage effects
$\Delta C_{D_{I_{vc}}}$	'profile drag' increment measured for vortex core, accounted to $C_{D_{II}}$ term
$\Delta C_{D_{IIa}}, \Delta C_{D_{IIb}}$	induced upwash auxiliary terms (Fig 6b), drag coefficient form
$C_{D_{I_{int}}}, C_{D_{II_{int}}}$	profile and vortex drag contributions from support rig interference, in coefficient form
$C_{D_{I_{ref}}}, C_{D_{I_{ref}}}$	profile drag and induced drag at minimum total drag condition
C_{L_y}	local lift contribution coefficient, measured in wake- traverse plane
k	constant in assumed parabolic law of total drag variation

LIST OF SYMBOLS (continued)

k_p	constant in assumed parabolic law of profile drag variation
k_v	constant in assumed parabolic law of induced drag variation
H	total head
H_{min}	minimum total head in wake at a given spanwise position
$H_{(1)}$	reference total head, undisturbed stream
ΔH	increment of total pressure defect
p	static pressure
p_0	reference static pressure, undisturbed stream
p_1, p_2, p_3, p_4	'static pressures' measured by the four side tubes of a five-hole yawmeter
p_m	tunnel plenum wall-static pressure
q_0	reference dynamic pressure, undisturbed stream
q, q_m	dynamic pressure, local dynamic pressure measured by five-hole yawmeter
δR	incremental distance in anti-clockwise sense along liftloop contour (Fig 6c)
δs	incremental cross-sectional area normal to tunnel stream
U	streamwise velocity (x-axis direction)
U_0	reference streamwise velocity, undisturbed stream
U_e	streamwise velocity, effective value produced by solid blockage effects
U^*	streamwise velocity, Betz perturbation velocity ($\frac{1}{2}\rho U^{*2} = H_0 - (H - \frac{1}{2}\rho U^2)$)
U_{circ}	local anti-clockwise velocity component, tangential to liftloop contour in traverse plane
u_0	streamwise velocity, perturbation contribution produced by solid blockage effects
v_2, v_2^0	sidewash velocity and sidewash flow angle measured in wake-traverse plane
w_2, w_2^0	downwash velocity and downwash flow angle measured in wake-traverse plane
x, y, z	streamwise, spanwise (positive to starboard) and vertical (positive upwards) cartesian co-ordinates. Origin given by intersection of line joining T/E tips with vertical C/L plane

LIST OF SYMBOLS (concluded)

Δx	increment of streamwise distance
y_s	spanwise position of main strut chordplane
y_{wr}	spanwise position of intersection of the wing trailing-edge with the fuselage
y'	spanwise limit of application of strut circulation correction to lift data ($y' = y_s$)
α, α_{ra}	model incidence, five-hole probe pitch error
γ_z	circulation round main strut, at given z
γ	circulation round arbitrary contour in traverse plane
Γ_y	circulation on a contour defined by a cut through the viscous wake and the liftloop segment on its right-hand side (Fig 6c)
Γ'	maximum value of Γ_y on a semispan
$\Delta\Gamma_{LK}$	correction for strut circulation effects (Fig 6c, section 3.3)
Δ	denoting an incremental quantity
δ_0, δ_1	constants from standard tunnel constraint theory ¹²
ε_p	roll tube angular position error for five-hole yawmeter
θ, θ_B	yawmeter pitch angle, pitch angle at nulled condition
$\Lambda_c/4$	wing sweep at quarter chord
ξ	streamwise vorticity measured at a point on the wake-traverse plane
ξ_{min}, ξ_{max}	minimum and maximum ξ values at given y
ρ	fluid density
ϕ, ϕ_B	yawmeter roll angle, roll angle at nulled condition
ψ_{ra}	five-hole probe yaw error
$\Psi(y, z)$	cross-flow stream function on traverse plane, hypothetical value if $\xi(y, z)$ is constant to infinity downstream
Ψ'	cross-flow stream function on traverse plane, value actually measured

REFERENCES

- | <u>No.</u> | <u>Author</u> | <u>Title, etc</u> |
|------------|---|--|
| 1 | E.C. Maskell | Progress towards a method for the measurement of the components of the drag of a wing of finite span.
RAE Technical Report 72232 (1972) |
| 2 | S. Goldstein (Ed) | Modern developments in fluid dynamics.
Volume 1, pp 257-63, Dover, 1965 |
| 3 | A.J. Priest | Measurements in the near-wake of a high-wing transport model at $C_L = 0.3$.
RAE Technical Memorandum in preparation |
| 4 | A.J. Priest | Measurements in the near-wake of a high-wing transport model at $C_L = 0.6$.
RAE Technical Memorandum in preparation |
| 5 | A.J. Priest | Measurements in the near-wake of a high-lift wing at $C_L = 2.5$.
RAE Technical Memorandum in preparation |
| 6 | D.A. Lovell | The development of an automatic wake-traverse system for flow-field measurements in large low-speed wind tunnels.
RAE Technical Report 80078 (1980) |
| 7 | Z.M. El Ramly
W.J. Rainbird | A computer-controlled system for the investigation of flow behind wings.
<i>J. Aircraft</i> , <u>14</u> , pp 668-674 (1977) |
| 8 | D.A. Lovell | A wind tunnel investigation of the effects of flap span and deflection angle, wing planform and a body on the high-lift performance of a 28° swept-wing.
RAE Technical Report 76030 (1976) |
| 9 | D.A. Lovell | A generalised programme for the processing of low-speed wind tunnel mechanical-balance force and moment data.
RAE Technical Report 70174 (1970) |
| 10 | D.J. Kettle | Low-speed wind-tunnel measurements of wing-strut mutual interference effects on tare loads and moments.
RAE Technical Report 74055 (1974) |
| 11 | D.W. Bryer
R.C. Pankhurst | Pressure probe methods for determining wind speed and flow direction.
pp 67-74, HMSO 1971 |
| 12 | H.C. Garner
E.W.E. Rogers
W.E.A. Acum
E.C. Maskell | Subsonic wind tunnel wall corrections.
AGARDograph 109, 1966 |

REFERENCES (concluded)

<u>No.</u>	<u>Author</u>	<u>Title, etc</u>
13	D.A. Lovell D.G. Dobney	Initial measurements with an automatic wake-traverse system (behind a swept-wing). RAE research, unpublished
14	E.C. Maskell D.A. Kirby J.Y.G. Evans	Aerodynamic research to improve the low-speed performance of transport aircraft for short and medium ranges. RAE Technical Memorandum Aero 1114 (1968)
15	E.C. Maskell	An interim note on the extension of the wake-traverse technique to the measurement of the drag of finite lifting wings. RAE Technical Memorandum Aero 1664 (1976)

-MM-

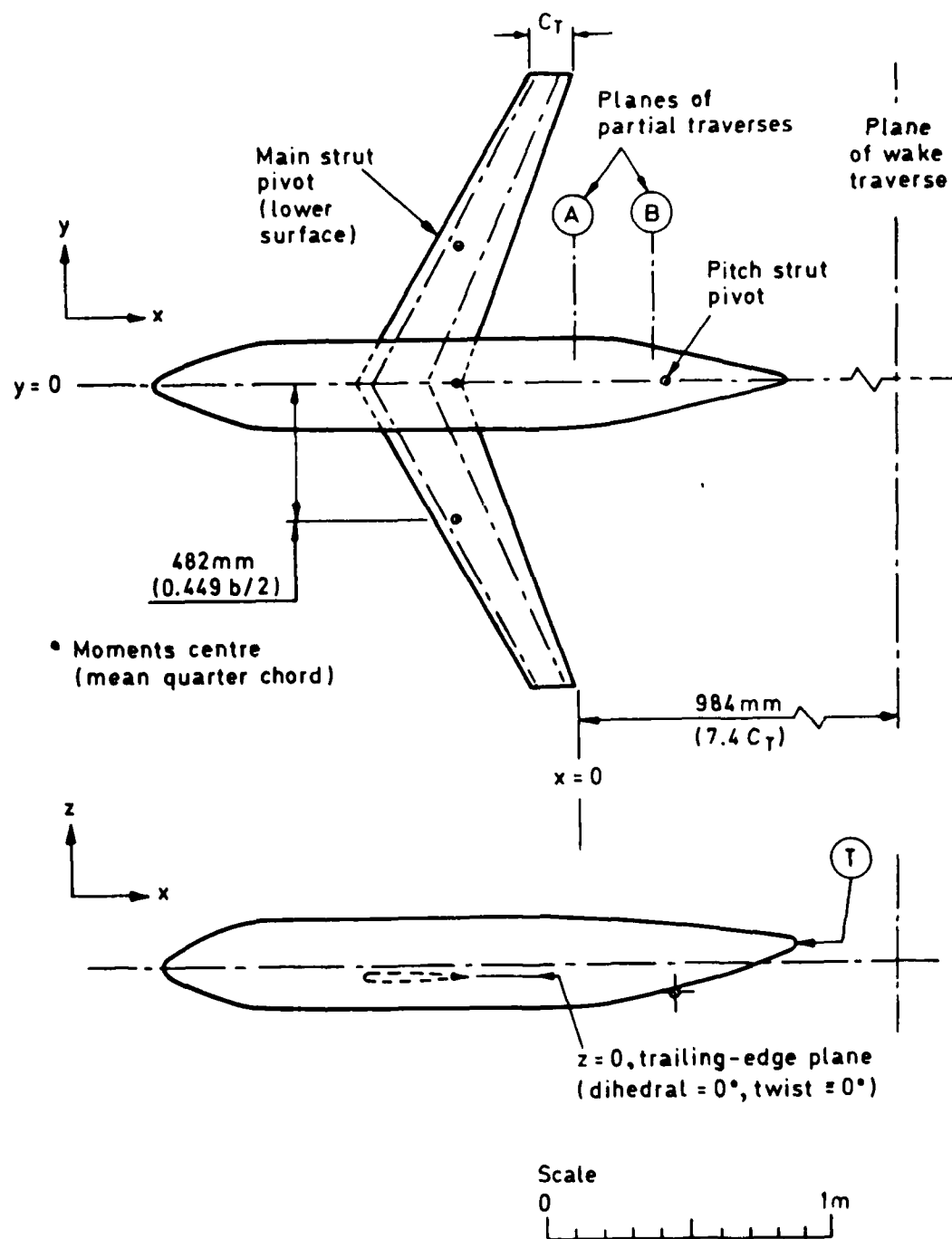


Fig 1 Schematic general arrangement of model 468

Fig 2

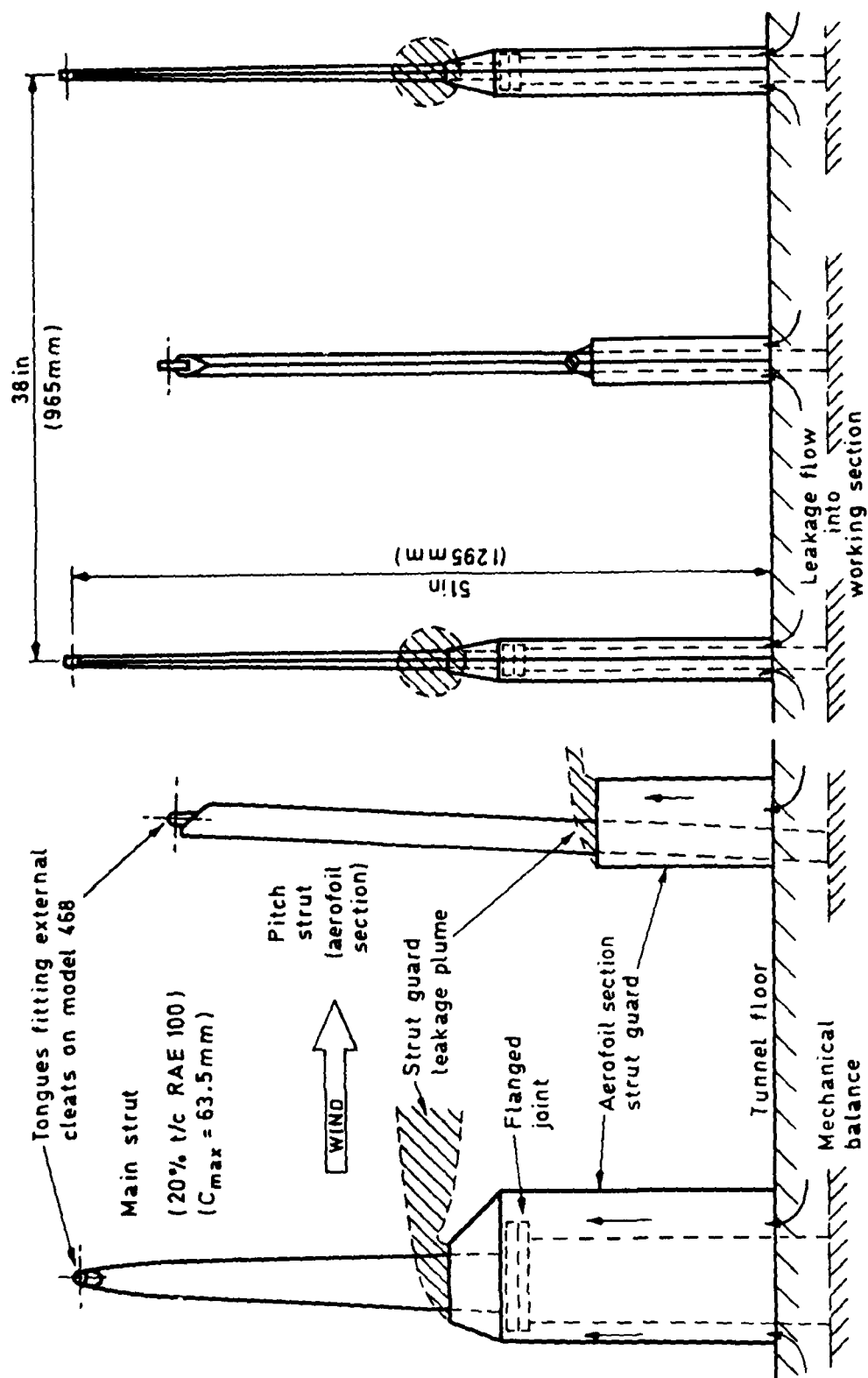


Fig 2 Schematic general arrangement of model support rig

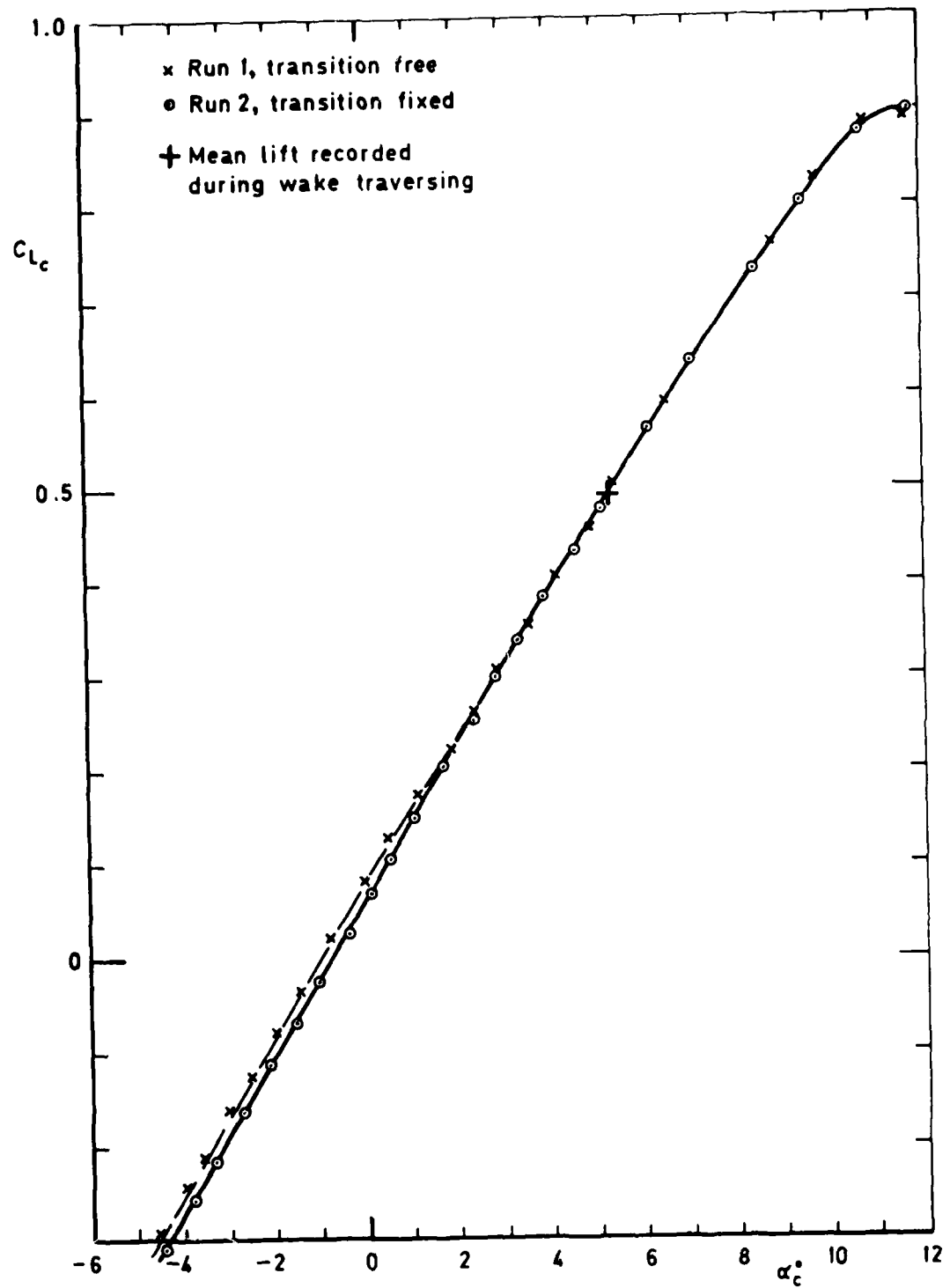


Fig 3 Effect of transition fixing on lift curve

Fig 4a

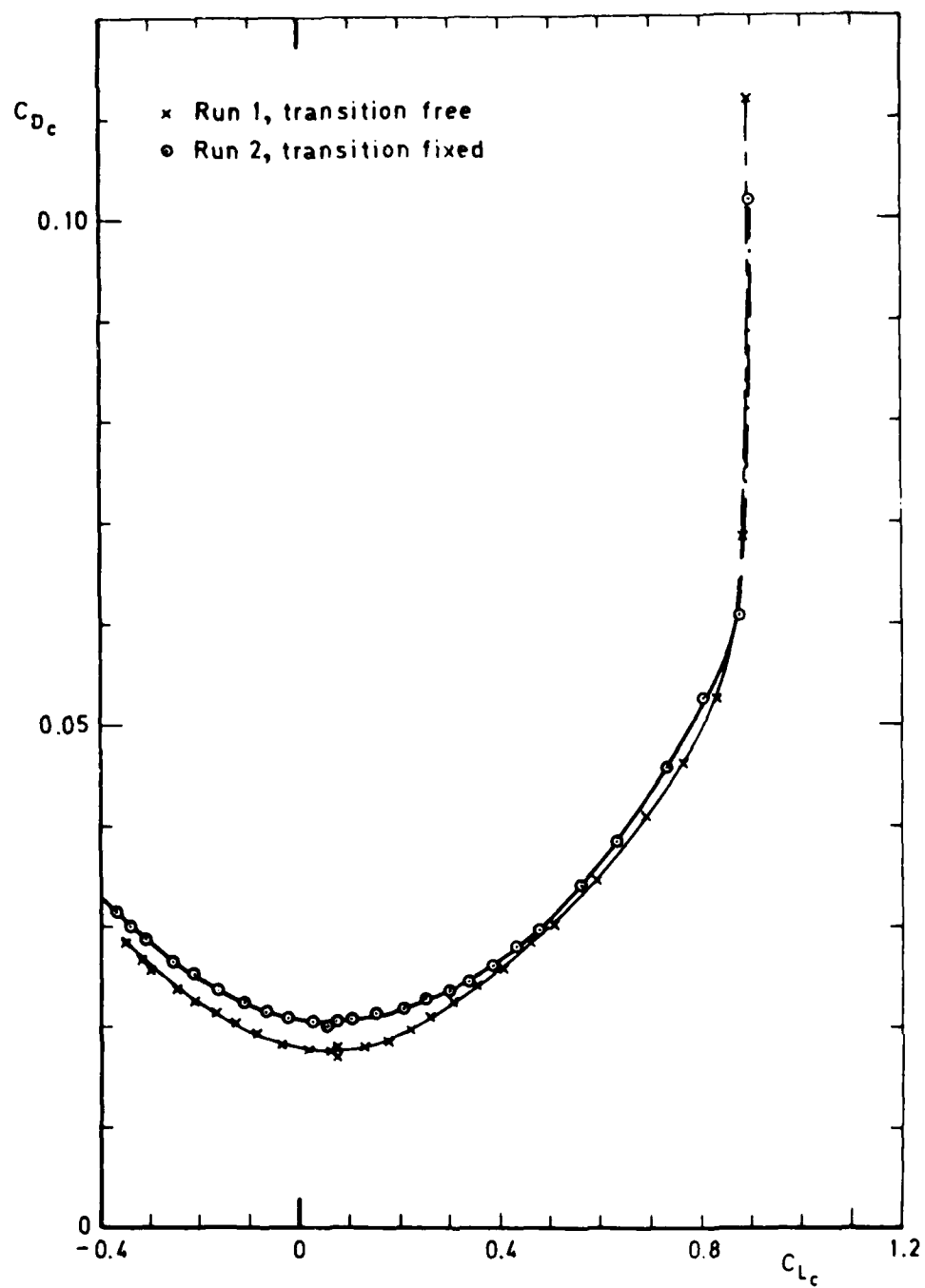


Fig 4a Effect of transition fixing on drag polar

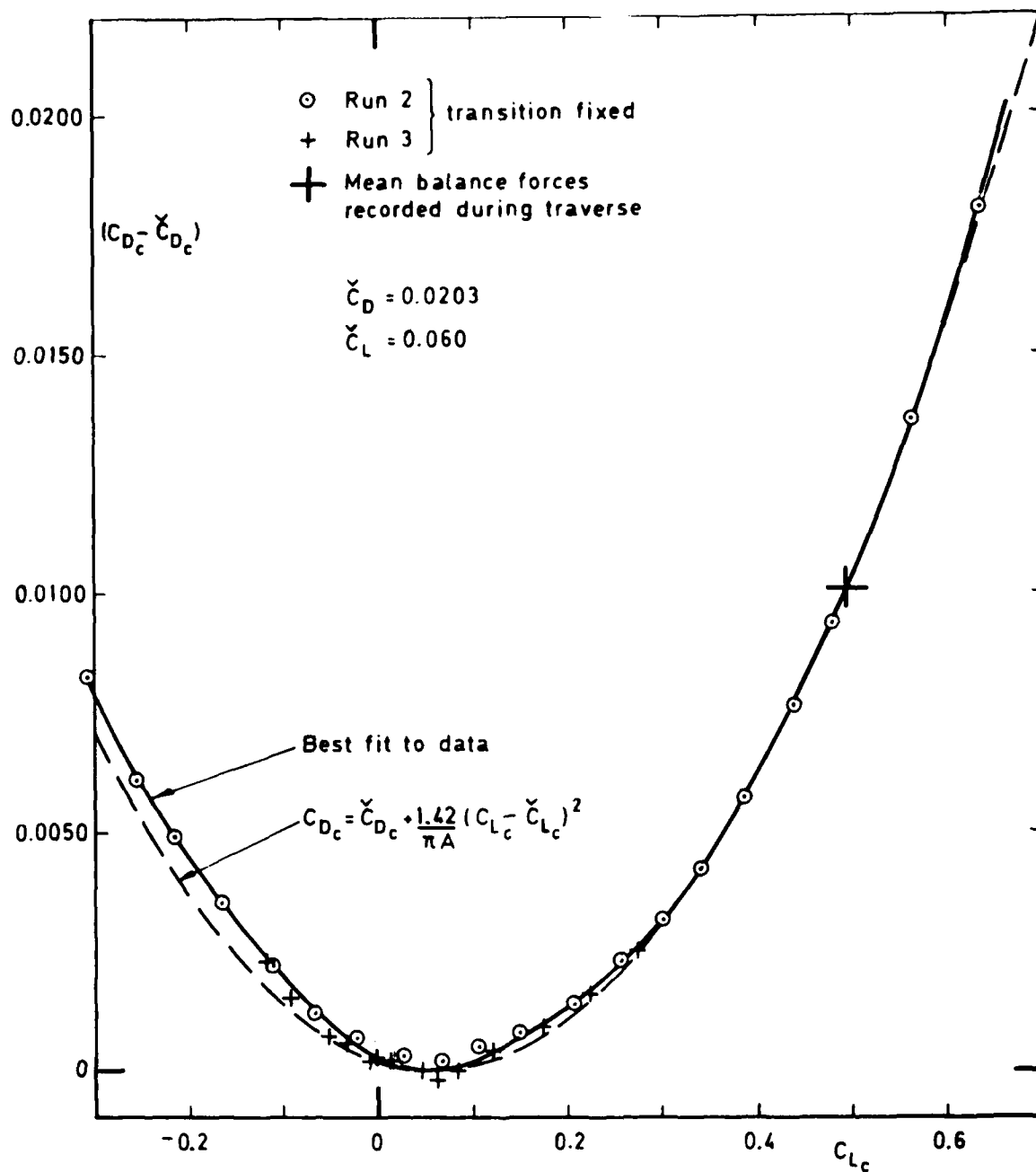


Fig 4b Low lift segment of drag polar, repeatability of data

Fig 5

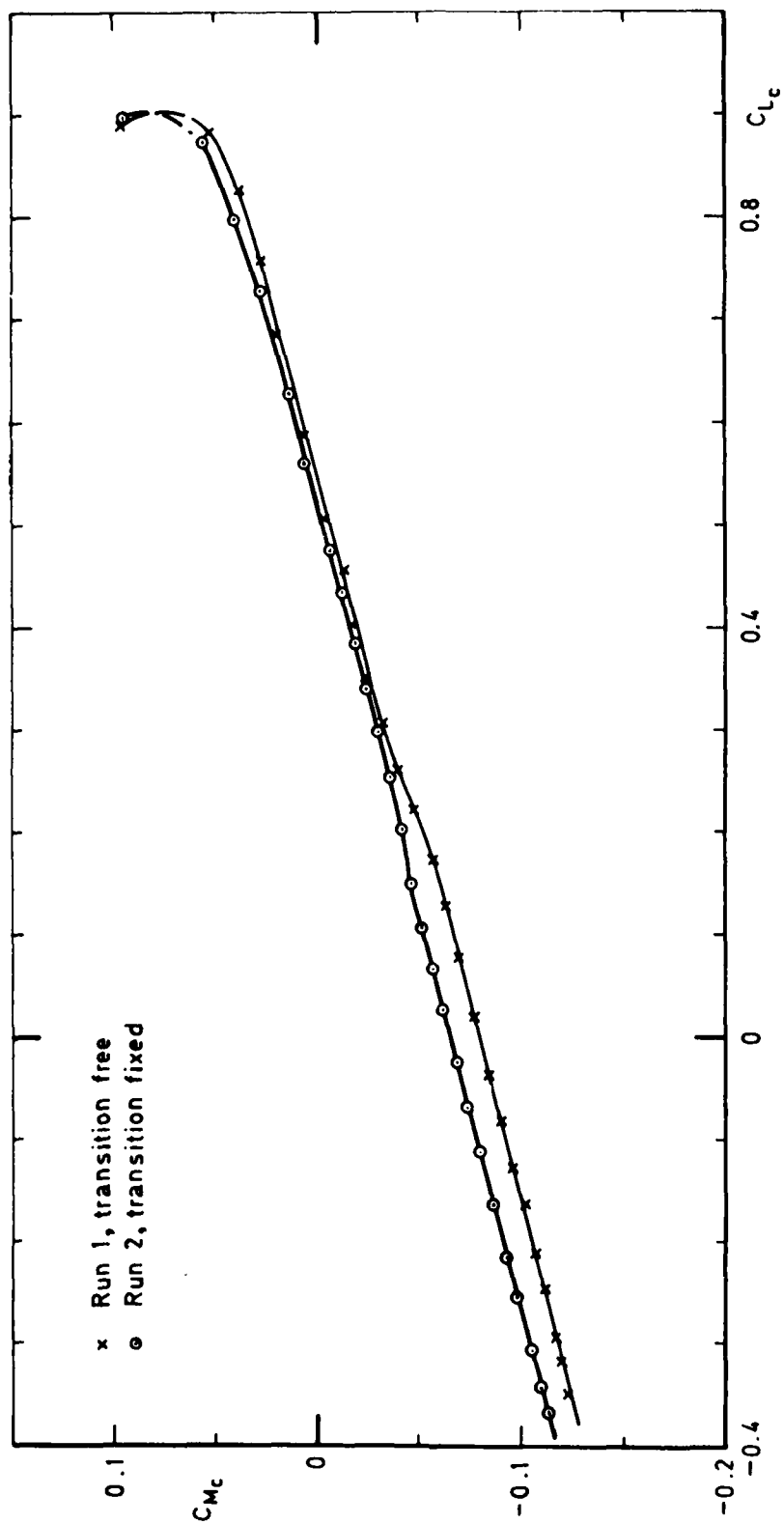


Fig 5 Effect of transition fixing — pitching moments about mean quarter-chord axis

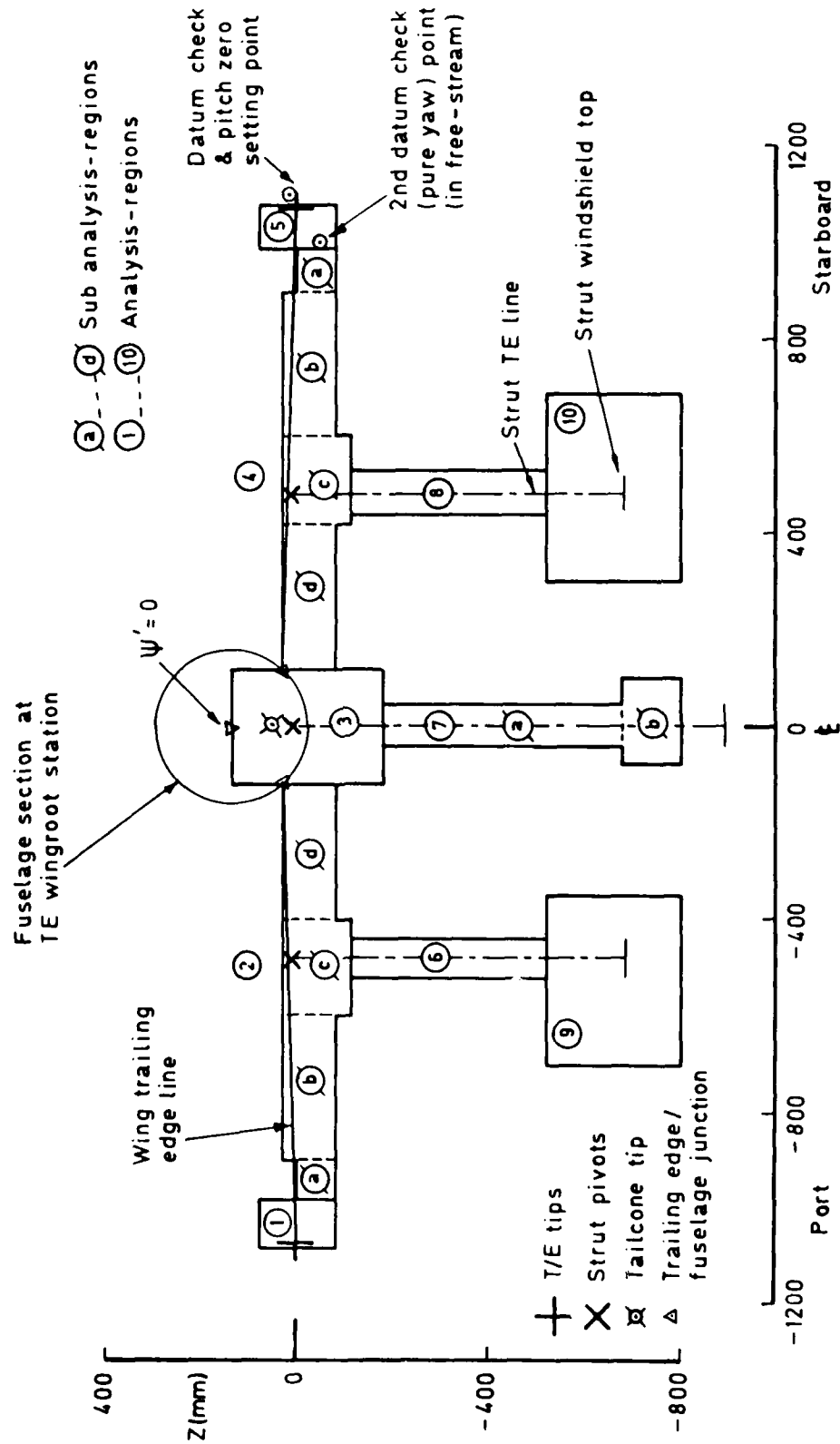


Fig 6a Diagram showing the analysis regions (bounding the viscous wake) on the traverse plane, and the locations of principal model features

$$C_{D_I} = C_{D_I} + C_{D_{II}} \quad (1)$$

$$C_{D_I} = \frac{1}{q_0 b \bar{c}} \left\{ \iint_w (H_0 - H_2) ds + \rho/2 \iint_w (U_2^* - U_2)(U_2^* + U_2 - 2U_0) ds \right\} + \Delta C_{D_I} \quad (2)$$

$$C_{D_{II}} = \frac{1}{q_0 b \bar{c}} \left\{ \rho/2 \iint_w \psi' \xi ds \right\} + \Delta C_{D_{II_a}} + \Delta C_{D_{II_b}} \quad (3)$$

Where

$$U_e = U_0 + u_0 = U_0 + \frac{1}{2c} \iint_w (U_2^* - U_2) ds \quad (4)$$

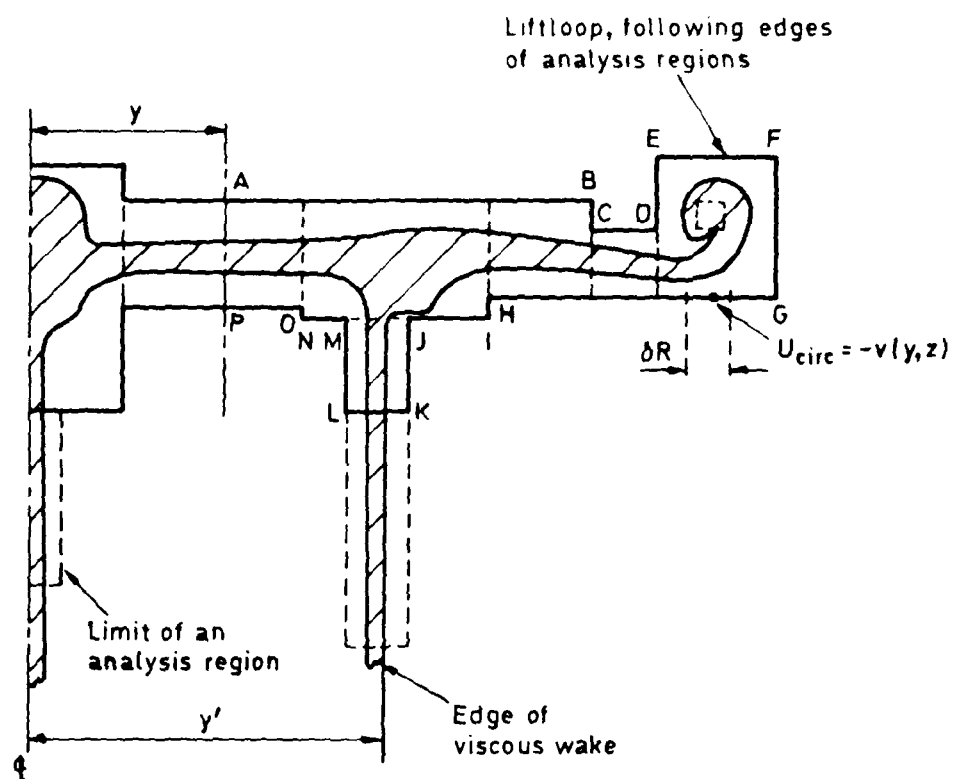
$$\frac{1}{2} \rho U_2^{*2} = H_0 - (H_2 - \frac{1}{2} \rho U_2^2) \quad (5)$$

$$\Delta C_{D_{II_a}} = - \frac{C_L}{8\pi U_e b'} \int_w \left[\frac{1}{y \cdot b'/2} \left\{ \sqrt{1 + \left(\frac{y \cdot b'/2}{x} \right)^2} - 1 \right\} \right. \\ \left. - \frac{1}{y - b'/2} \left\{ \sqrt{1 + \left(\frac{y - b'/2}{x} \right)^2} - 1 \right\} \right] \Gamma_y dy \quad (6)$$

$$\Delta C_{D_{II_b}} = -C_L^2 \left(\frac{b \bar{c}}{c} \right) \left(\frac{U_0}{U_e} \right)^2 (\delta_0 - \delta_1 \frac{x}{h}) \quad (7)$$

$$\Delta C_{D_I} = -\rho \iint_w (U_e - U_0)(U_2^* - U_2) ds = -\rho u_0 \iint_w (U_2^* - U_2) ds \quad (8)$$

Fig 6b Summary of key drag expressions



$$C_L = \int_{-1}^{+1} C_{LY} d(2y/b) \quad (1)$$

$$C_{LY} = \frac{1}{q_0 b \bar{z}} \left[\rho U_e \Gamma_Y + \rho \int (U_2^* - U_2) w_2 dz \right] + \frac{\rho U_e \Delta \Gamma_{LK}}{q_0 b \bar{z}} \quad (2)$$

$$\text{ie, } C_{LY} = \frac{1}{q_0 b \bar{z}} (\rho U_e \Gamma_Y) + \frac{\rho U_e \Delta \Gamma_{LK}}{q_0 b \bar{z}} \quad (3)$$

$$\Gamma_Y = \oint U_{circ} dR \quad (4)$$

$$\Delta \Gamma_{LK} = \text{strut circulation correction, 0 for } |y/y'| \geq 1$$

Fig 6c Division of traverse plane ($x = \text{const.}$) into analysis regions, definition of liftloop and calculation of overall lift

Fig 7

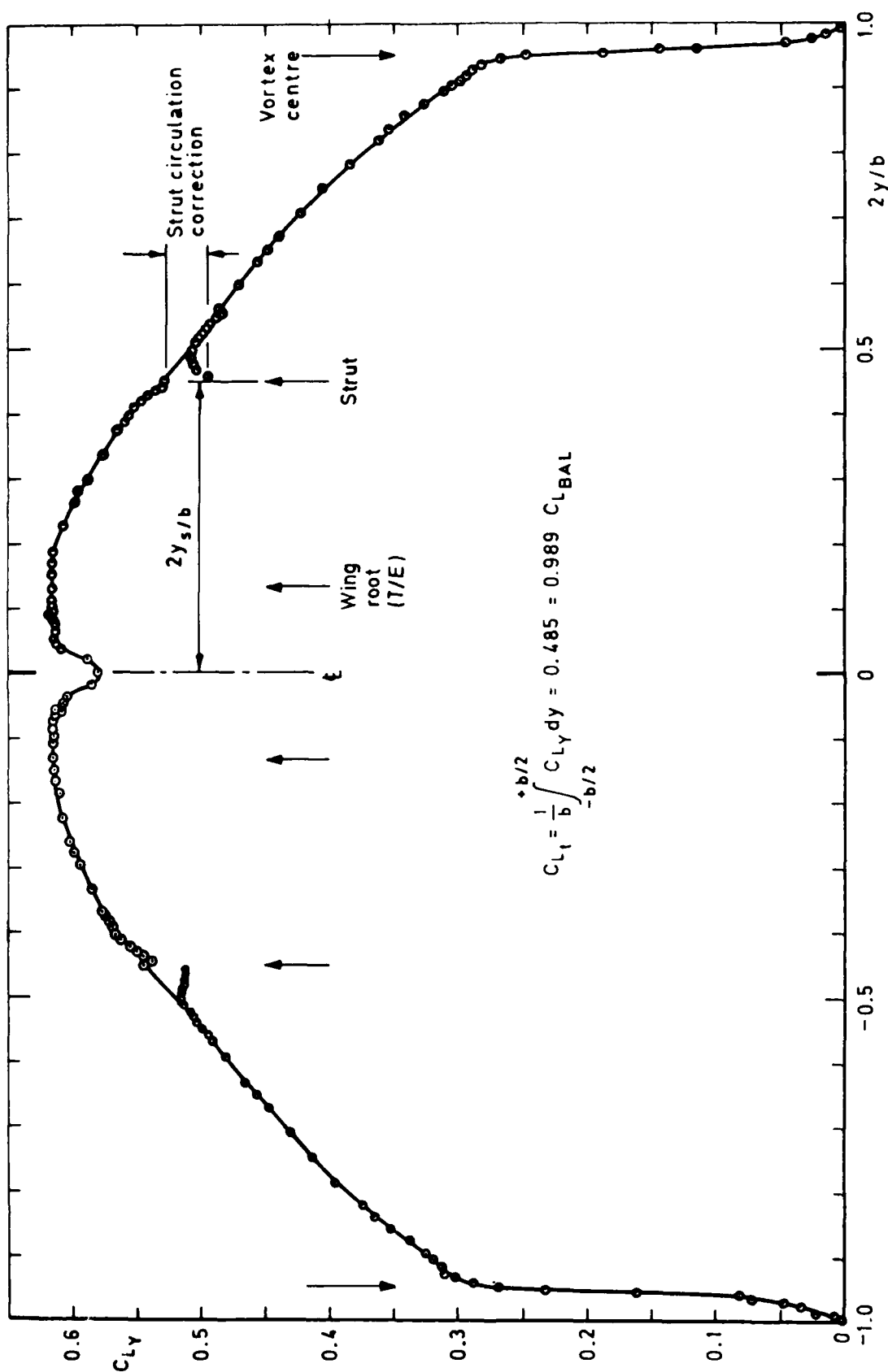


Fig 7 Spanwise distribution of local lift contribution (per unit run) measured in traverse plane

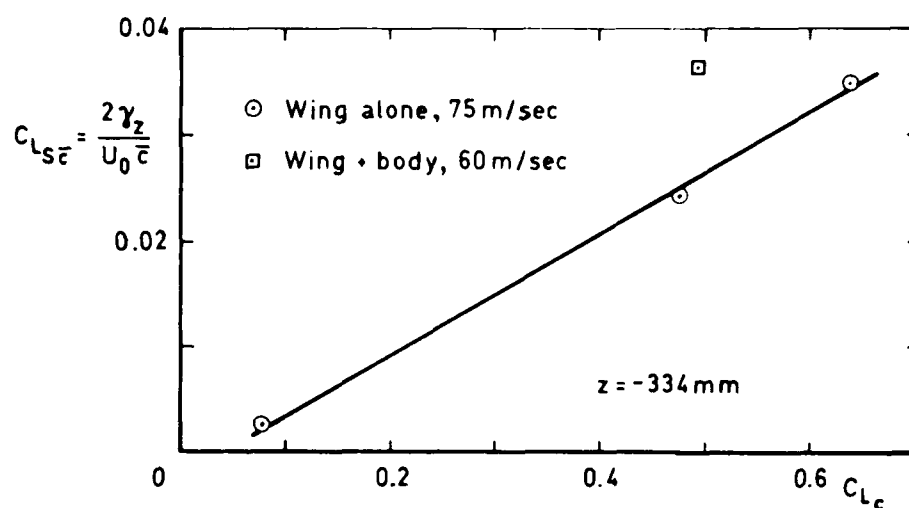


Fig 8a Variation of local lift at the mid point of the starboard strut ('A') with model lift

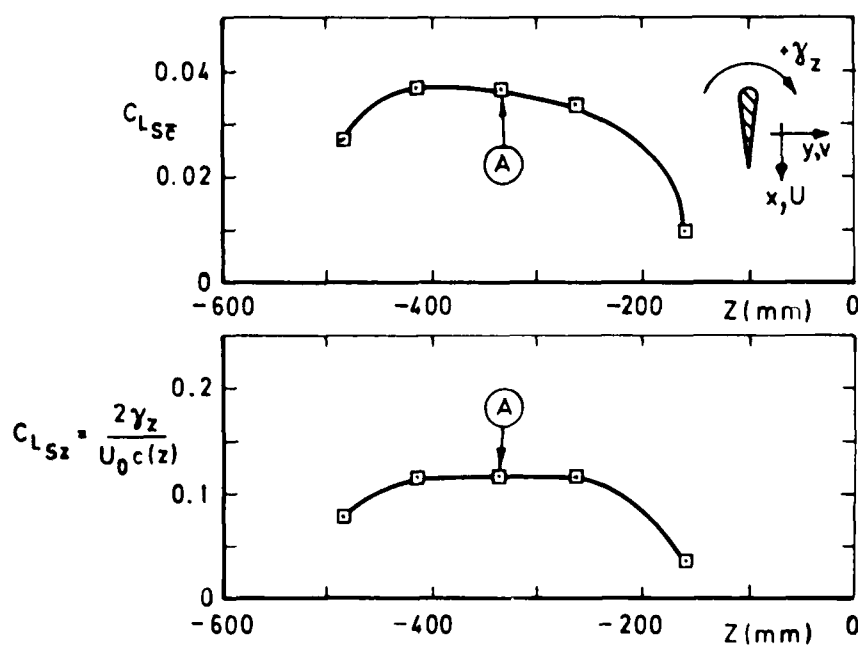


Fig 8b Variation of local lift along the length of the starboard strut at constant model lift ($C_{L_c} = 0.49$)

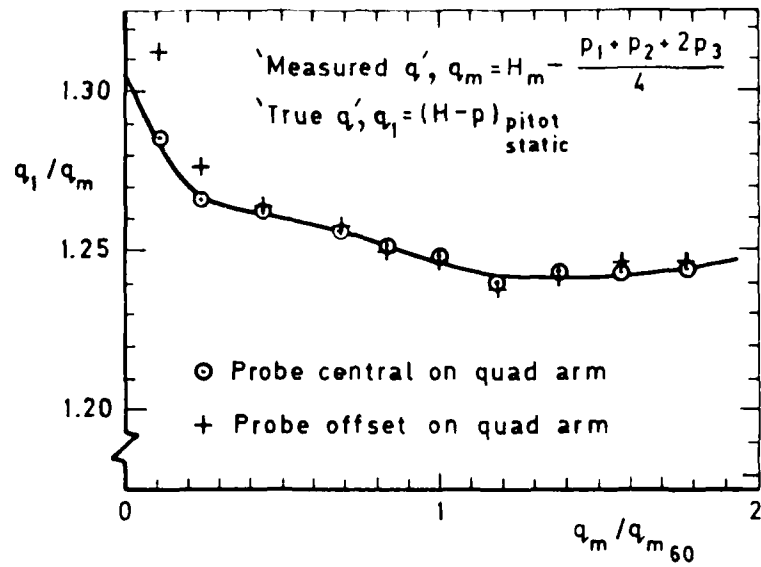


Fig 9 Five-hole yawmeter probe calibration, relationship between 'measured' and 'true' dynamic pressure

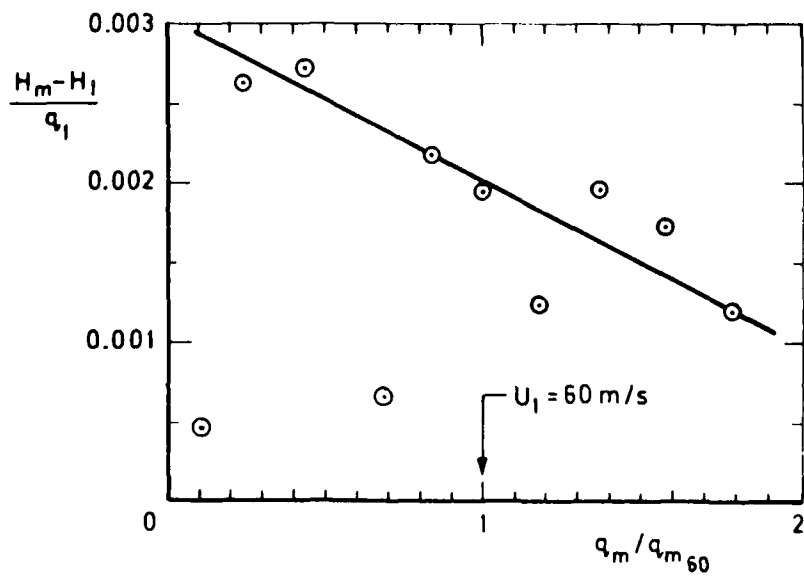


Fig 10 Five-hole yawmeter probe calibration, relationship between 'measured' and 'true' total head

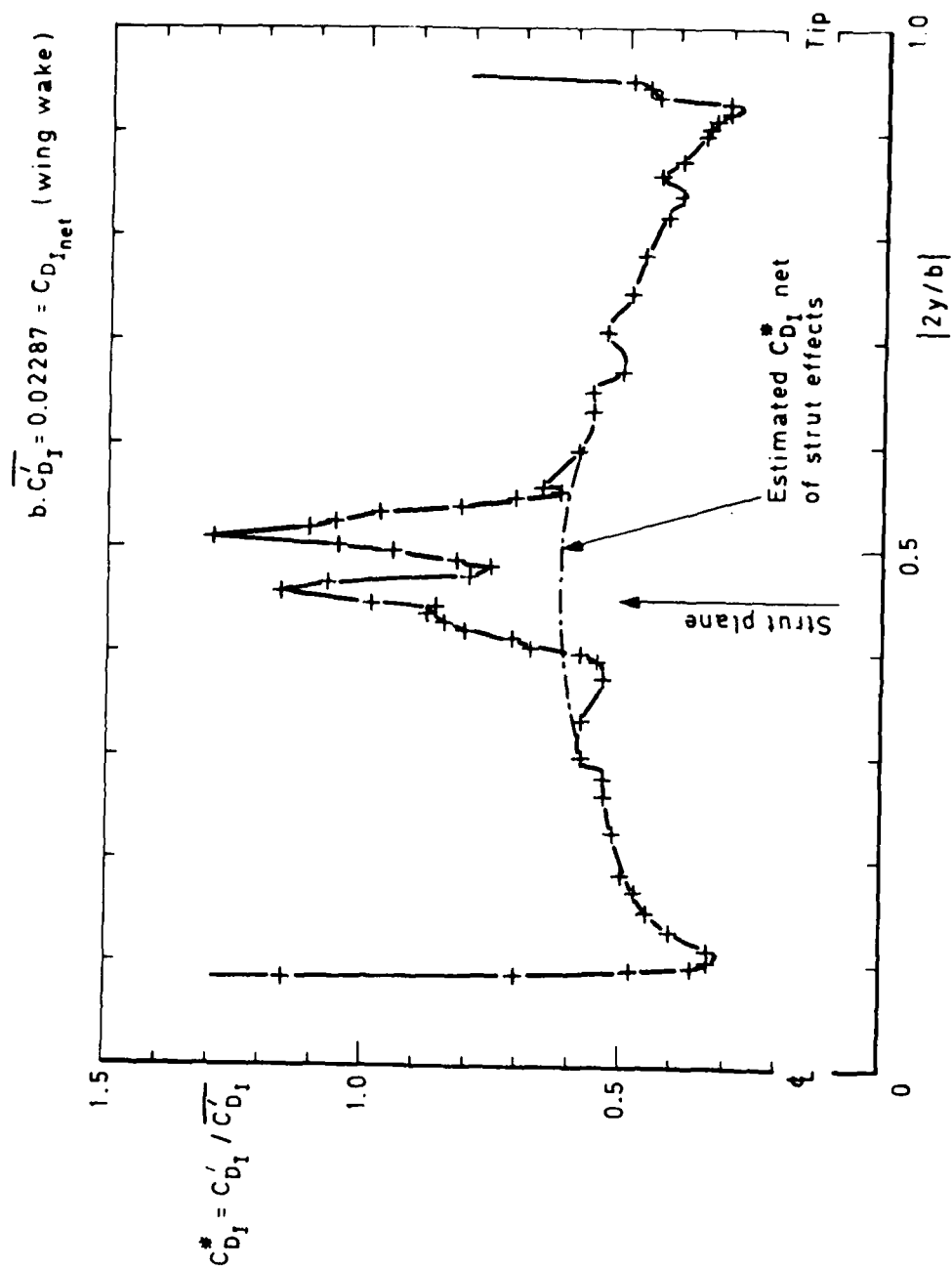
Fig 11a Spanwise distribution of local C_{D_I} contribution (per unit run) - starboard wing

Fig 11b

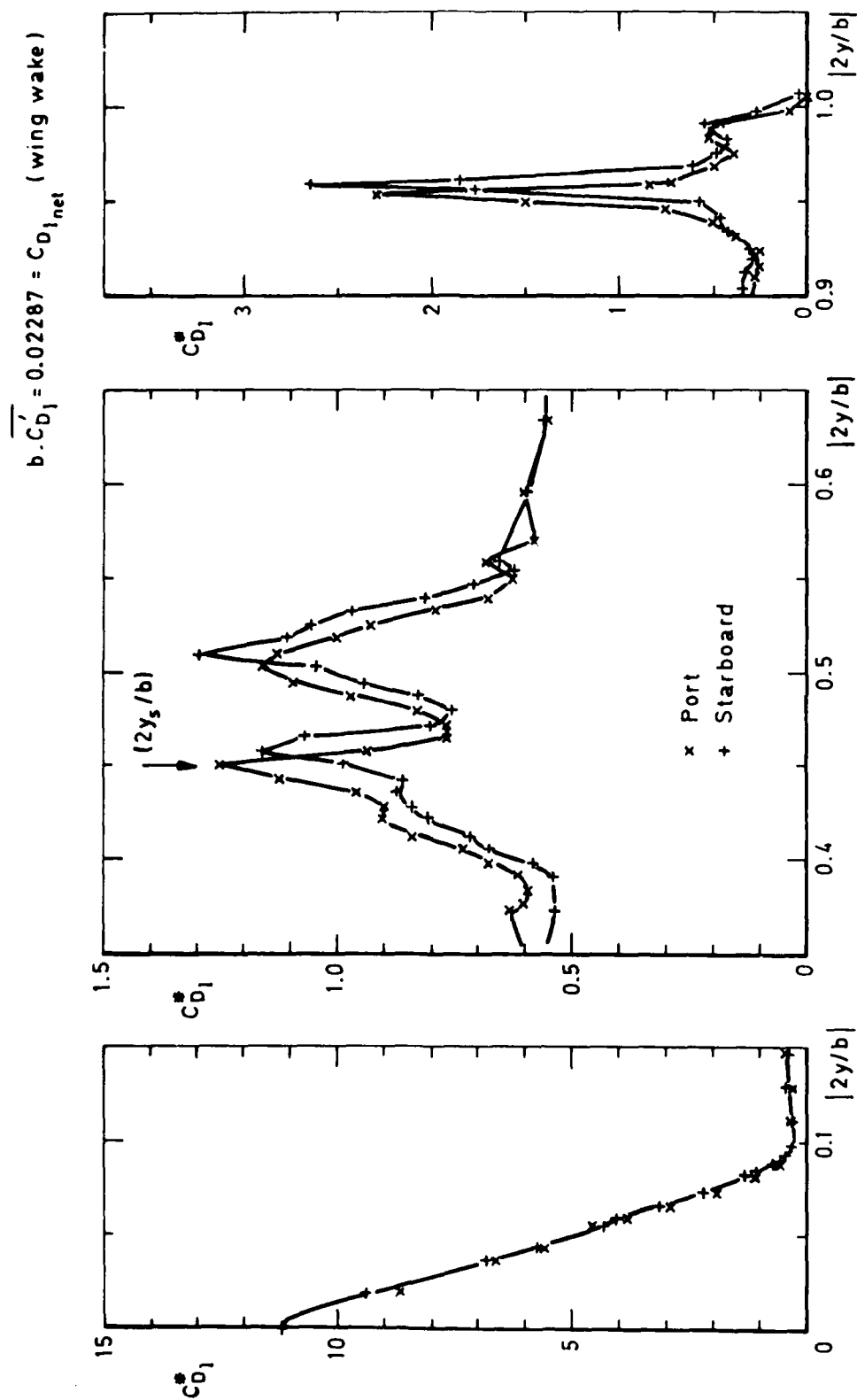


Fig 11b Spanwise distribution of local CD_1 contribution (per unit run) — port/starboard comparison

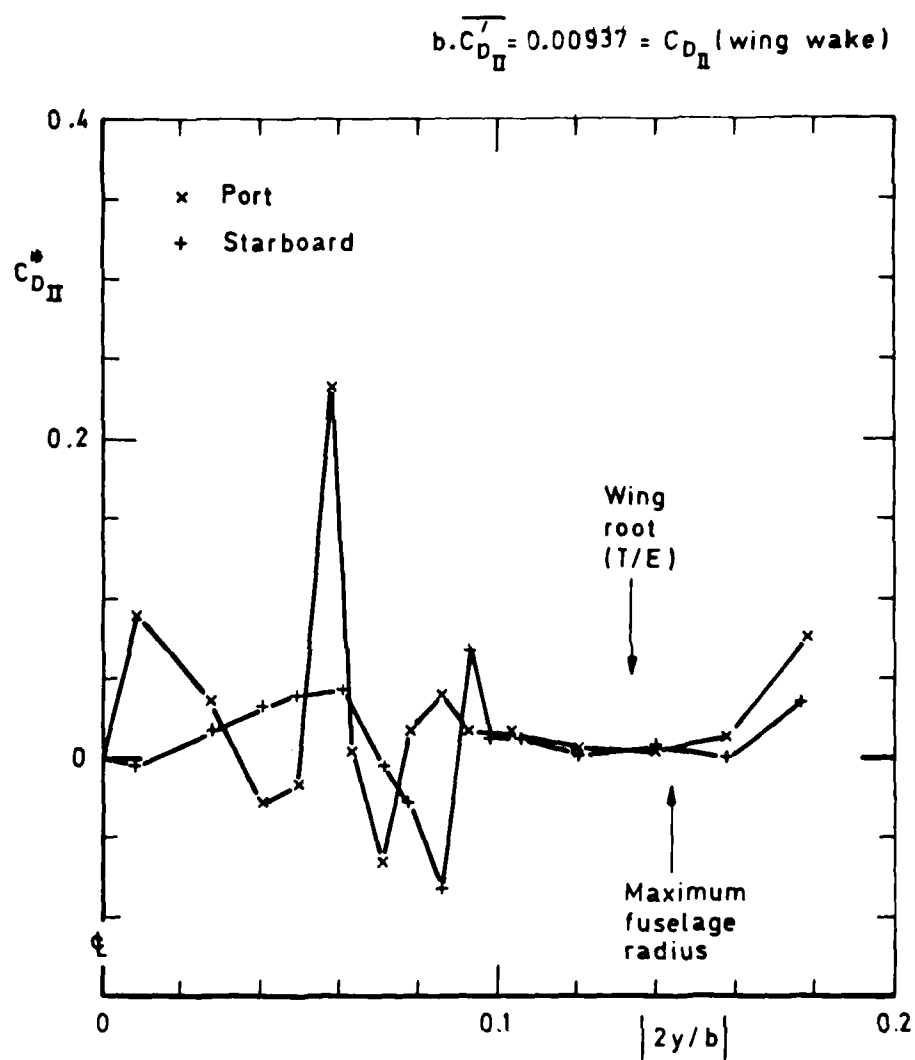
Fig 12a Spanwise distribution of local $C_{D_{II}}$ contribution (per unit run) – centre section

Fig 12b

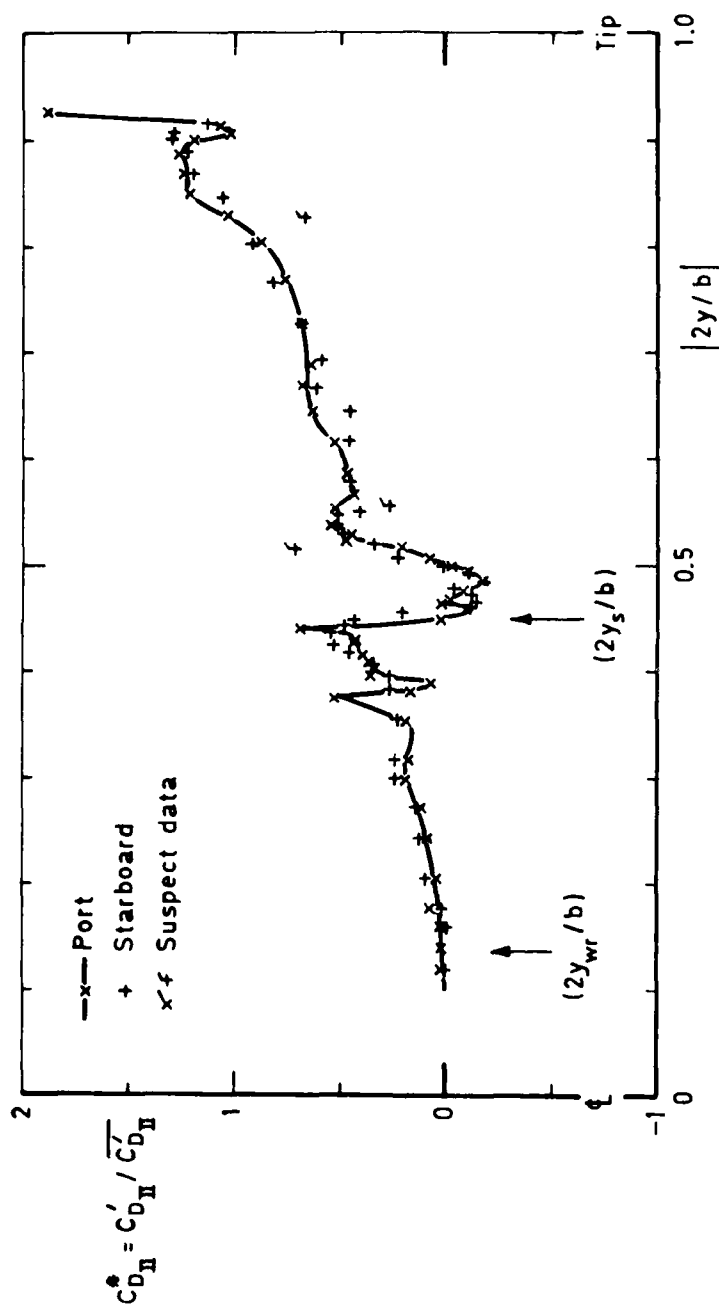


Fig 12b Spanwise distribution of local $C_{D_{II}}$ contribution (per unit run) — wing wakes

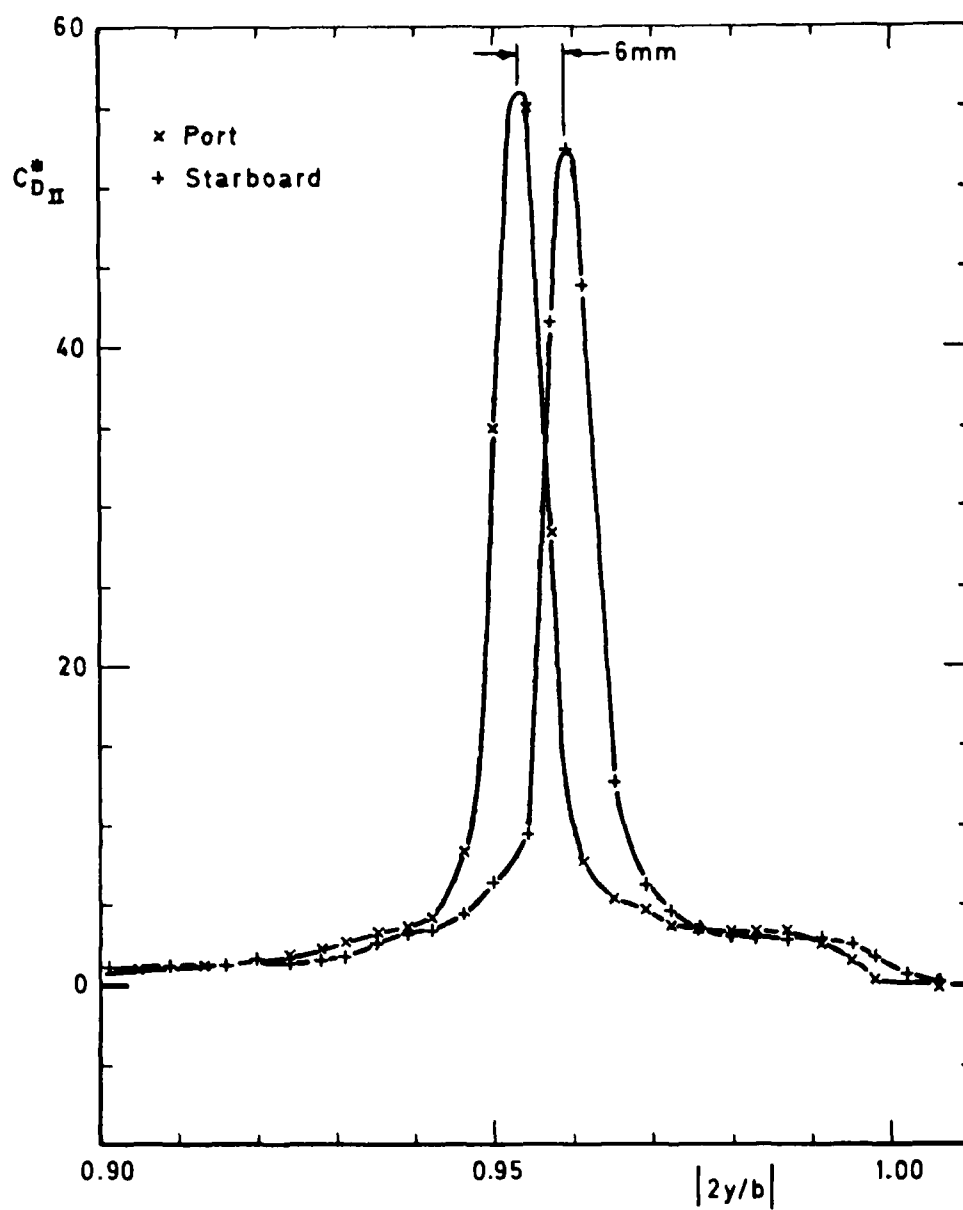
Fig 12c Spanwise distribution of local CD_{II} contribution (per unit run) — tip regions

Fig 13a

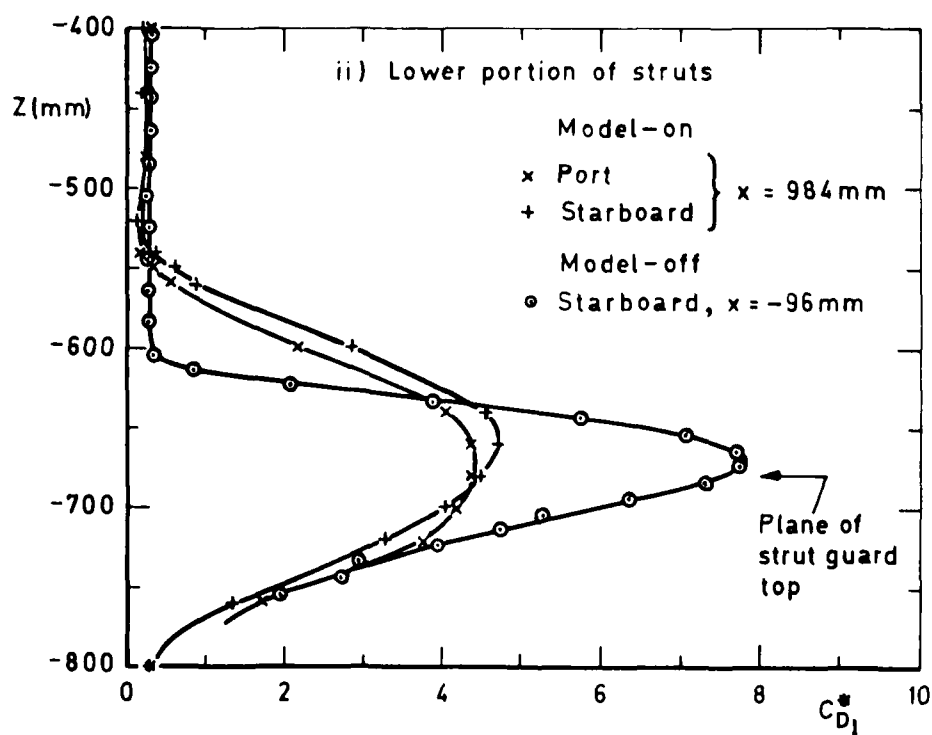
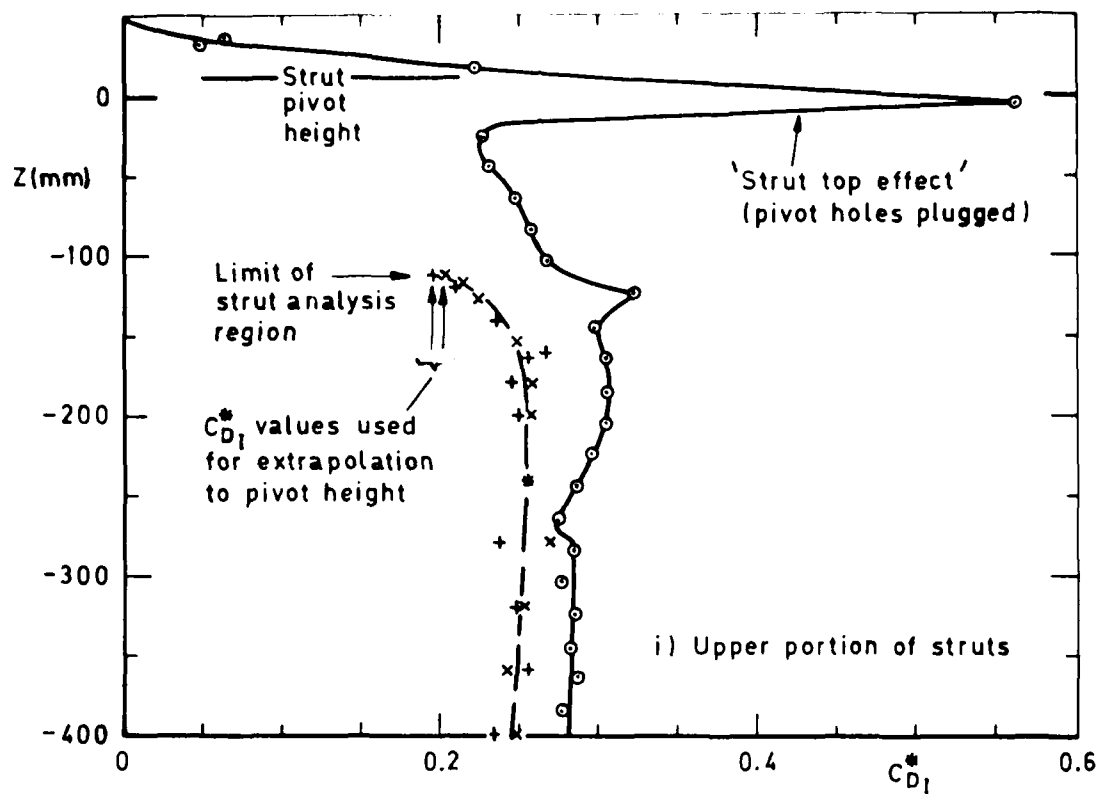


Fig 13a Distribution of CD_1 contribution (per unit run) along main struts

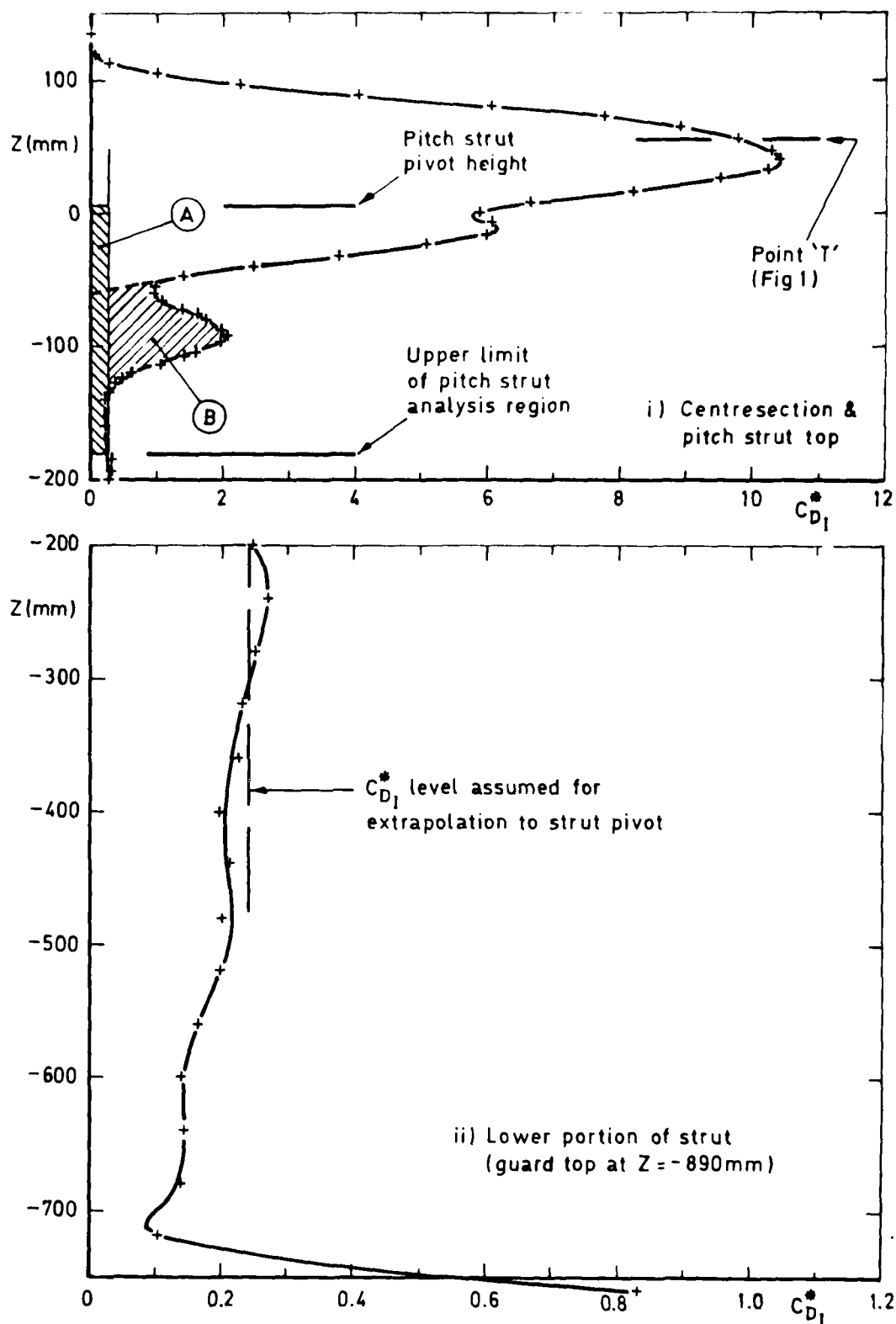


Fig 13b Distribution of $C_{D_I}^*$ in centre section ($-0.112 \leq \frac{2y}{b} \leq +0.112$) and along the pitch strut

Fig 14

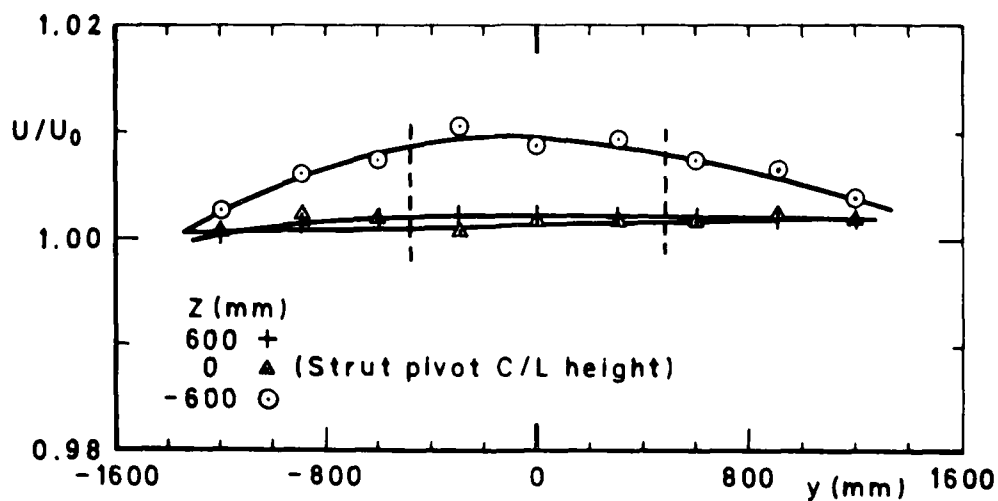
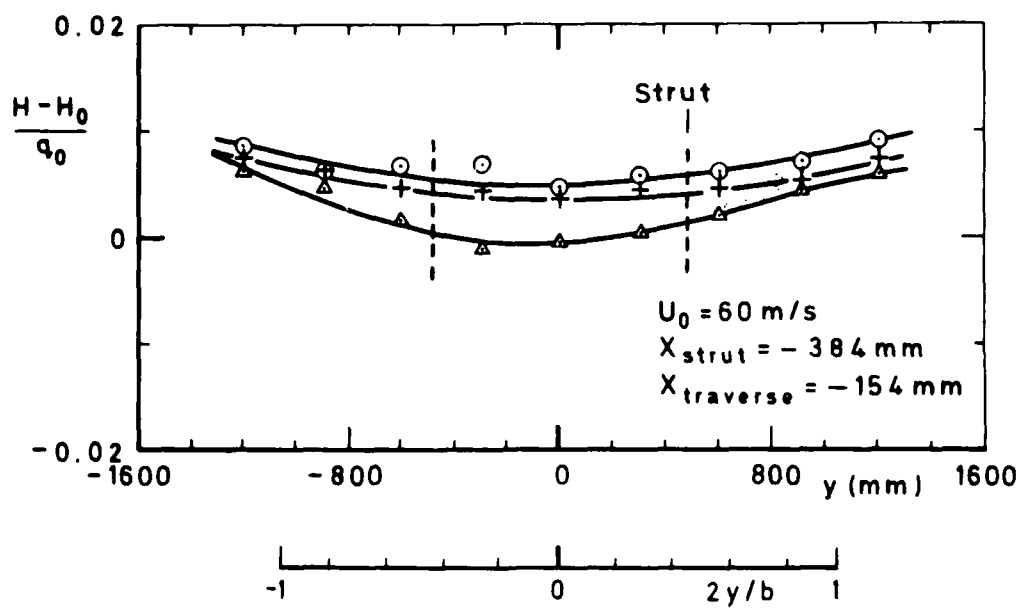


Fig 14 Variation of free-stream conditions across the empty tunnel working section

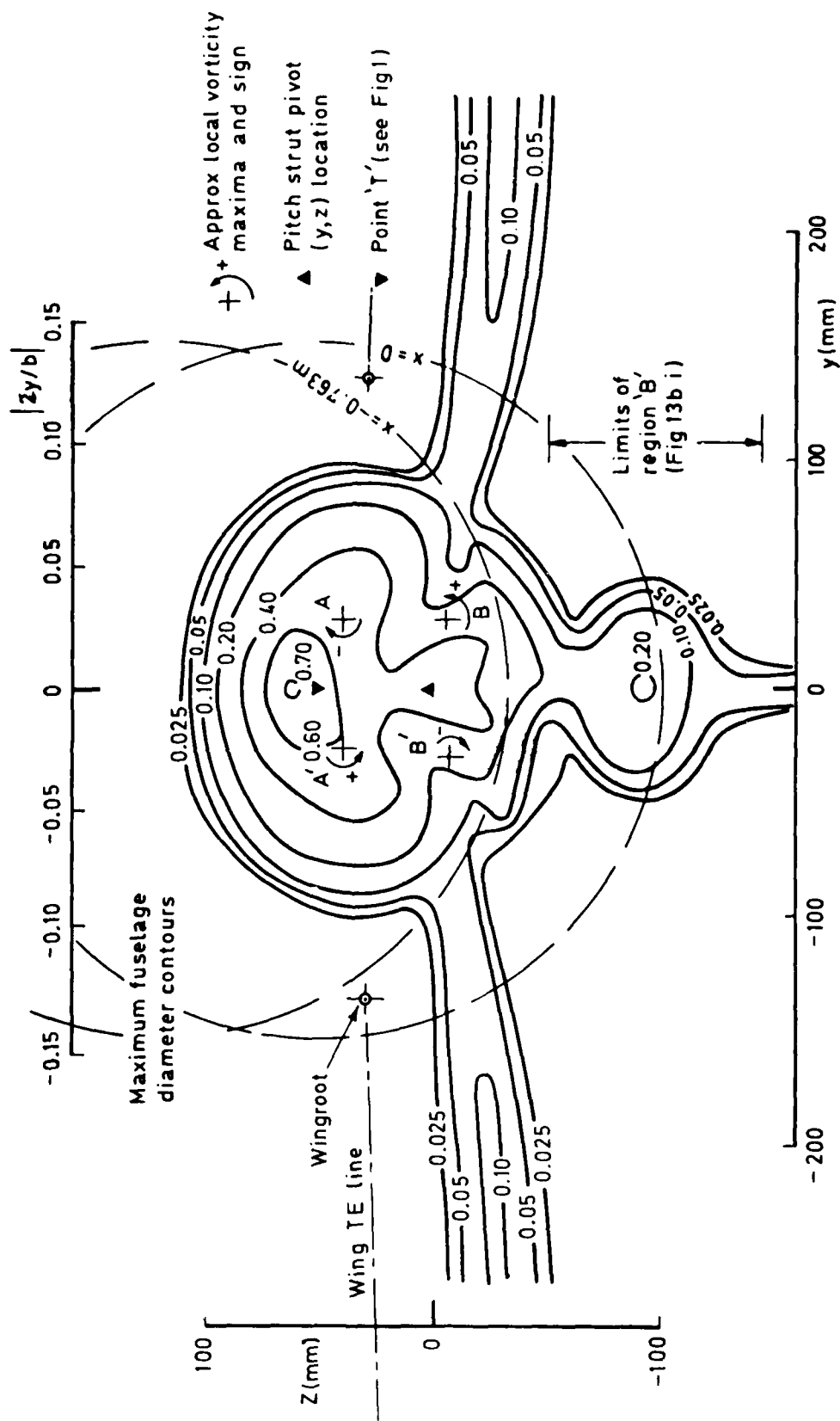
Fig 15a Centre section - contours of constant $(H_0 - H)/q_0$

Fig 15b

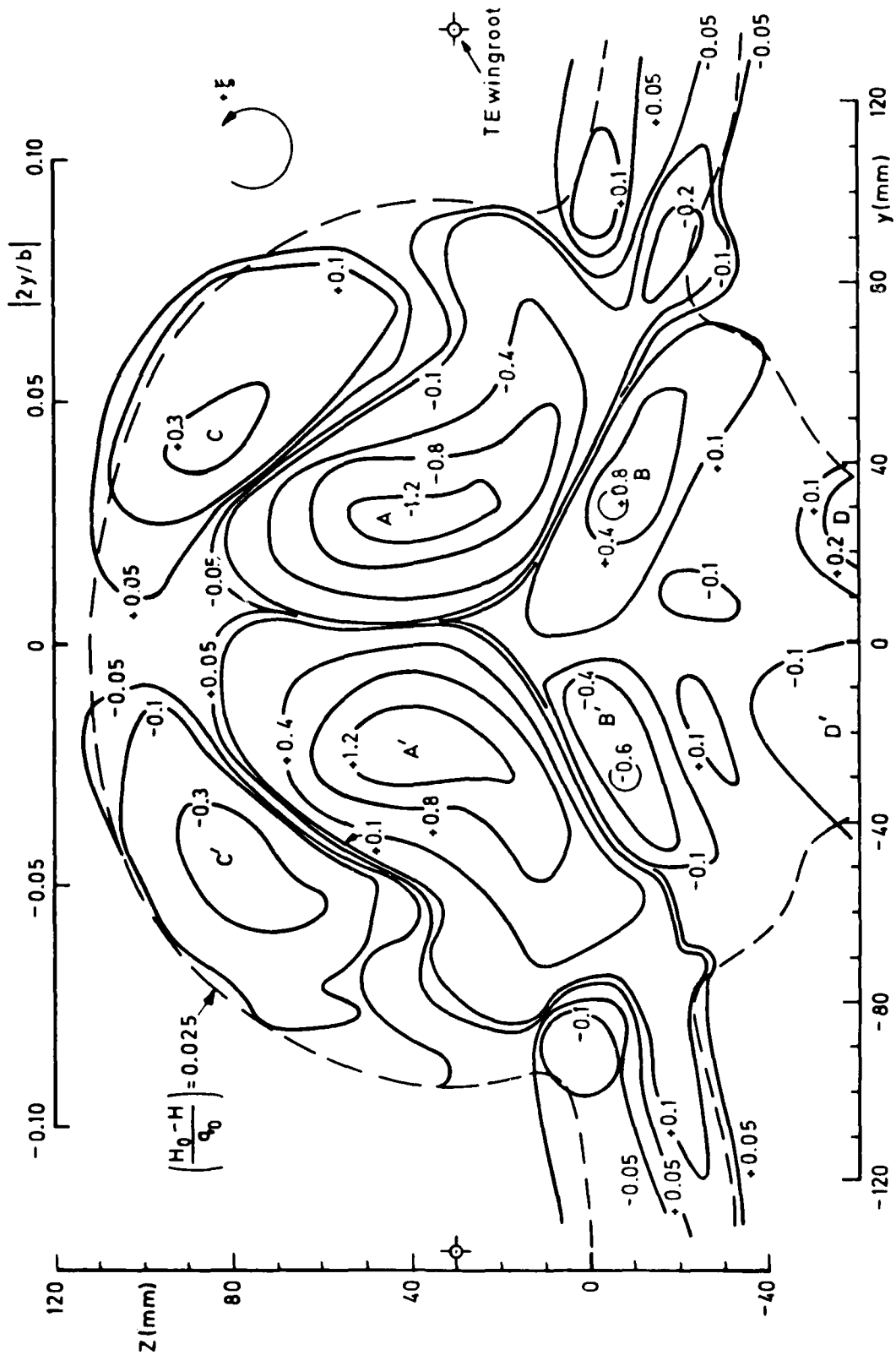


Fig 15b Centre section - contours of constant ξ_c/U_0

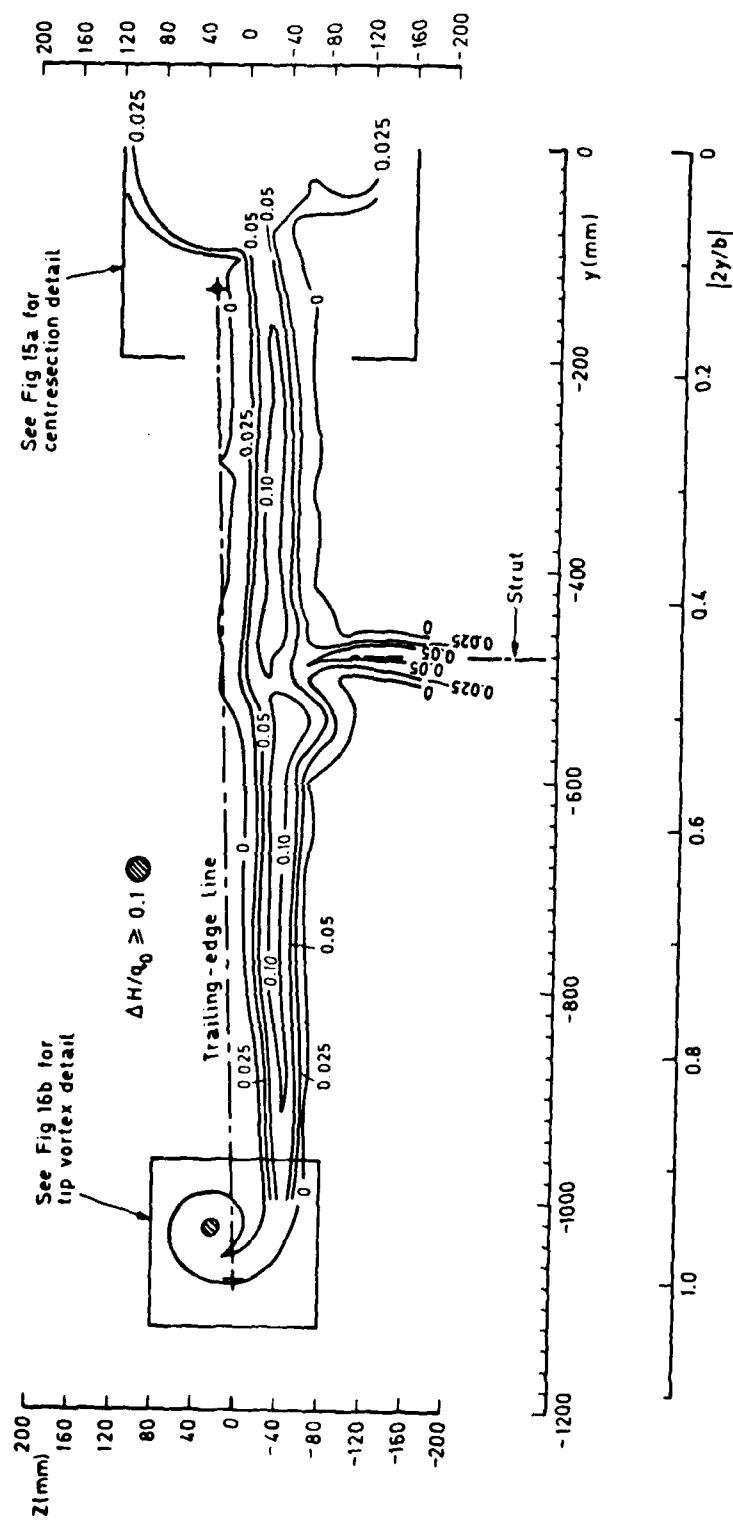
Fig 16a Contours of constant total head defect $(H_0 - H)/q_0$ — port wing wake

Fig 16b

$$\frac{H_0 - H}{\rho_0} \geq 1.0$$

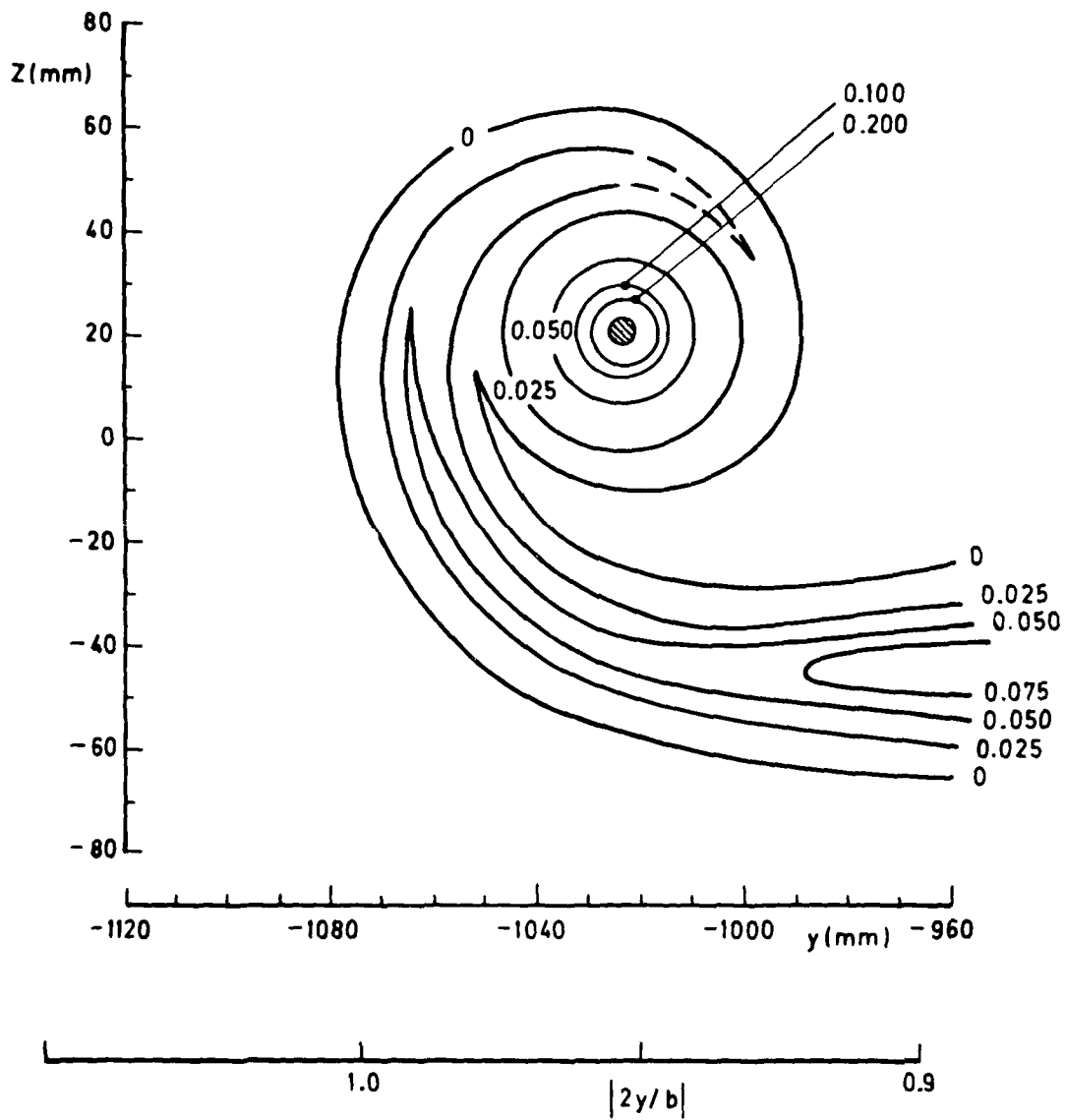


Fig 16b Contours of constant total head defect — port tip vortex region

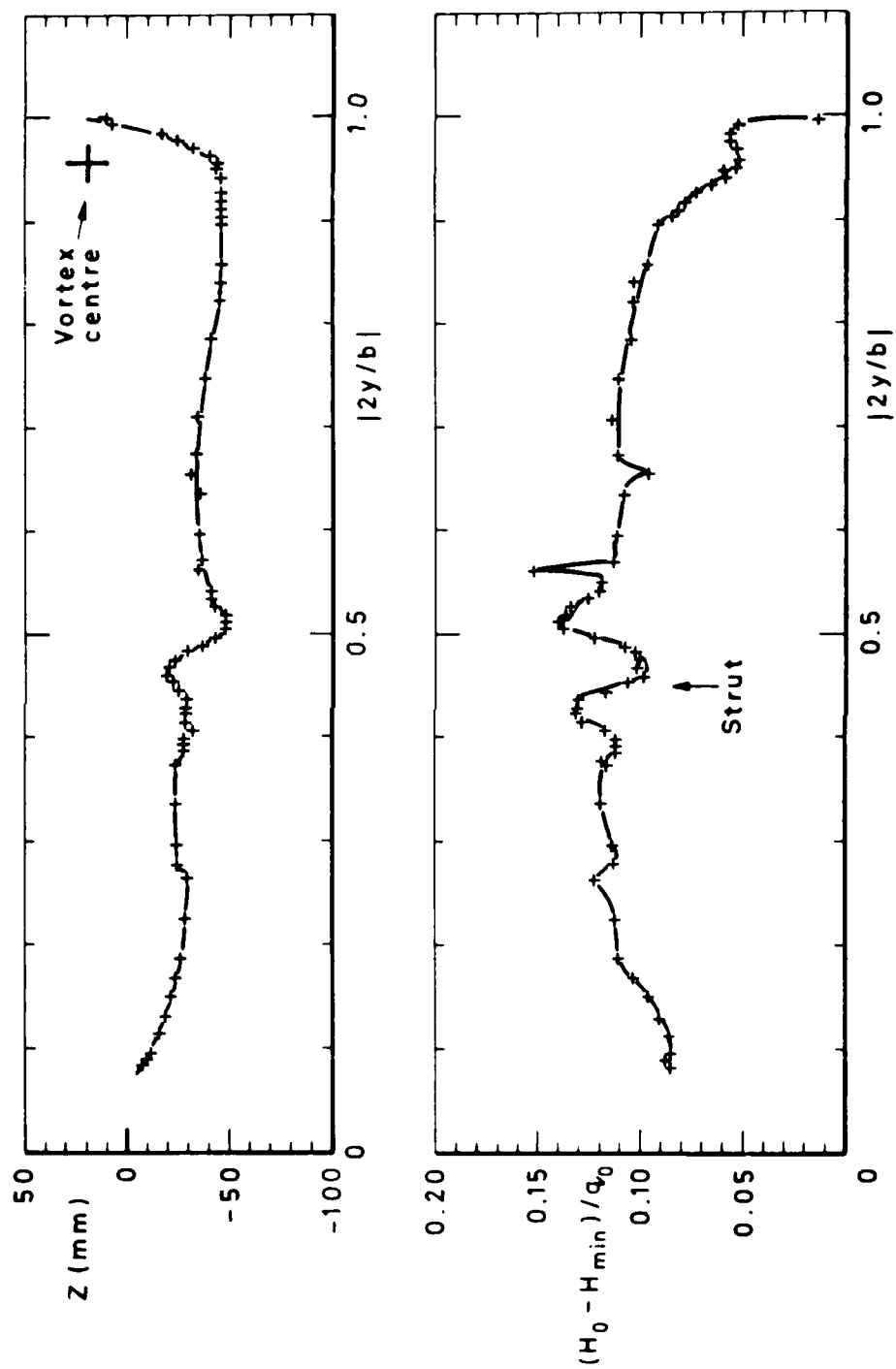


Fig 17 Locus of maximum total head defect and its value — port viscous wake

Fig 18

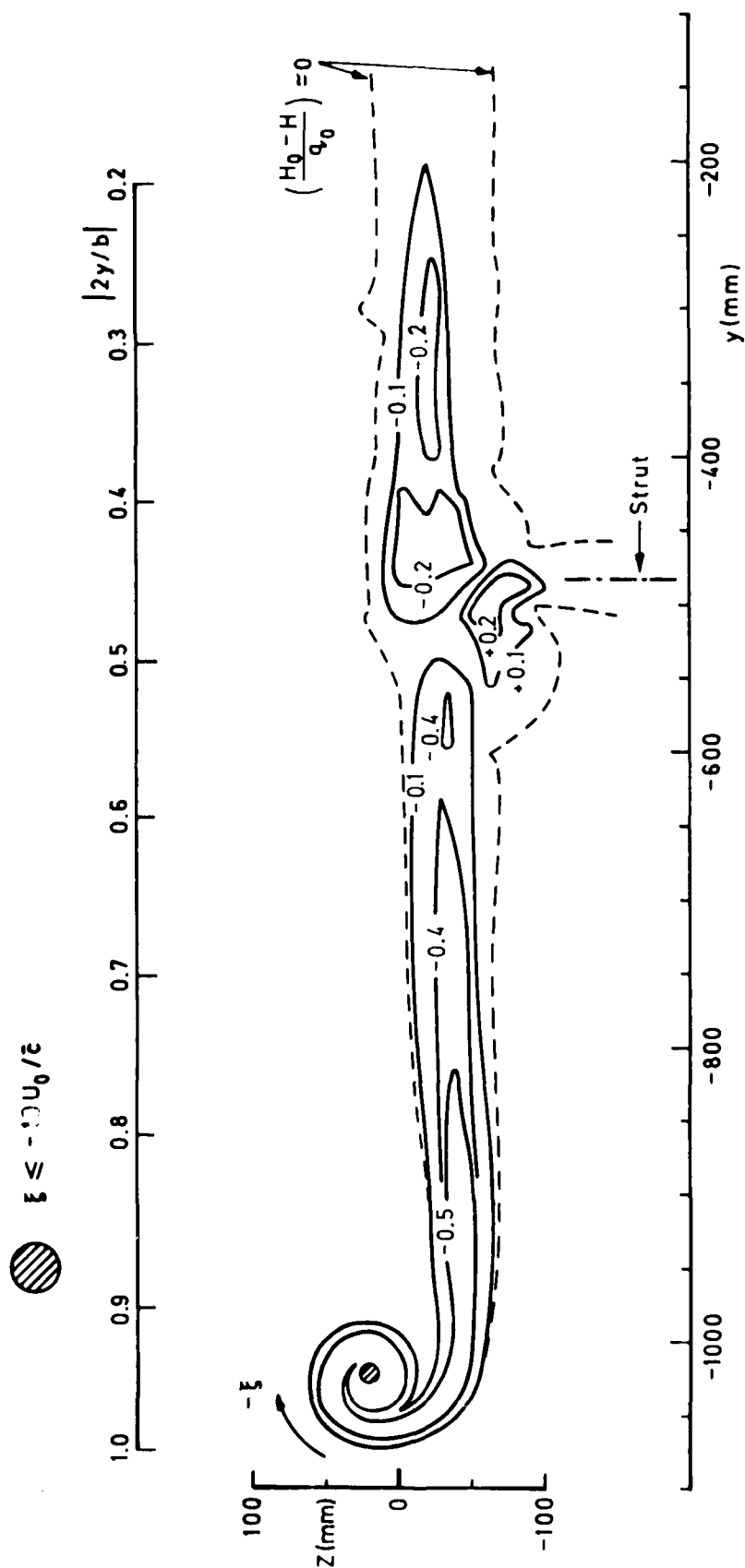


Fig 18 Contours of constant streamwise vorticity (ξ_c/U_0) - port wing

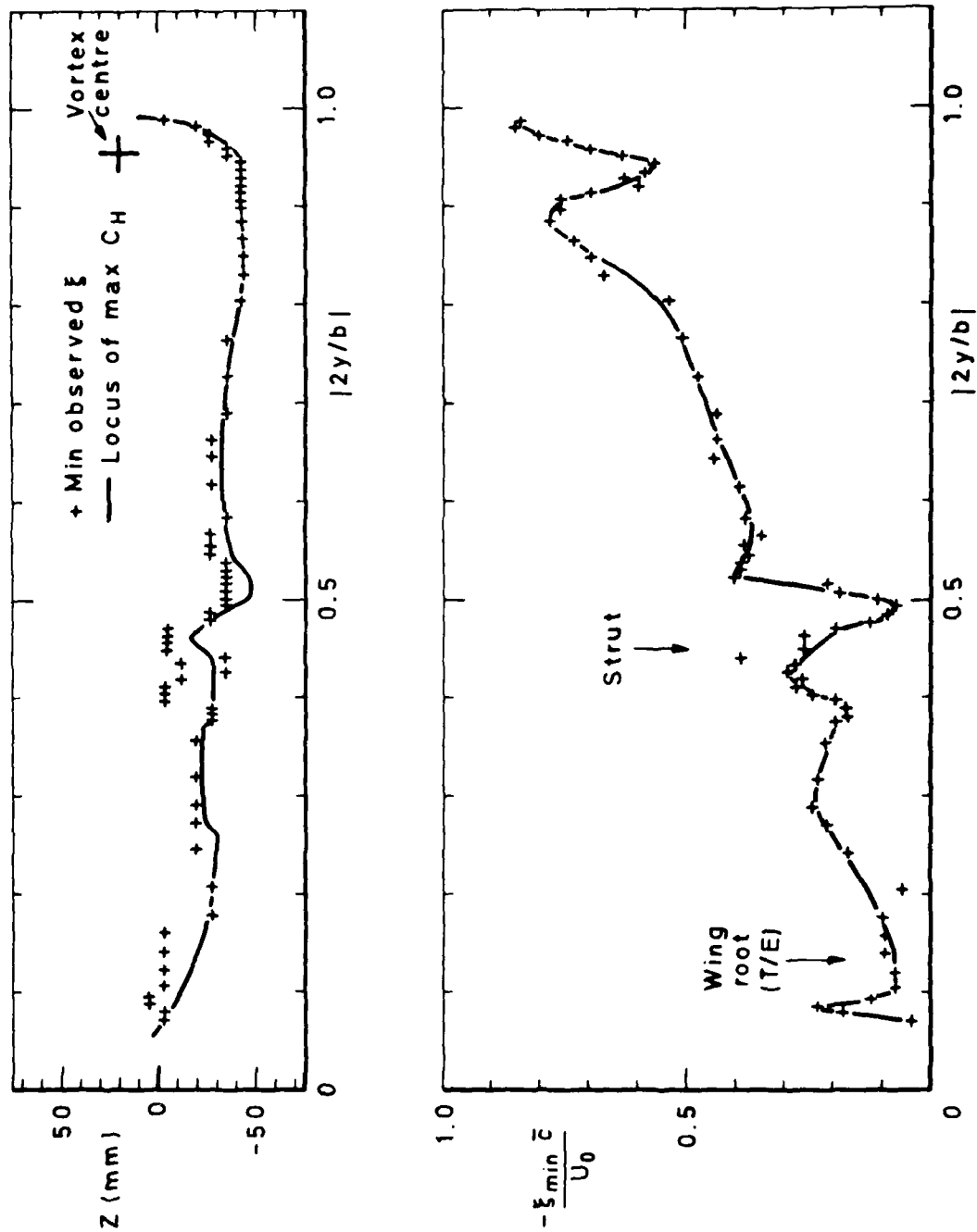


Fig 19 Locus of maximum (negative) observed vorticity and its value — port viscous wake

Fig 20

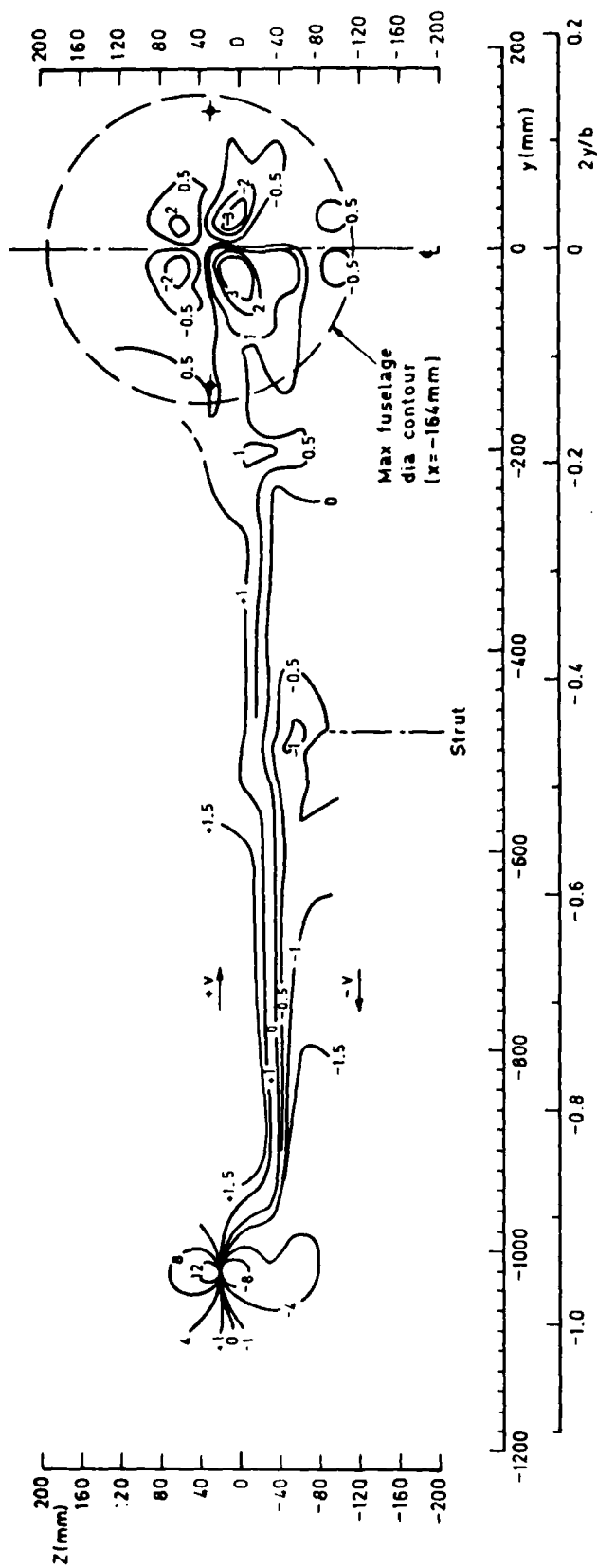


Fig 20 Contours of constant sidewash angle (v°) – port wing

TR 81012

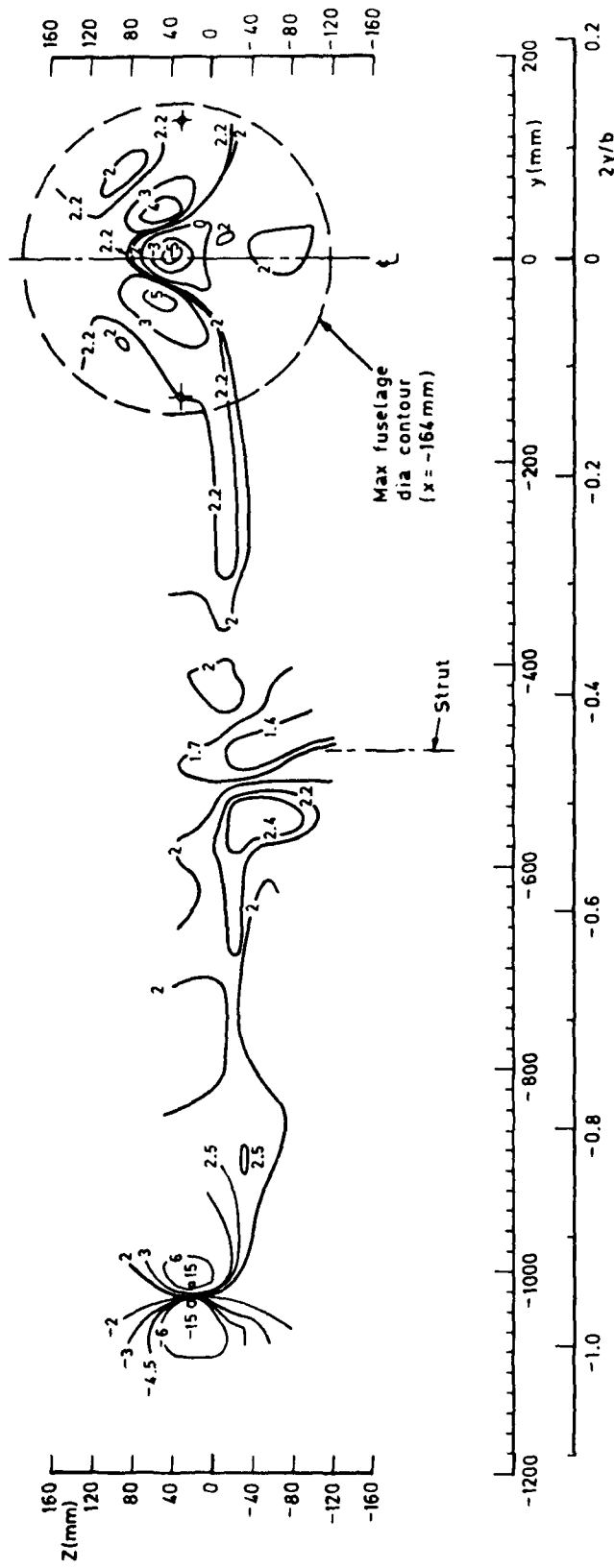
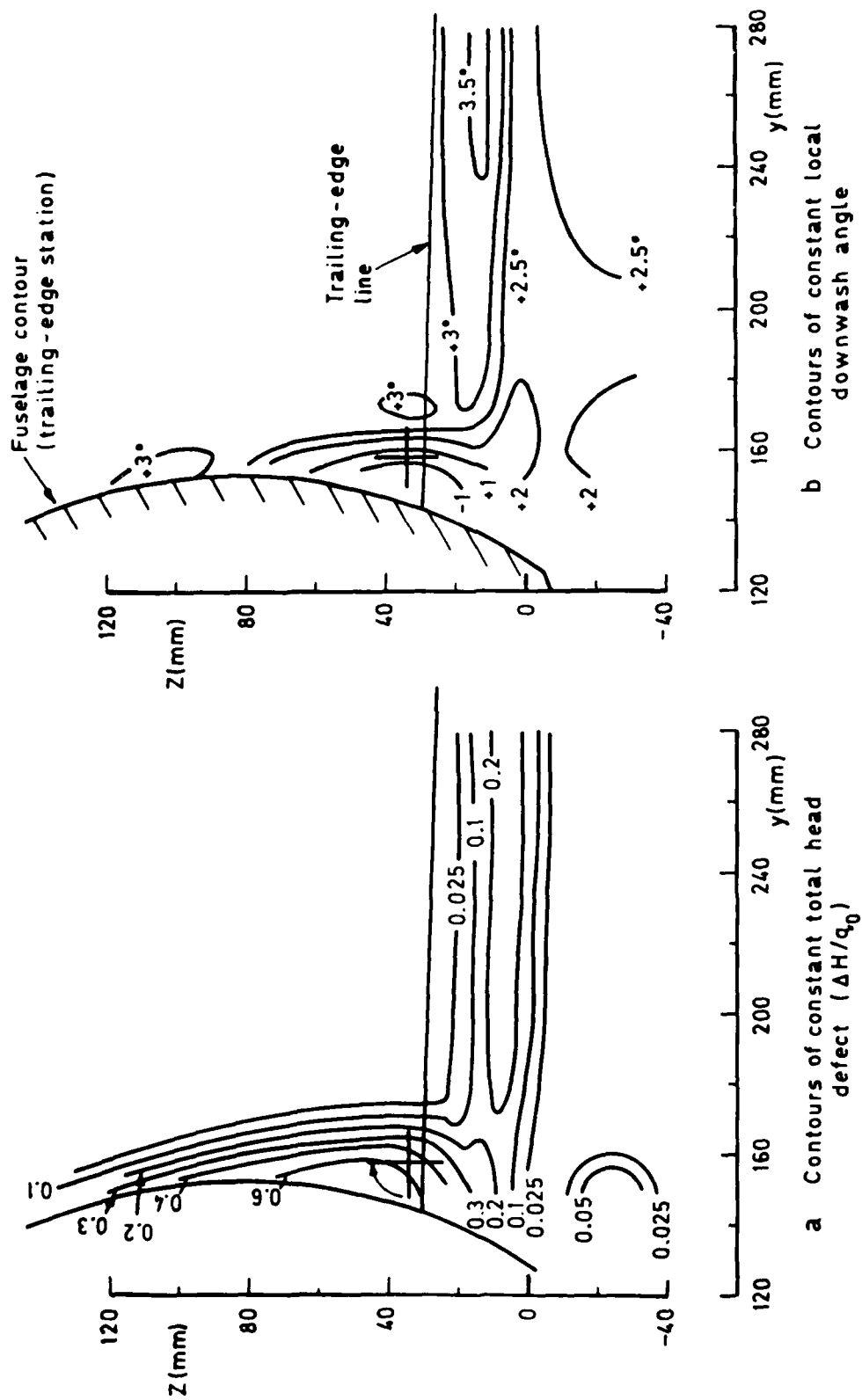


Fig 21 Contours of constant downwash angle (w°) - port wing

Fig 22a&b



+ Possible location of vortex 'A' (Figs 15a, 15b)

Fig 22a&b Measurements in fuselage side plane 'A'

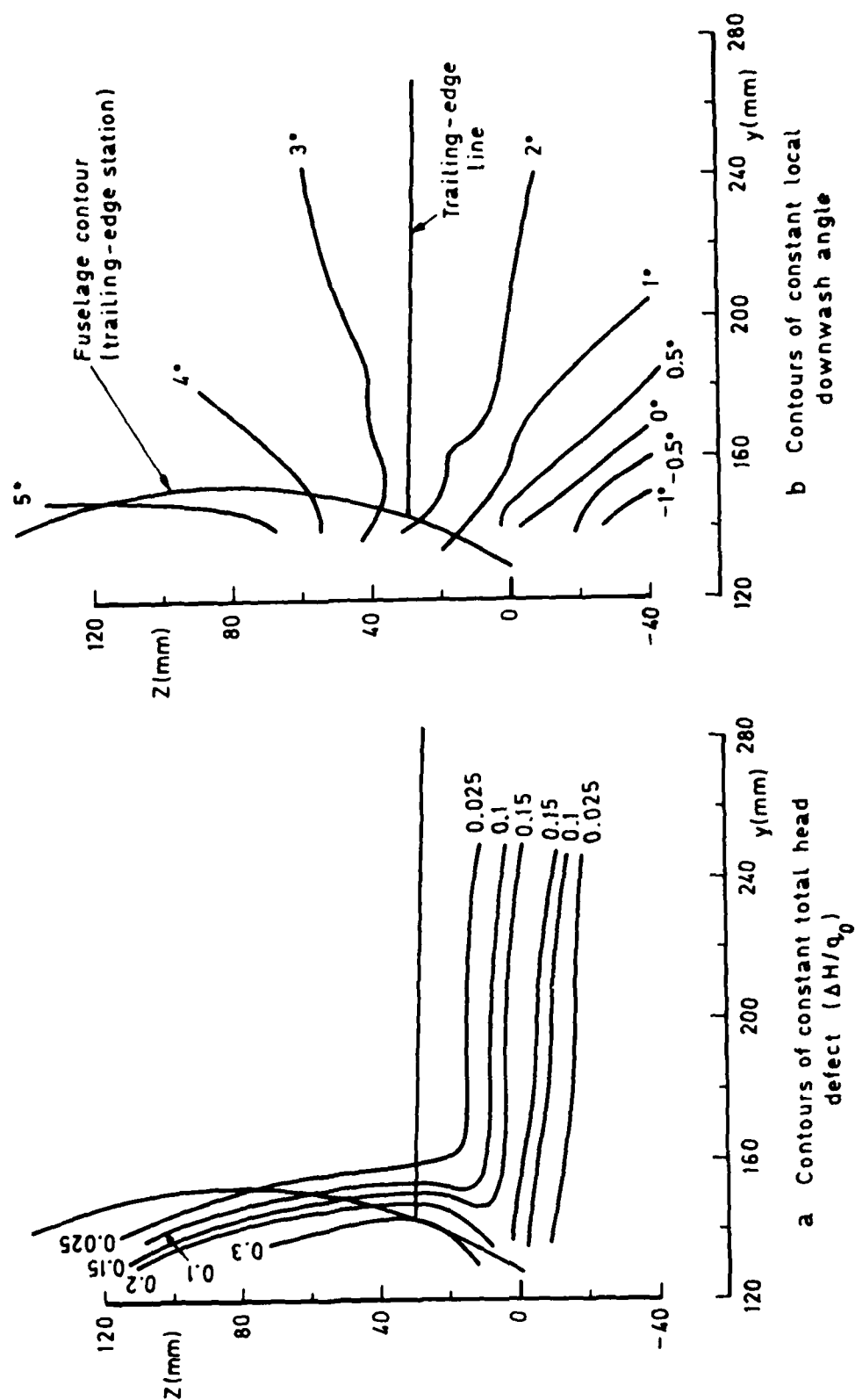


Fig 23a&b Measurements in fuselage side plane 'B'

Fig 24a&b

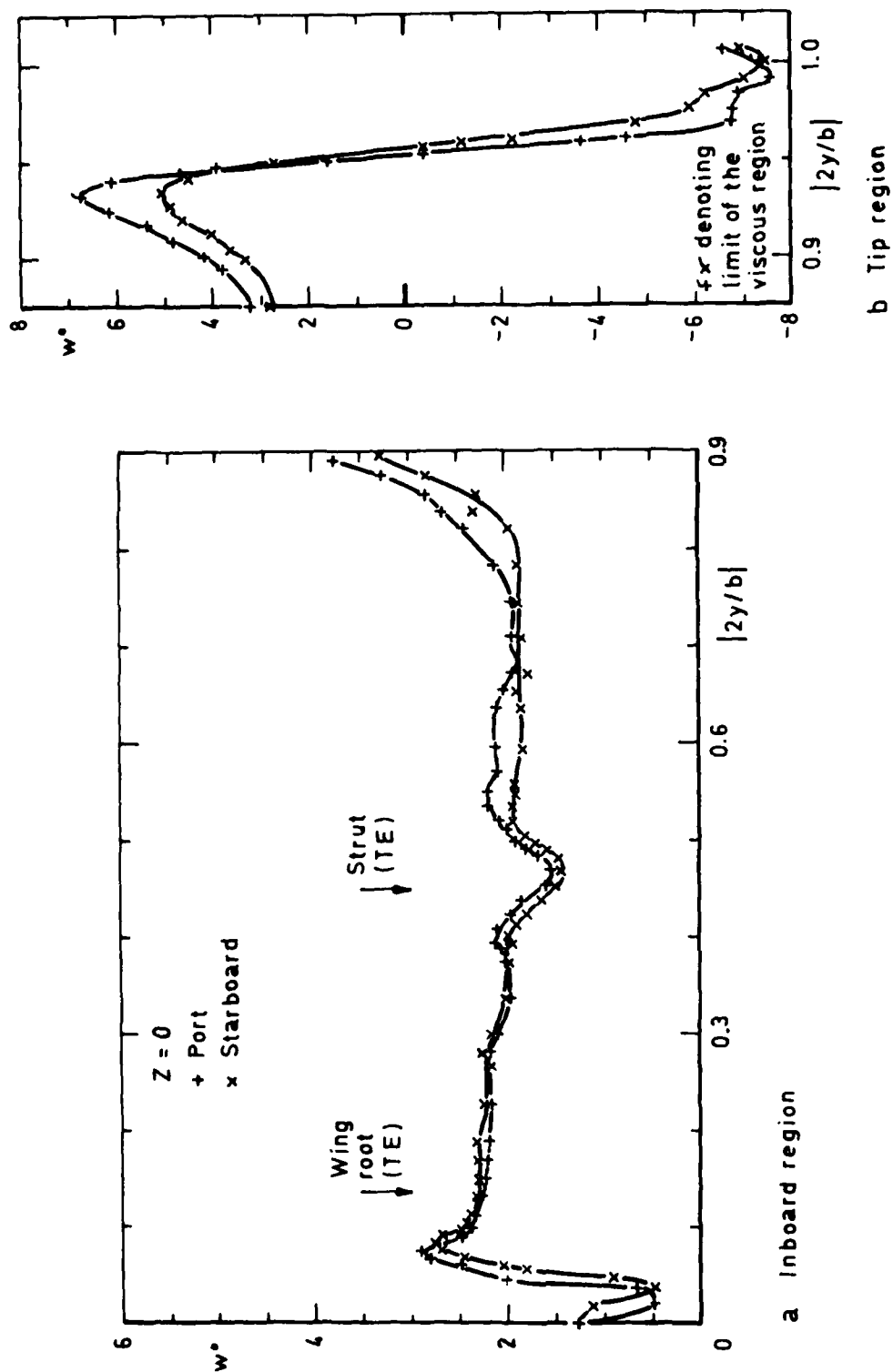


Fig 24a&b Spanwise distribution of downwash angle, in plane of tip-to-tip line

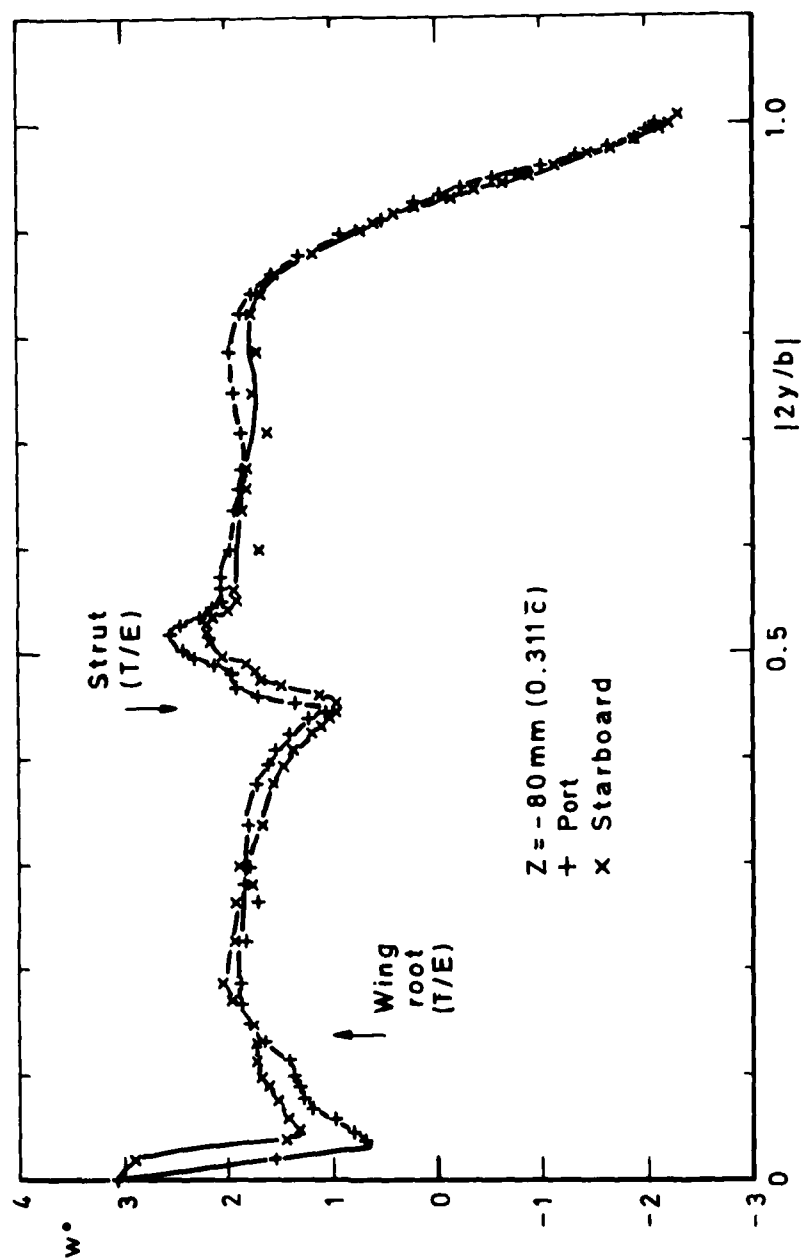


Fig 25 Spanwise distribution of downwash angle, below the viscous wake of the wing

Fig 26a&b

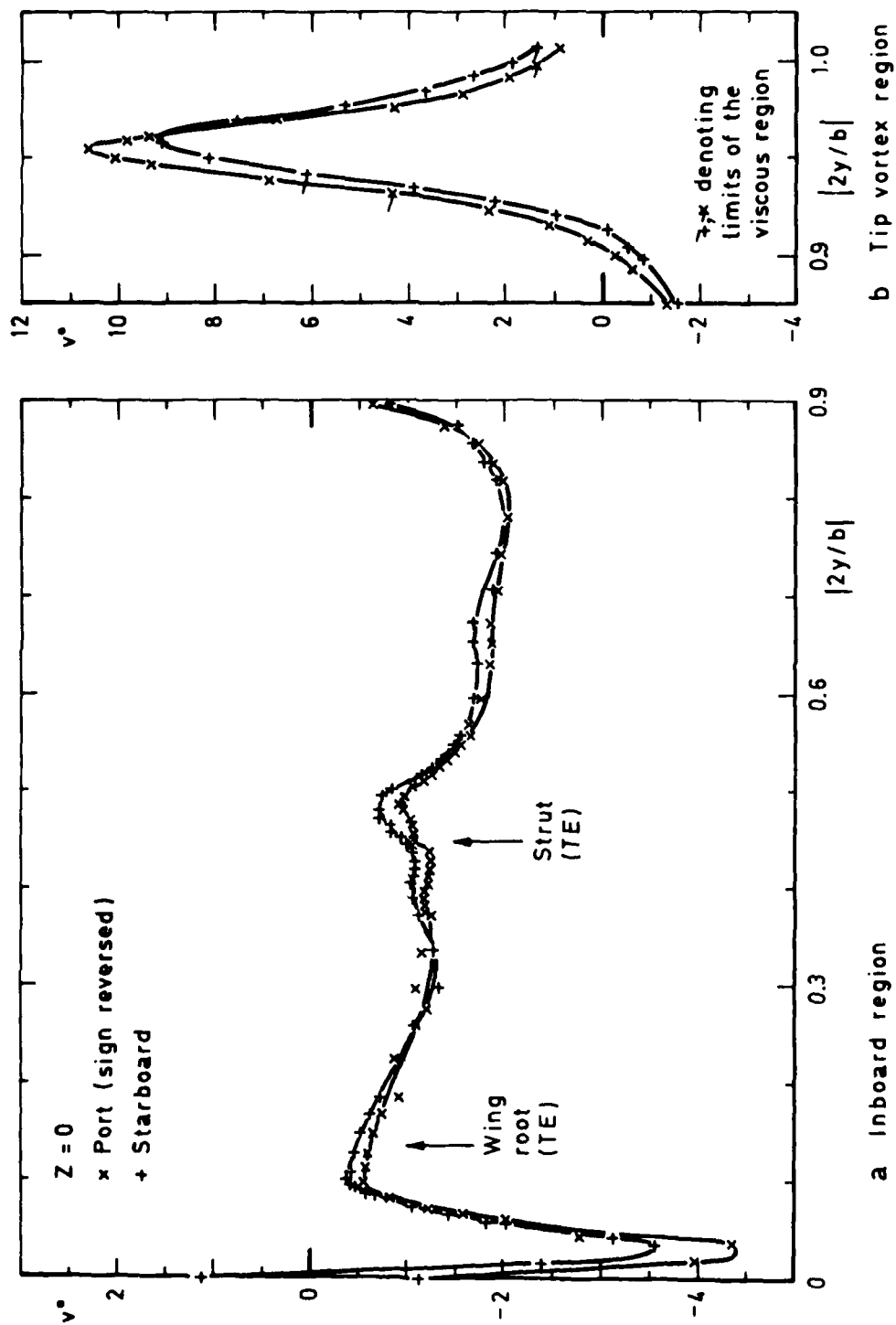


Fig 26a&b Spanwise distribution of sidewash angle, in plane of tip-to-tip line

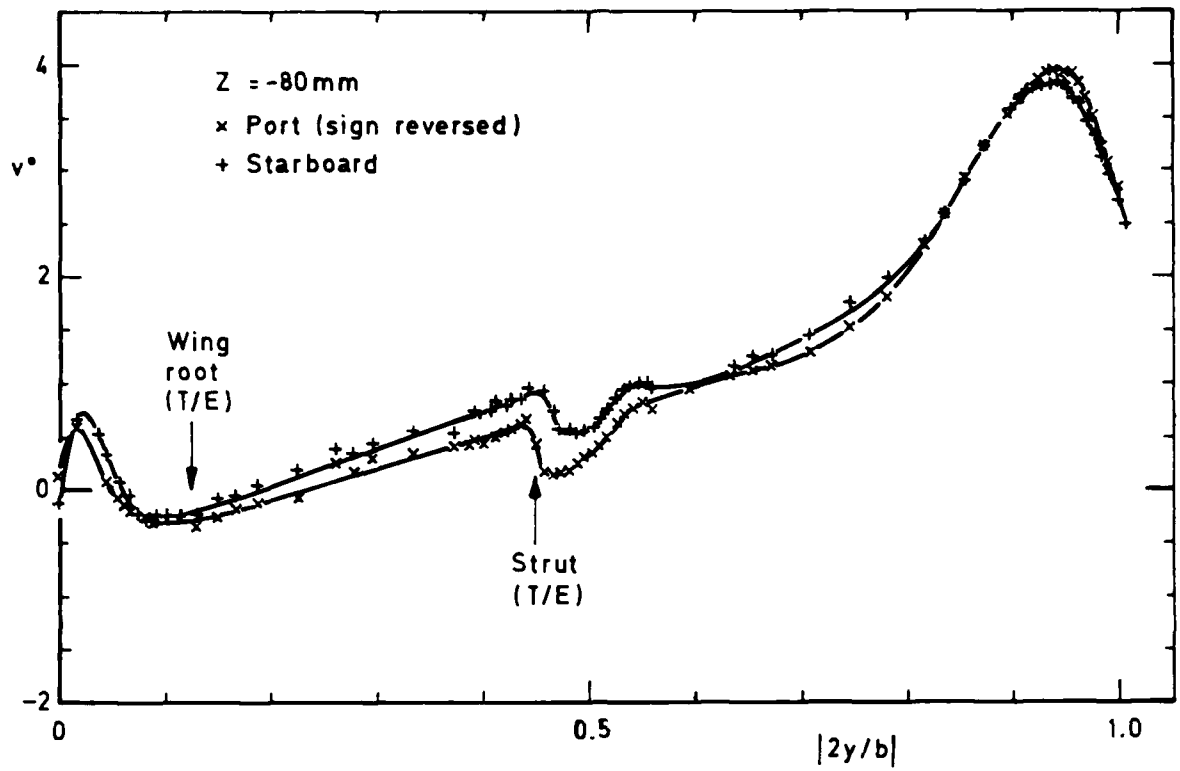


Fig 27 Spanwise distribution of sidewash angle, below the viscous wake of the wing

Fig 28a

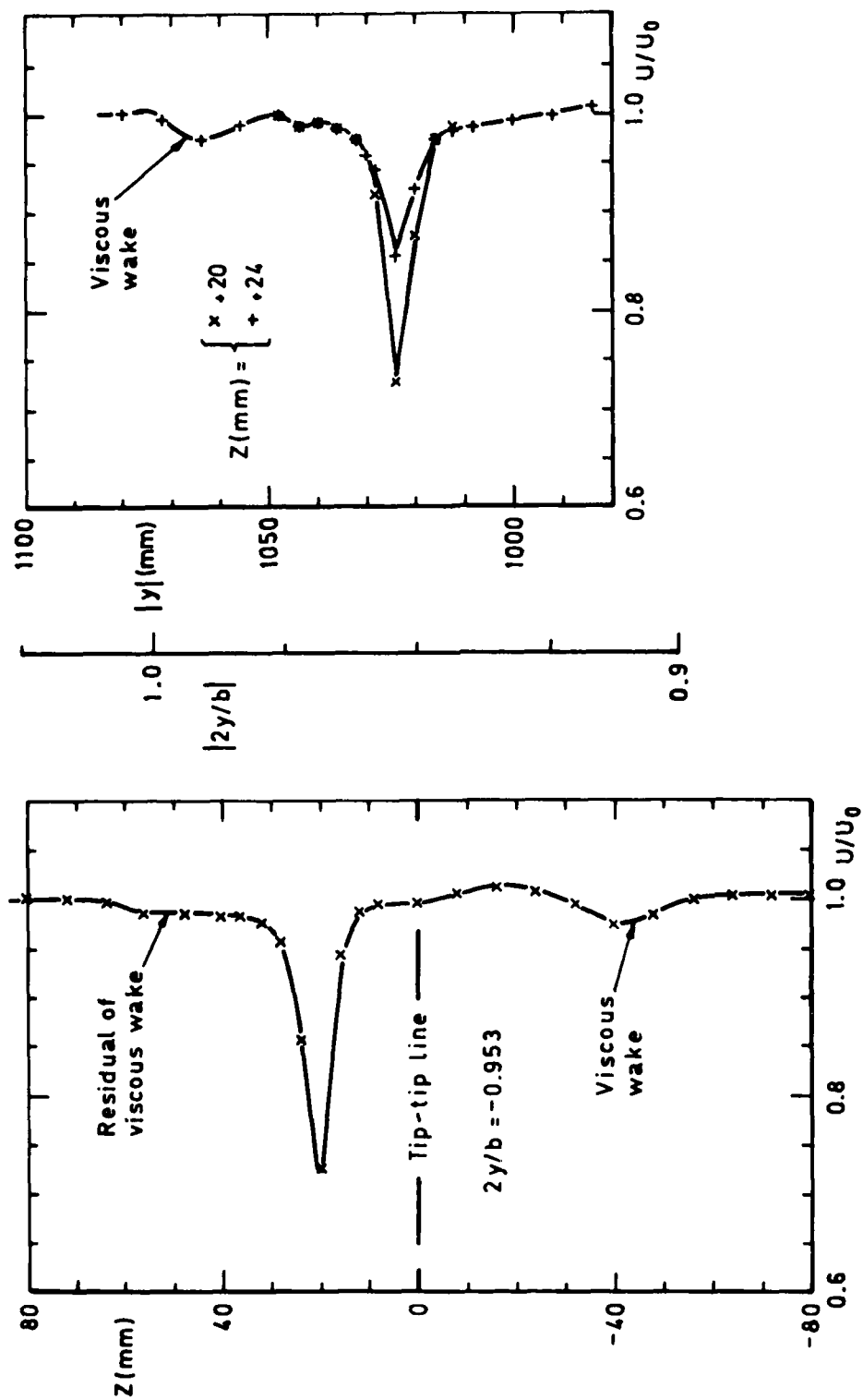


Fig 28a Variation of streamwise velocity on a vertical cut and a horizontal cut through the port tip vortex core

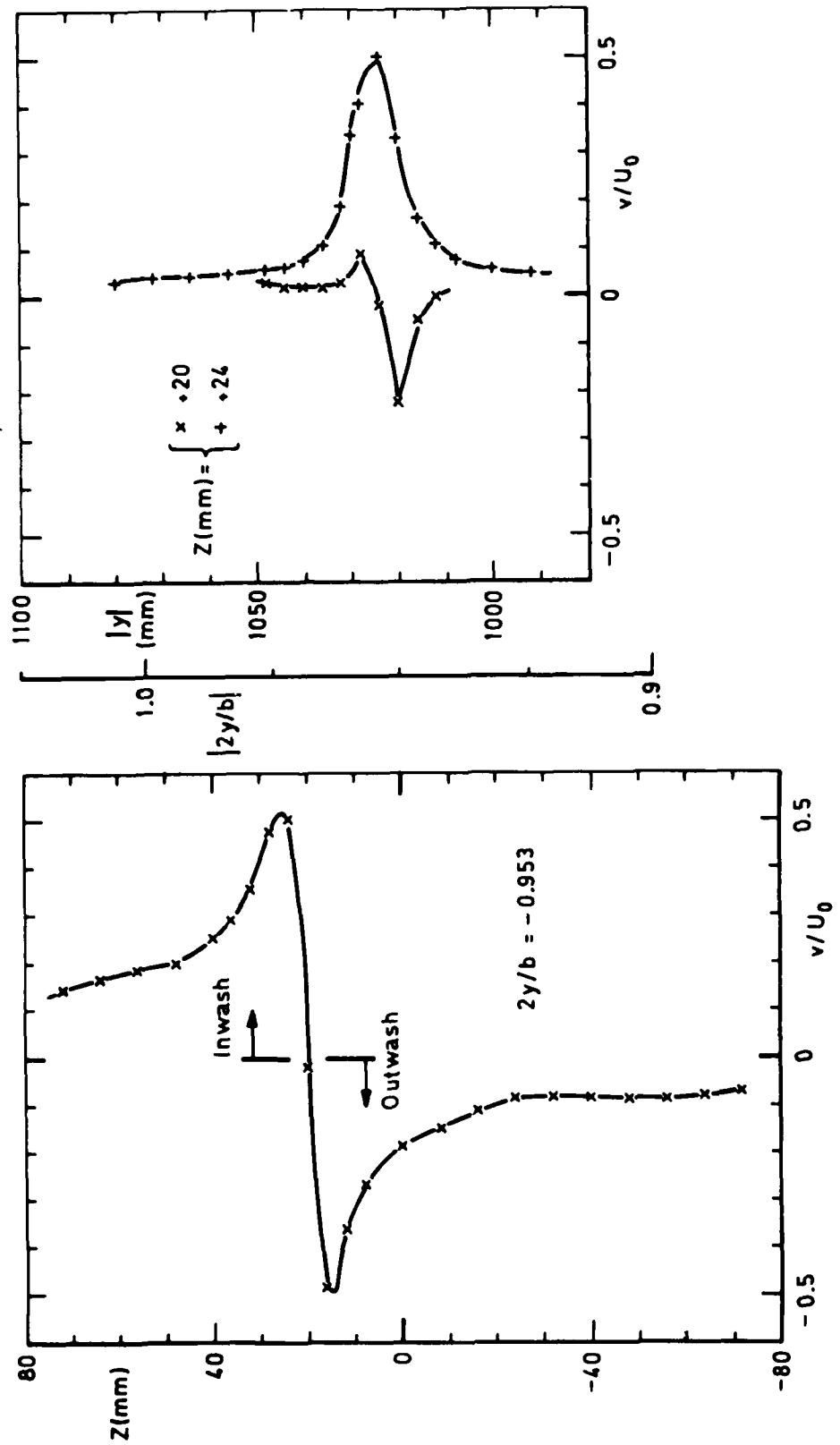


Fig 28b Variation of sidewash velocity on a vertical and horizontal cut through the port tip vortex core

Fig 28c

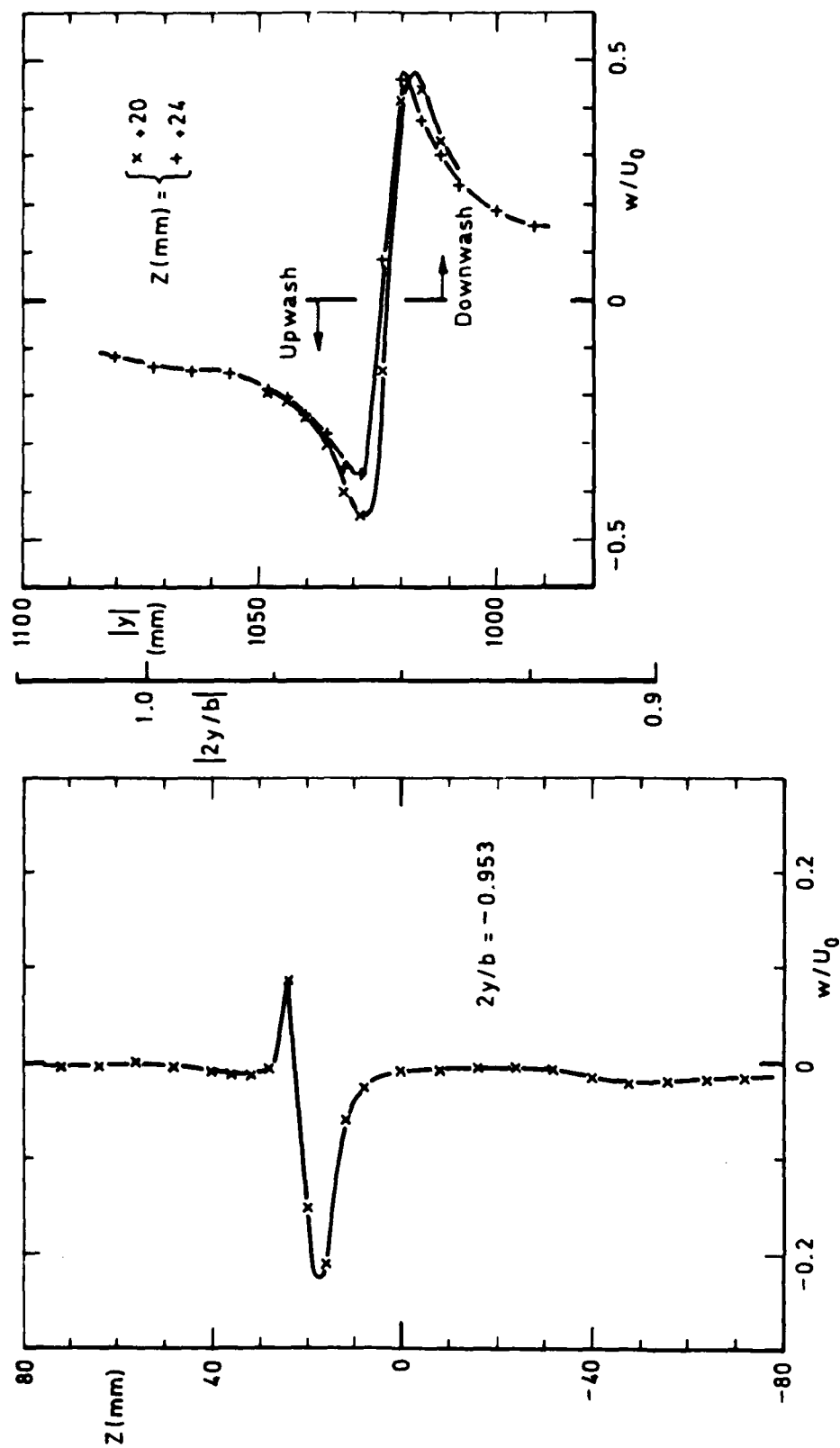


Fig 28c Variation of downwash velocity on a vertical and horizontal cut through the port vortex core

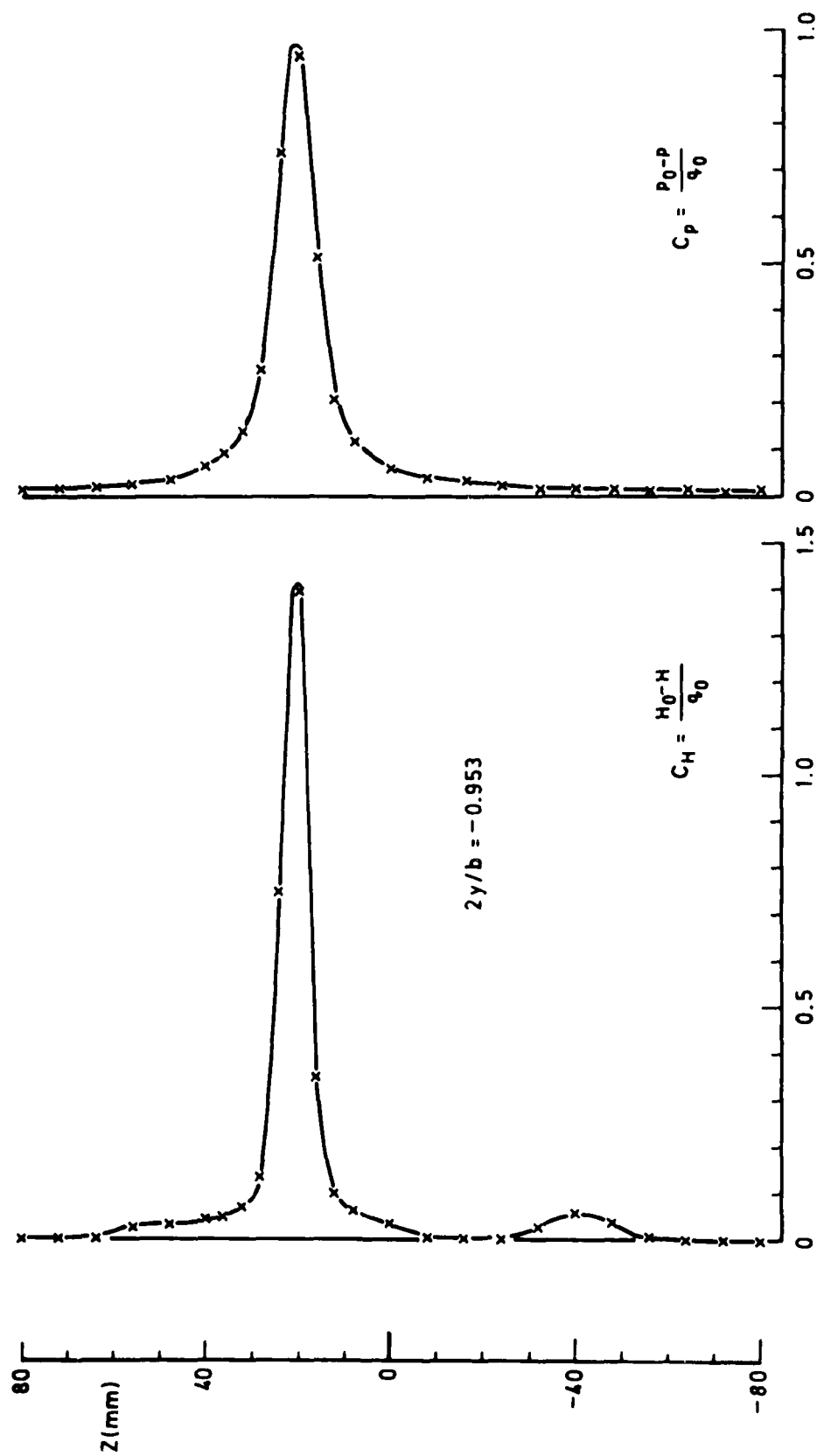
Fig 28d Variation of C_H and C_P on a vertical cut through the port tip vortex core

Fig 28e

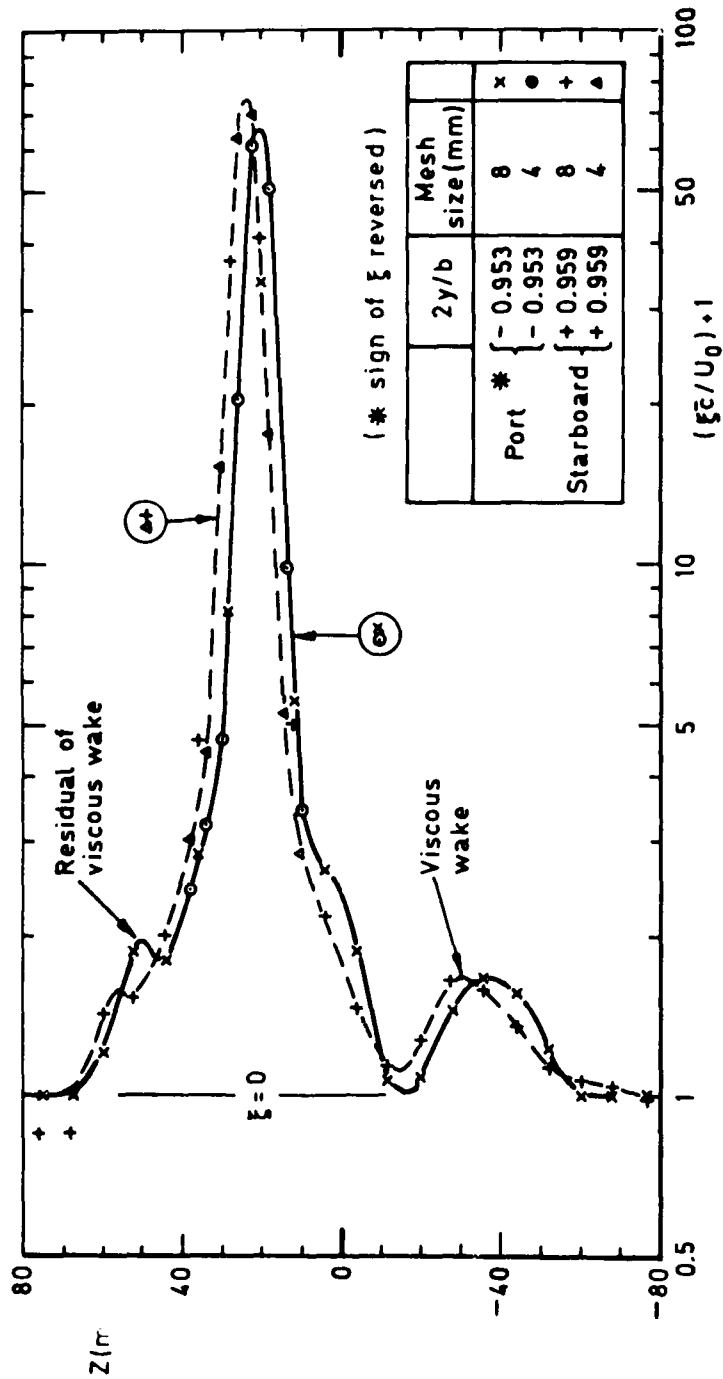


Fig 28e Variation of streamwise vorticity (ξ) on vertical cuts through the vortex cores

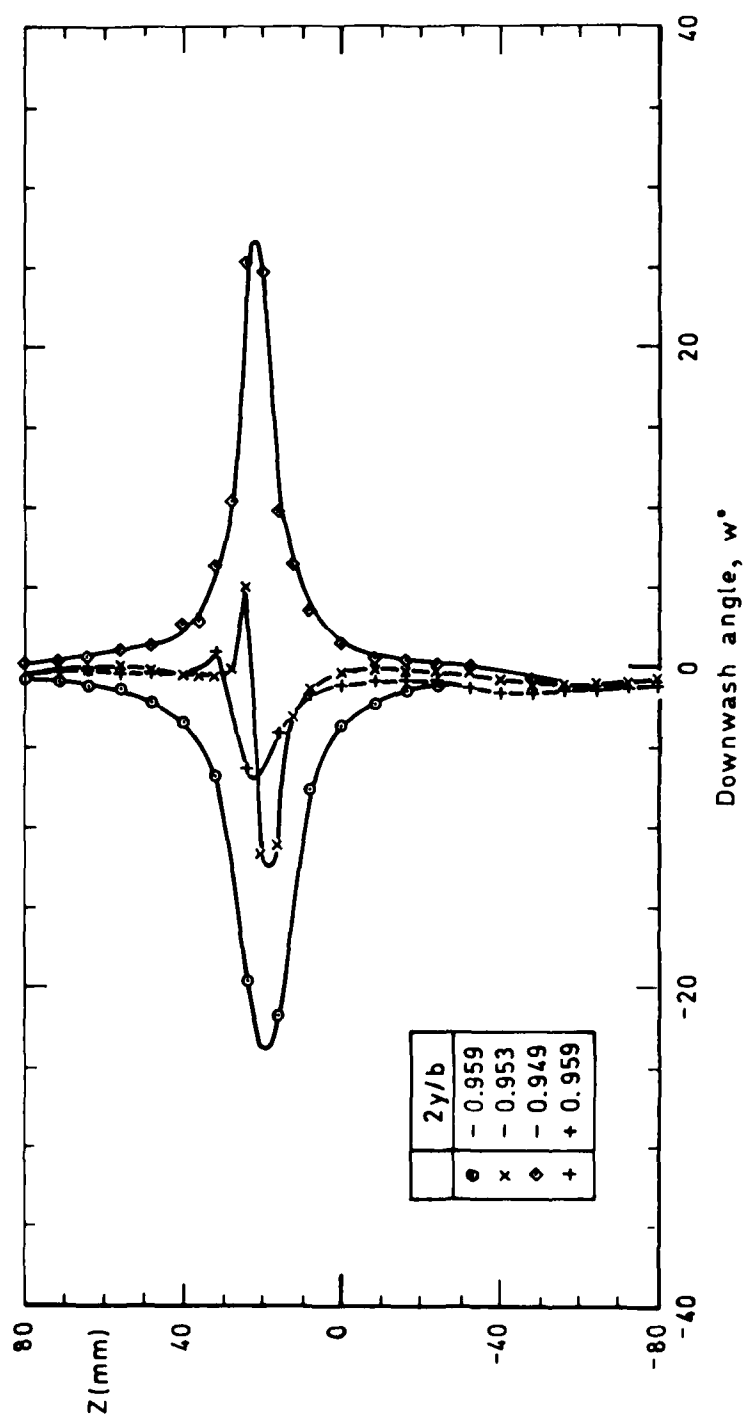


Fig 29 Variation of downwash angle on vertical cuts through the tip vortex cores

Fig 30

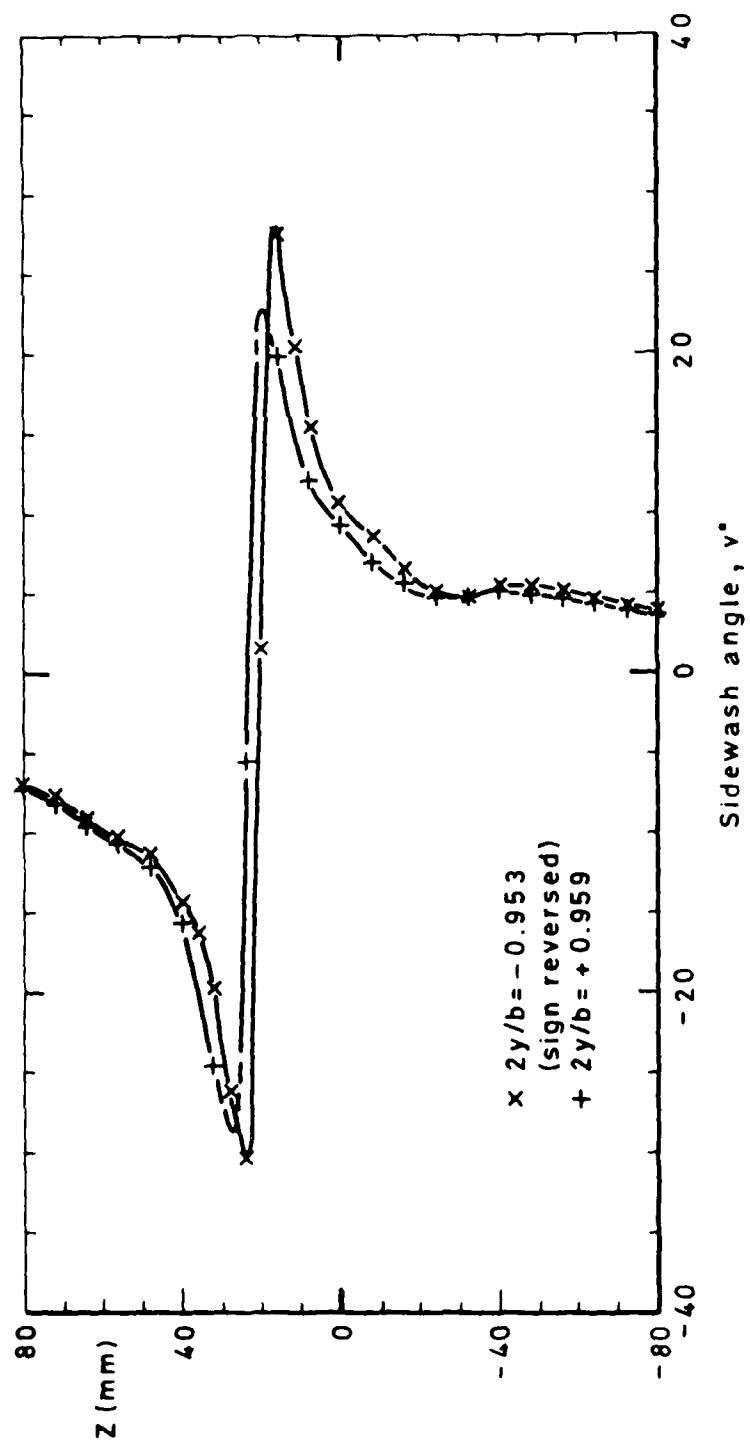


Fig 30 Variation of sidewash angle on vertical cuts through the tip vortex cores

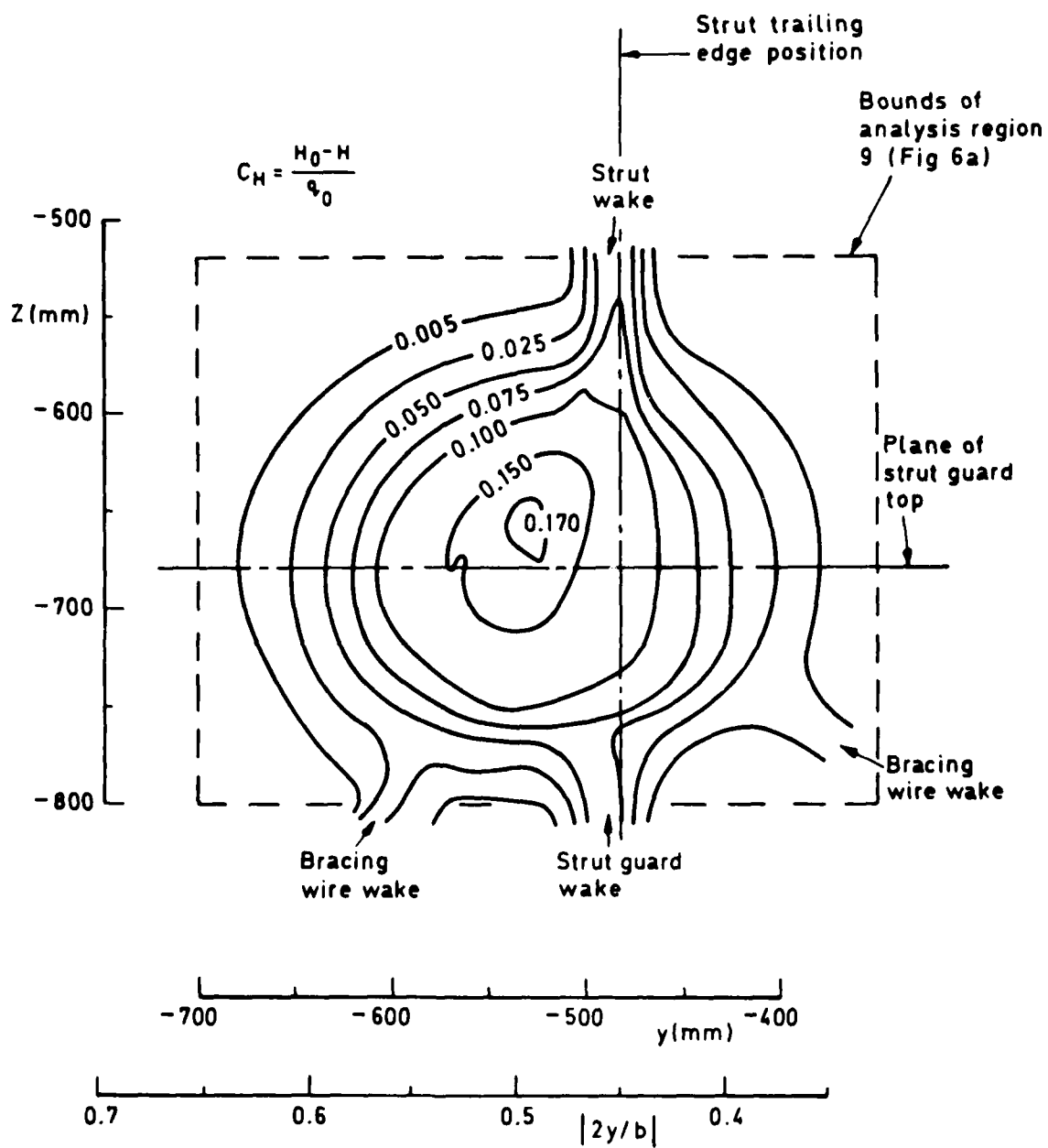


Fig 31 Contours of constant total head defect in the port strut guard leakage plume

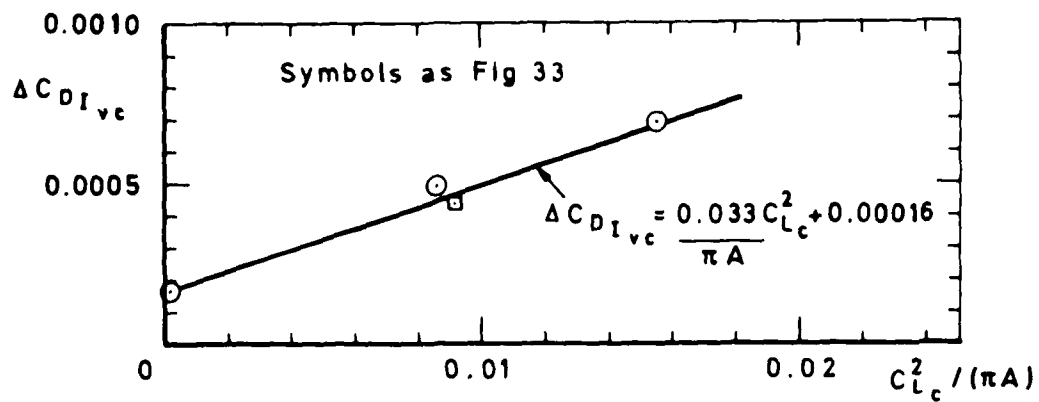


Fig 32 Variation of 'profile drag' contribution measured in the vortex cores with lift

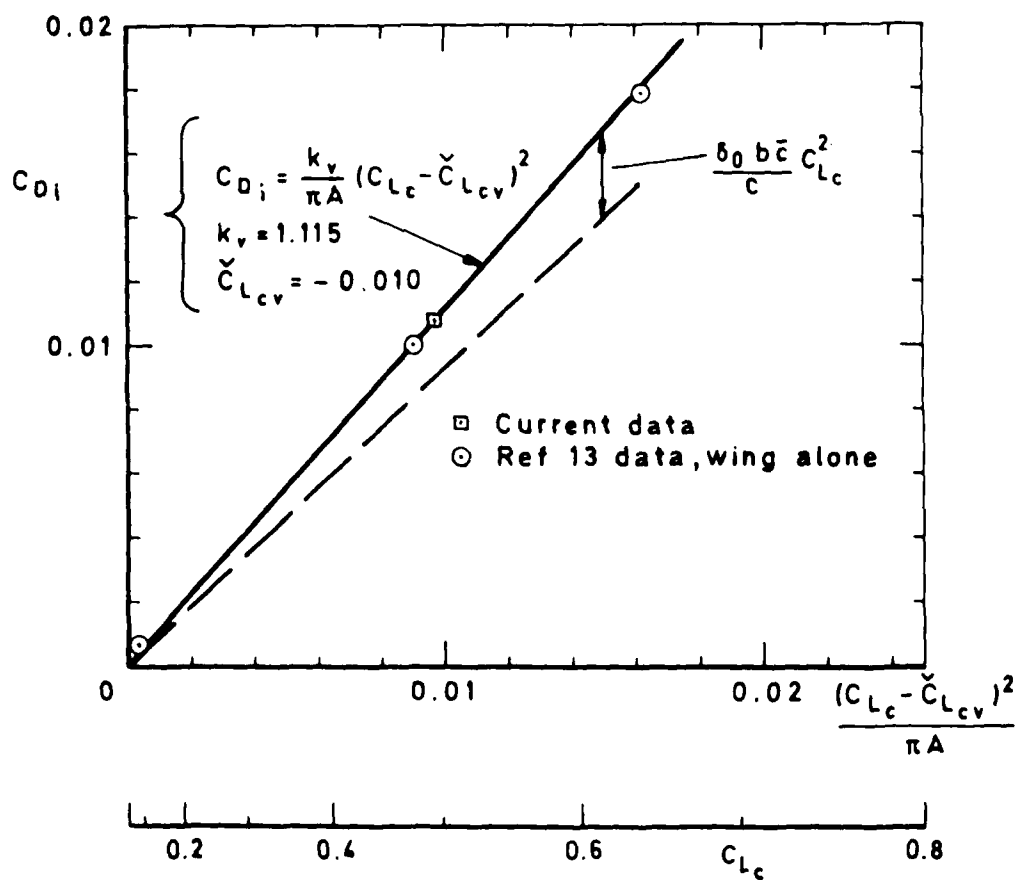


Fig 33 Variation of induced drag (corrected for constraint and strut interference) with lift

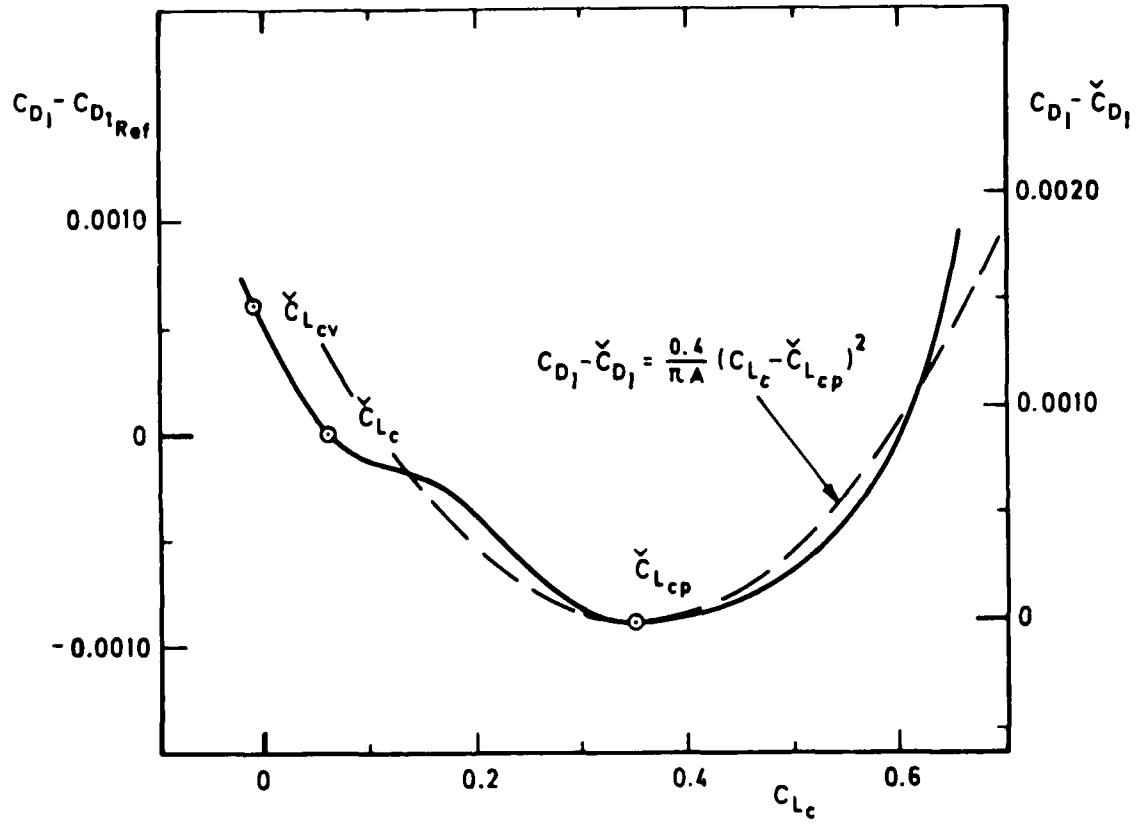


Fig 34 Estimated variation of profile drag (relative to a minimum total drag datum) with lift

Fig 35

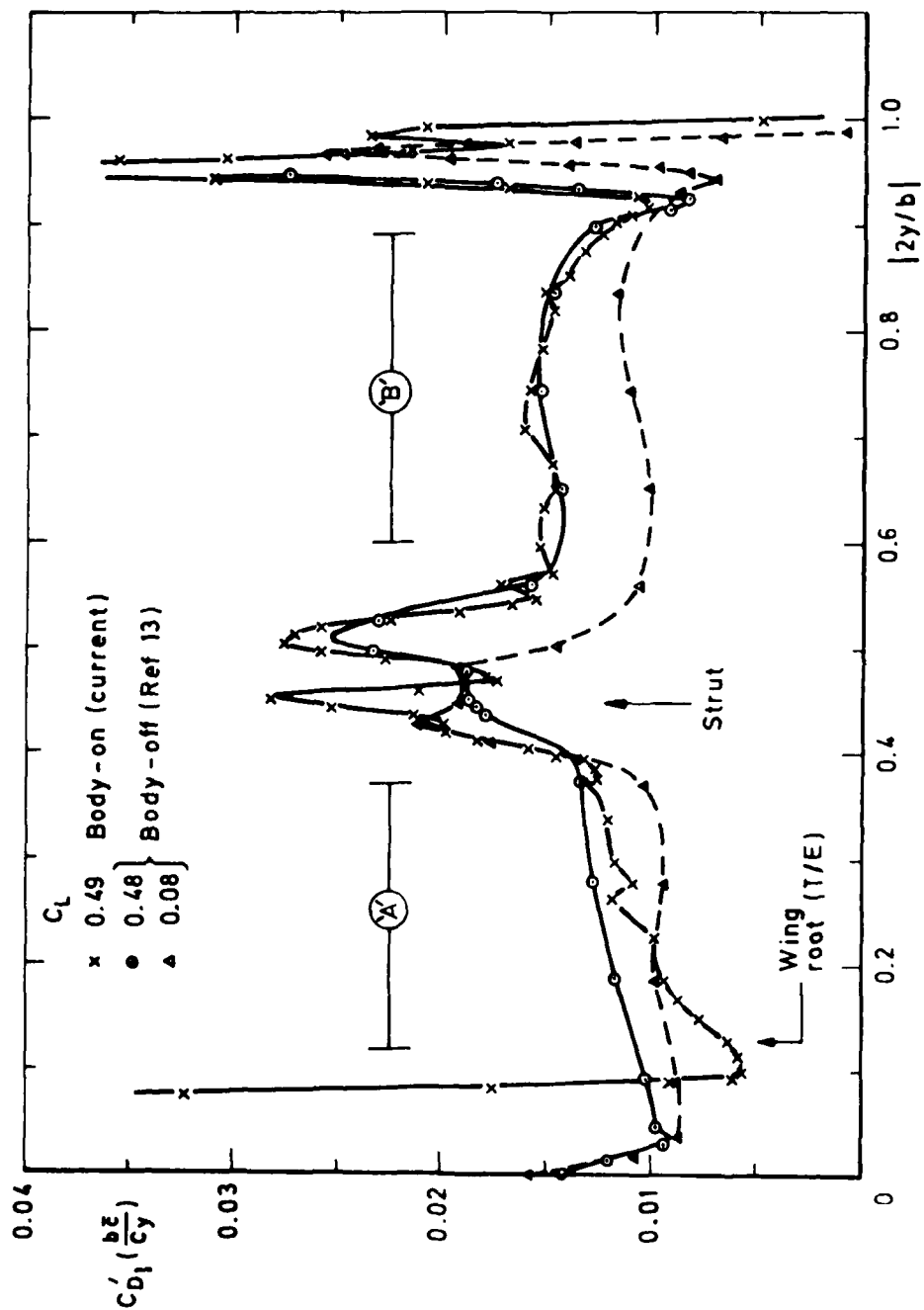


Fig 35 Spanwise distribution of profile drag, scaled on local chord (C_y)

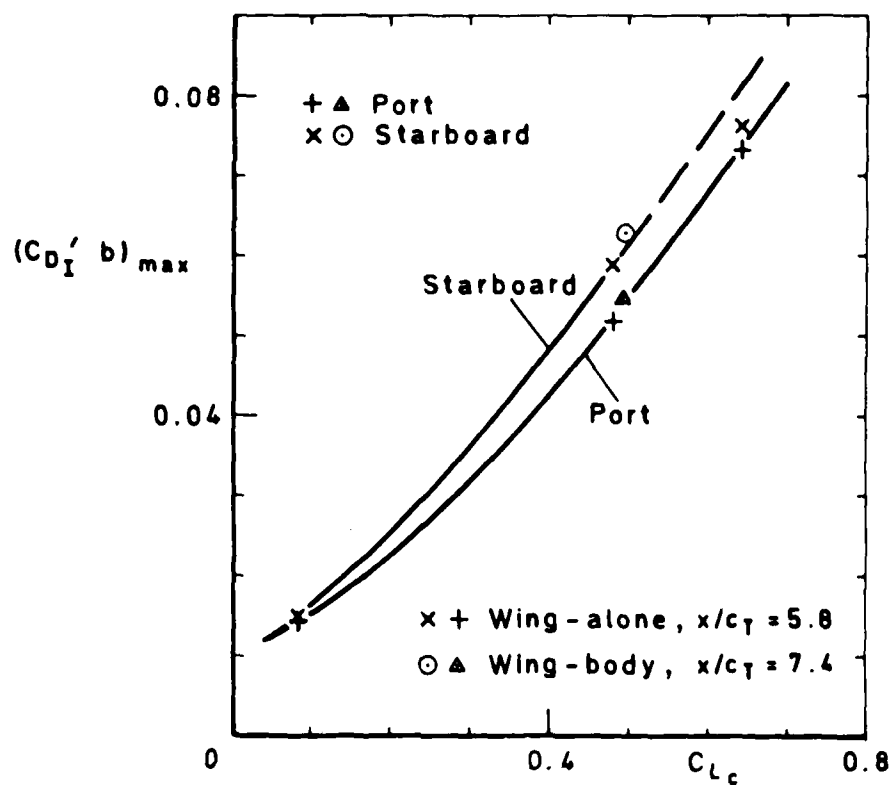


Fig 36 Variation of the maximum local profile drag contribution (at $|y/b_v| = 1.0$) with lift

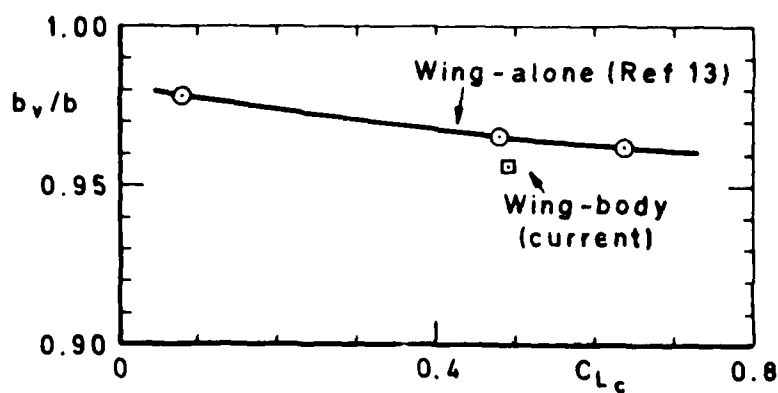


Fig 37 Variation of the tip vortex core separation (b_v) with lift

REPORT DOCUMENTATION PAGE

Overall security classification of this page

UNLIMITED

As far as possible this page should contain only unclassified information. If it is necessary to enter classified information, the box above must be marked to indicate the classification, e.g. Restricted, Confidential or Secret.

1. DRIC Reference (to be added by DRIC)	2. Originator's Reference RAE TR 81012	3. Agency Reference N/A	4. Report Security Classification/Marking UNLIMITED		
5. DRIC Code for Originator 7673000W		6. Originator (Corporate Author) Name and Location Royal Aircraft Establishment, Farnborough, Hants, UK			
5a. Sponsoring Agency's Code N/A		6a. Sponsoring Agency (Contract Authority) Name and Location N/A			
7. Title Measurements in the near-wake of a transport model, to determine the lift, drag and drag components using Maskell's analysis					
7a. (For Translations) Title in Foreign Language					
7b. (For Conference Papers) Title, Place and Date of Conference					
8. Author 1. Surname, Initials Priest, A.J.	9a. Author 2 Dobney, D.G.	9b. Authors 3, 4 Hill, R.P.	10. Date February 1981	Pages 89	Refs. 15
11. Contract Number N/A	12. Period N/A	13. Project	14. Other Reference Nos. Aero 3497		
15. Distribution statement (a) Controlled by – (b) Special limitations (if any) –					
16. Descriptors (Keywords) (Descriptors marked * are selected from TEST) Wake traverse. Profile drag. Vortex drag. Support rig effects.					
17. Abstract Extensive measurements have been made on a plane normal to the wake of a swept-wing/fuselage model of airbus type, at $C_L = 0.49$ in incompressible flow, using a computer-controlled wake-traverse system incorporating a null-reading five-hole yaw-meter probe. The results define the detailed distributions of total pressure defect, flow velocity, flow angles and streamwise vorticity in the viscous wake at that plane. The results have been analysed within the basic theoretical framework set out by Maskell (1973), allowing the calculation of lift and drag from traverse data, and the resolution of the drag into provisionally-defined components C_{D_I} and $C_{D_{II}}$, respectively relating to the profile drag and vortex drag.					

